UNIVERSITÀ DEGLI STUDI DI MILANO
FACOLTÀ DI SCIENZE E TECNOLOGIE

Ph.D. course in Chemistry, XXXV cycle

Department of Chemistry

Disordering in pyrochlore phases for radionuclides disposal: a multiscale structure study

CHIM/02, CHIM/03

Armando di Biase

Supervisor: Prof. Carlo Castellano

Co-supervisor: Prof. Marco Scavini

Coordinator: Prof. Daniele Passarella

A.A.

2021/2022

Table of Contents

Abstract 3

Part 1 5

Introduction 5

Structure and superstructure 5

Fluorite 6

Pyrochlore 9

Weberite-type 17

Bixbyte 20

Structural disorder in pyrochlore oxides 22

Compositionally induced disorder 27

Thesis objective and outline 30

Part 2 33

Experimental section 33

Synthesis 33

Characterization techniques 35

High-resolution X-ray diffraction and total scattering experiments 35

Raman measurements 47

Part 3 55

$Gd_2(Ti_{1-x}Zr_x)_2O_7$ solid solution 55

Part 4 101

$(Nd_{1-x}Gd_x)_2Zr_2O_7$ solid solution 101

Part 5 123

$Gd_2(Zr_{1-x}Ce_x)_2O_7$ solid solution 123

Conclusions and future prospects 151

Appendix A 155

Disposal of radioactive waste 155

Pyrochlores for actinides immobilization 159

Appendix B.....165
Stability field of the pyrochlore structure.....165
References.....169

Abstract

Oxides with the general formula $A_2B_2O_7$ and the pyrochlore structure have drawn much attention in the field of radionuclides immobilization. The $Gd_2Zr_2O_7$ composition, in particular, has demonstrated high radiation resistance, making it an ideal host-matrix for encapsulating radioactive elements within the crystal structure. Despite the average structure, chemical composition can induce intrinsic structural distortions and control the degree of ordering of cations and anions in pyrochlore oxides, defining their response towards irradiation. To understand the origin of such distortions, an in-depth study of the structure at both the average and local scales is required. In the present thesis, a systematic investigation of three solid solutions related to the $Gd_2Zr_2O_7$ composition is performed. Namely, the following solid solutions are examined: $Gd_2(Ti_{1-x}Zr_x)_2O_7$, $(Nd_{1-x}Gd_x)_2Zr_2O_7$ and $Gd_2(Zr_{1-x}Ce_x)_2O_7$. All the samples are produced by solid-state synthesis and structural changes as a function of chemical composition are studied through High-resolution X-ray Diffraction (HR-XRD), laboratory Raman spectroscopy and the analysis of Pair Distribution Function (PDF). Cation antisite and anion Anti-Frenkel defects accumulate at the average scale as cations become similar in size. These defects are symptoms of structural distortions at the local scale and a weberite-type model is invoked for the description of the short-range order in the $Gd_2(Ti_{1-x}Zr_x)_2O_7$ system. Nevertheless, the deviation from the average structure at the local scale in disordered compositions appear to be more complex than a single structural model can describe.

Part 1

Introduction

Structure and superstructure

The structure of pyrochlore compounds can be easily captured if considered in relation with the structure of fluorite (CaF_2). In particular, a pyrochlore can be regarded as a 'subtraction derivative' of a fluorite. This concept has been clearly outlined by Yakubovich and co-workers in their work on $Na_2Fe_2F_7$ in the context of $Na_2M^{II}M^{III}F_7$ compounds with a weberite structure[1]. The two essential features of a fluorite-like structure are the cubic close packing of cations and the coordination of anions, which remain invariable in all structure types related to the fluorite. The cations are arranged according to a face centered cubic lattice (fcc) and the anions are always four-fold coordinated in tetrahedral sites. Removing one or more anions, leads to the formation of 'subtraction structures' or 'anion-deficient fluorite superstructures', in which the change of the total charge and cations coordination allows to accommodate a wide range of metal ions with different sizes and valences. One can express the general formula of these fluorite-related structures by referring to the cell content of a fluorite, A_4X_8, where A is the sum of all cations and X that of all anions. The number of anion vacancies can be denoted with the subscript 'y' so that the general formula becomes A_4X_{8-y}; if y = 1 one can obtain the formula of a compound with the pyrochlore (e.g. $Gd_2Ti_2O_7$), weberite (Na_2MgAlF_7) or zirconolite

($CaZrTi_2O_7$) structure, if y = 2, a compound with a bixbyite (or C-type) structure (α-Mn_2O_3) can be identified. The subscript can be even non integer and more complex compositions can be achieved with different cations/anions ratios, such as the δ-phase ($Sc_4Zr_3O_{12}$)[2,3] or the murataite structure ($(Y,Na)_6(Zn,Fe)_5Ti_{12}O_{29}(O,F)_{10}F_4$)[4,5].

Fluorite

As for the majority of structure types, the term fluorite primarily indicates the homonymous mineral. In this case, fluorite, with composition CaF_2, owes its name to its use as flux agent in ores melting (from Latin *fleure*, 'to flow')[6,7]. The mineral crystallizes in the cubic crystal system, s.g. $Fm\bar{3}m$ (Z=4) with a cell constant a_f of approximately 5.45 Å. The fluorite structure is also typical of several binary oxides such as CeO_2, ThO_2, UO_2 etc. The asymmetric unit consists of a cation and an anion, which occupy the special positions labeled *4a* and *8c* respectively (see Table 1.1).

Table 1.1 Atoms and their corresponding crystallographic sites in the asymmetric unit of the fluorite structure. A and X represents generic cations and anions respectively

Atom	Wyckoff letter	Site symmetry	x	y	z	Occ.
A	*4a*	$m\bar{3}m$	0	0	0	1
X	*8c*	$\bar{4}3m$	1/4	1/4	1/4	1

As already stated, the cations define a fcc lattice, while the anions, which are placed in tetrahedral interstices, follow a simple cubic array[8,9]. Cations are 8-fold

coordinated in perfect cubes, which share edges with one another (Figure 1.1). The general crystallographic formula for a fluorite-like compound can be written as $^{VIII}AX_2$, where the Roman number indicates the anions coordination around the cation.

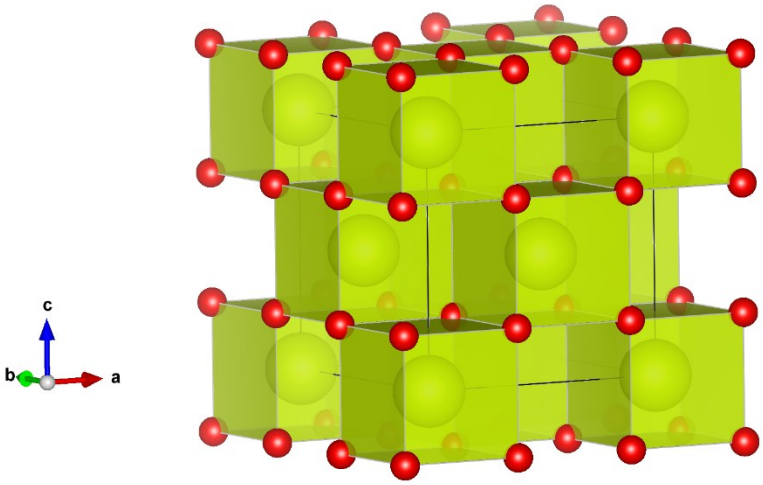

Figure 1.1 Fluorite structure with coordination polyhedra of cations highlighted in yellow. Anions are in red.

In the context of this thesis, it is worth noticing that, beside the anions coordination, each cation in the fluorite structure has 12 nearest neighboring cations, forming a cubo-octahedral cage[9] (see Figure 1.2). Since the atoms are in special positions with all fixed coordinates, the first metal-to-metal interatomic distance can be calculated from the cell constant as $a_f \frac{\sqrt{2}}{2}$.

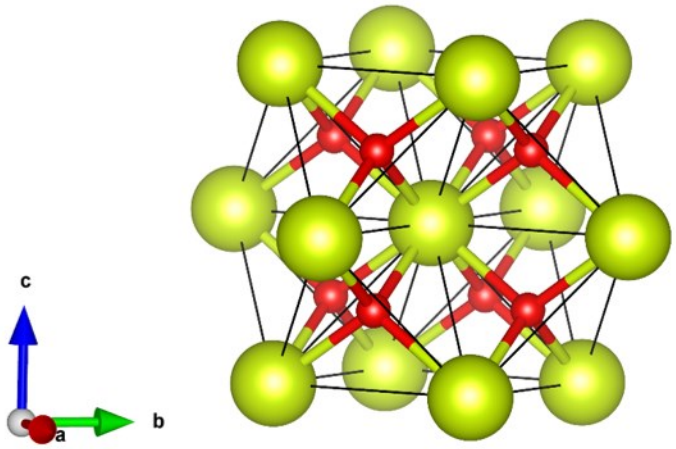

Figure 1.2 Cubo-octahedredron of cations (yellow) surrounding each cation in the fuorite structure. The anions in red are visible within the tetrahedral interstices.

Pyrochlore

The name pyrochlore, from the Greek πῦρ, fire, and χλωρός, green, was given by J.J. Berzelius to a cubic mineral found in Norway that gave a green flame when ignited[10,11] with general composition (Na, Ca)(Nb, Ta)O_6(F,OH). Currently, the term pyrochlore refers to a supergroup of minerals with general formula $^{VIII}A_{2-m}{}^{VI}B_2{}^{IV}X_{6-w}{}^{IV}Y_{1-n}$, where the Roman numbers indicates the coordination of the corresponding crystallographic site and the subscripts *m*, *w* and *n* are used for possible incomplete occupancy of A, X and Y sites[12]. A and B are usually reserved to cations, whereas X and Y are occupied by anions. Pyrochlore oxides have general formula $A_2B_2O_7$ and crystallize in the cubic crystal system, s.g. $Fd\bar{3}m$ (Z=8) with a cell constant a_p of approximately 10.4 Å. The cation A is usually large (radius ≈ 1.0 Å) with 2+ or 3+ valence, while the cation B is typically smaller with 5+ or 4+ valence[11–14]. The present thesis will focus on 3+/4+ compositions and a general scheme of possible of A- and B-site cations is provided in Figure 1.3. It should be noted that not all combinations of elements produce a stable pyrochlore phase, and this largely depends on the ionic radii ratio r_A/r_B. Considering ambient conditions, a pyrochlore phase is formed when r_A/r_B is in the range 1.46 ($Gd_2Zr_2O_7$)-1.78 ($Sm_2Ti_2O_7$)[5,11]. For r_A/r_B values lower than 1.46, cations become more similar in size and a defect fluorite structure is formed. On the other hand, when r_A/r_B exceeds 1.78, a monoclinic perovskite layered structure is favored (e.g. $La_2Ti_2O_7$)[15,16]. In the

presence of Ce^{4+}, formally at the B-site of the structure in $A_2Ce_2O_7$ compositions, the bixbyte structure may form[17–20].

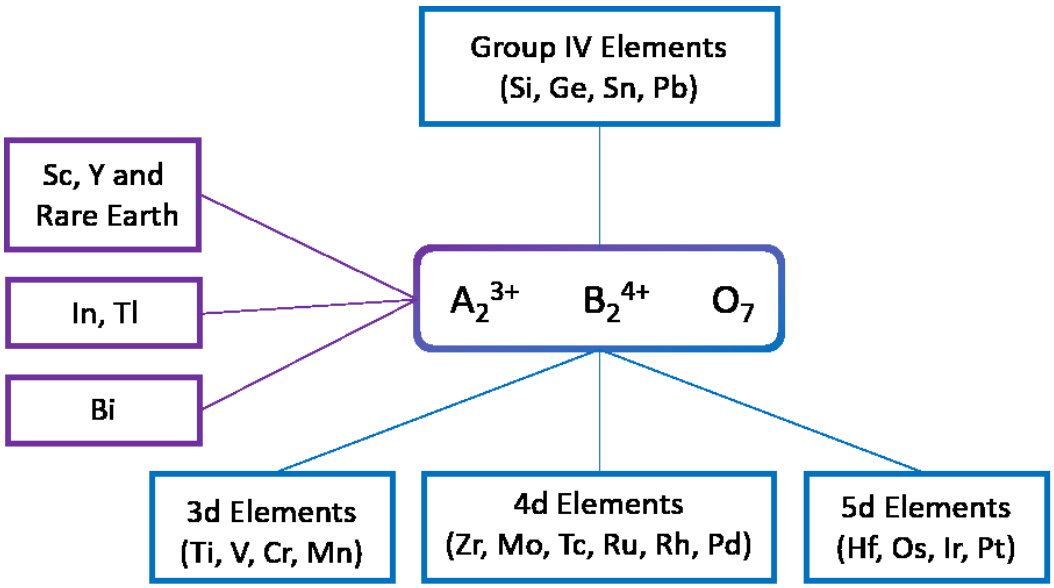

Figure 1.3. Possible combinations of cations in a $A_2^{3+}B_2^{4+}O_7$ pyrochlore oxide [adapted from Ref. 11].

The pyrochlore structure can be regarded as an anion-deficient superstructure (A_4X_{8-y}, y=1) of the fluorite structure with $a_p = 2a_f$, where a_p and a_f are the lattice constants of pyrochlore and fluorite respectively. The doubling of the cell parameter with respect to the fluorite hints an additional atomic ordering within the pyrochlore structure. In fact, cations are distributed over two different crystallographic sites, while anions and anion vacancies are placed in three distinct interstices. The coordinates of the atoms in the asymmetric unit of the pyrochlore structure are listed in Table 1.2. Within the origin choice 2 of space group $Fd\bar{3}m$, two different settings are possible, depending on which cation is placed at the origin[11,21,22]. In the following discussion the setting 2 will be adopted.

Table 1.2 Atoms and their corresponding sites in the asymmetric unit of the pyrochlore structure. A and B are generic cations, while the sites for anions and anion vacancies are indicated by numbered oxygen symbols.

	Atom	Wyckoff letter	Site symmetry	x	y	z	Occ.
	A	*16c*	$.\bar{3}m$	0	0	0	1
	B	*16d*	$.\bar{3}m$	1/2	1/2	1/2	1
setting 1	O1	*48f*	*2.mm*	*x*[a]	1/8	1/8	1
	O2	*8b*	$\bar{4}3m$	3/8	3/8	3/8	0
	O3	*8a*	$\bar{4}3m$	1/8	1/8	1/8	1
	A	*16d*	$.\bar{3}m$	1/2	1/2	1/2	1
	B	*16c*	$.\bar{3}m$	0	0	0	1
setting 2	O1	*48f*	*2.mm*	*x*[a]	1/8	1/8	1
	O2	*8b*	$\bar{4}3m$	3/8	3/8	3/8	1
	O3	*8a*	$\bar{4}3m$	1/8	1/8	1/8	0

[a] *x* value is in the range 0.4375-0.375 for setting 1 (see Ref. 21) or in the range 0.3125 -0.375 for setting 2 (see main text).

The pyrochlore structure has been extensively described in the work of Subramanian and co-workers[11] and hereafter the most significant features will be presented.

As starting point, one can imagine having a fluorite oxide with two different cationic species. In that case, the general formula of the unit cell content would be $^{VIII}(A,B)_4O_8$. The introduction of an oxygen vacancy, randomly distributed over the tetrahedral interstices, reduces the average coordination number of cations to seven and the general formula becomes $^{VII}(A,B)_4O_7$. One can refer to this composition as anion-deficient fluorite or defect-fluorite. To produce a pyrochlore ordering, two alternate [110] rows of cations A and B are then arranged in every other (001) plane (and in [-110] in the other (001) planes) (see Figure 1.4). The ordering of cations leads to a doubling of the unit cell and the overall symmetry is reduced in such a way that the new space group is $Fd\bar{3}m$. Considering one eighth of the unit cell, the general formula of the pyrochlore compound is now $^{VIII}A_2{}^{VI}B_2O_7$.

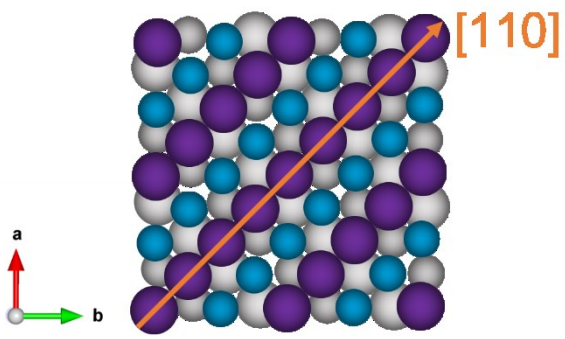

Figure 1.4 Ordered rows of A (violet) and B (blue) cations parallel to the [110] direction in the (001) plane. Oxygen atoms are omitted for clarity.

Looking at the cubic close packing. of cations, the pyrochlore structure is built by alternating layers of A_3B and AB_3 cations stacking along the [111] direction[23,24] (Figure 1.5).

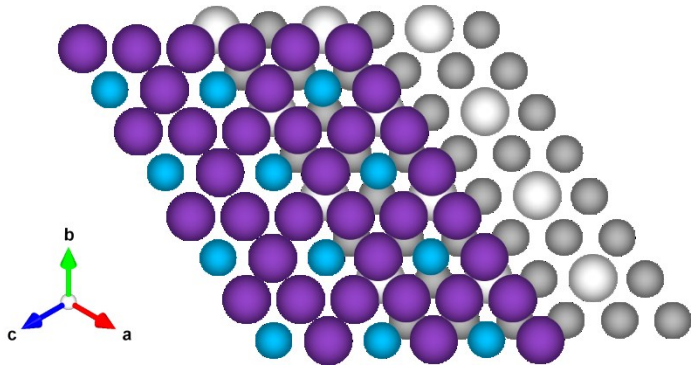

Figure 1.5 A_3B (colored, top) and AB_3 (grey, bottom) layers of cations stacking along the [111] direction. A-cations are in violet, B-cations are in blue.

This kind of cations stacking generates three types of tetrahedral interstices where oxygen atoms and vacancies are ordered. The oxygen placed at the *8b* site (O2, see Table 1.2) are at the center of A_4 tetrahedra, those at the *48f* site (O1) are coordinated by two A- and two B-cations in A_2B_2 tetrahedra, while nominally vacant *8a* sites (O3) are at the center of B_4 tetrahedra (see for example Figure 1.6a). In a description of the pyrochlore structure equivalent to the fluorite, the O1 oxygen atom occupies the *48f* site at coordinates (3/8, 1/8, 1/8). In reality, O1 provides electrostatic shielding to the four B-cations exposed across the O3 vacancy by shifting from this ideal position towards the vacancy along <100> directions. The larger A-O1 distance

compared to the B-O1 distance also contributes to the shift[25]. The displacement of O1 is expressed by the 'x_{48f}' coordinate (see Table 1.2), which will be designated as *x*O1 hereafter. The presence of an ordered anion vacancy (O3) implies that the coordination number of the A-cation is 8 (like in the fluorite structure), while that of the B-cation is 6 (Figure 1.6b). Furthermore, the shift *x*O1 causes a distortion of the cations coordination environment. In particular, two limiting values of *x*O1 define the shape of cations coordination polyhedra as follows: when *x*O1 = 0.375, the A-coordination polyhedron is a perfect cube, while that of B-cations is a trigonally flattened octahedron; the other limiting value for *x*O1 is 0.3125 and, in that case, A is in a distorted cube and B is in a regular octahedron. Experimentally, *x*O1 is in between those values, so that A is in a scalenohedron surrounded by six O1 and two O2 oxygen atoms with two set of distances (6 A-O1 + 2 A-O2), while B is in a trigonal antiprism coordinated by six O1 oxygen atoms at equal distance (Figure 1.6b). The coordination environment around A-cations can be better visualized looking at the AB_3 plane of the pyrochlore structure projected along the [111] direction (Figure 1.7). In this view, the pyrochlore structure appears to be composed of corner-shared BO_6 octahedra, which form hexagonal tungsten bronze-like layers parallel to (111) planes[11,23]. A-cations are placed in the hexagonal cavities of this 3D framework and are coordinated by six O1 oxygen atoms forming a chair-like ring and two anions O2 in a linear arrangement, with A-O2 shorter than A-O1 distances.

Regarding the cations coordination, it should be mentioned that, in analogy with the fluorite structure, the first metal coordination shell around any metal in the pyrochlore structure consists of 12 cations (six A and six B) placed at the corners of a cubo-octahedron, at a distance from the central cation of $a_p \frac{\sqrt{2}}{4}$.

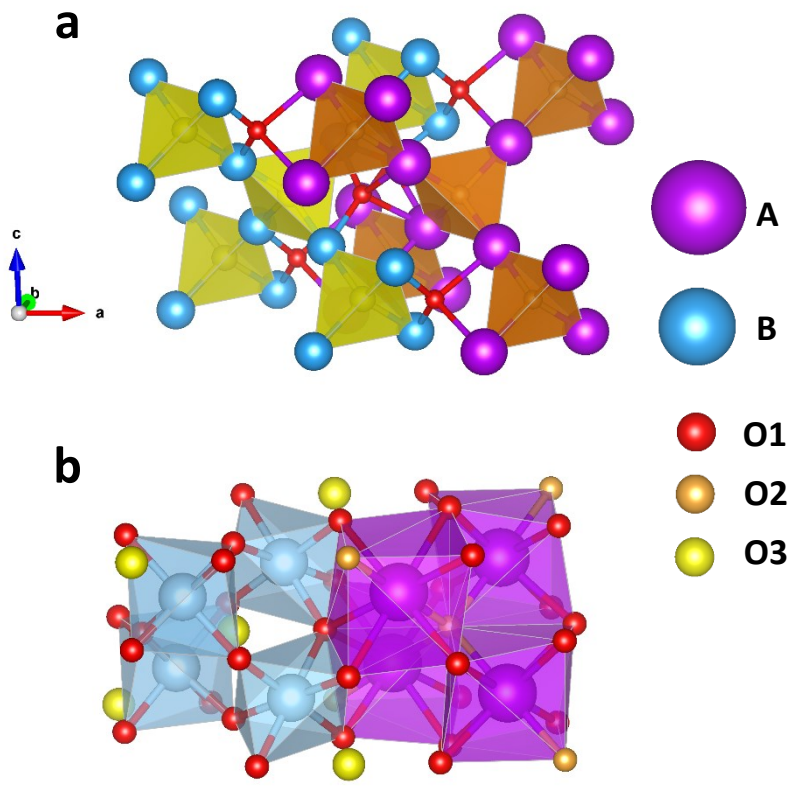

Figure 1.6 Detail of the pyrochlore structure represented by the coordination polyhedra of (**a**) anions and (**b**) cations. (O1)A_2B_2 tetrahedra are not shown for clarity. While A-cations are 8-fold coordinated by six O1 and two O2 oxygen atoms, O3 vacancies reduce the coordination number of B-cations to 6.

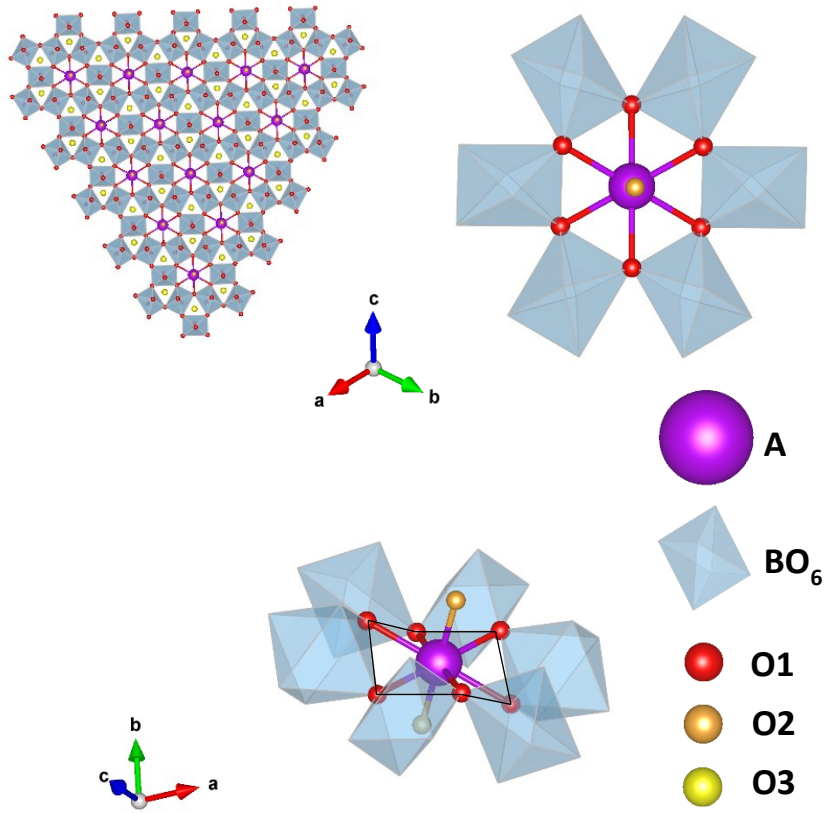

Figure 1.7 At the top, the pyrochlore structure projected along the [111] direction and a detail of the hexagonal cavity formed by BO_6 octahedra. At the bottom, other view of the hexagonal cavity with the O2-A-O2 fragment and the chair-like ring of O1 oxygen atoms.

Weberite-type

The archetype structure of weberite materials is that of the reference mineral Na_2MgAlF_7, which was found in Greenland and named after the Danish industrialist Theobald Weber[23,26]. It crystallizes in the orthorhombic crystal system, s.g. *Imma* (Z=4) with cell constants of approximately 7.5, 10 and 7.3 Å (see [1,23] and references therein). The cell metrics can be easily obtained from that of a pyrochlore structure by a 45° rotation around one of the cubic axes. Given $2a_f$ as the cell parameter of a pyrochlore structure (where a_f represents the lattice constant of a fluorite), a weberite structure has cell edges approximately $a_f\sqrt{2}$, $2a_f$ and $a_f\sqrt{2}$ [23,27]. As for the pyrochlore, the weberite can be regarded as a subtractive derivative of the fluorite structure (A_4X_{8-y}; y = 1), but with superior cationic ordering with respect to the pyrochlore[1]. A general formula for materials adopting the weberite structure may be written in the form $^{VIII}A1^{VIII}A2^{VI}B1^{VI}B2X_7$, where A and B are generic cations and X represents a generic anion (usually F^- or O^{2-}). This formula highlights the presence of four distinct crystallographic sites for cations, two in 8-fold and two in 6-fold coordination, allowing for a great chemical variability within the structure. Being a superstructure of the fluorite, the weberite retains the fcc arrangement of cations, with A_3B and AB_3 layers stacking along the [011] direction. Pyrochlore and weberite differ precisely in the stacking of two adjacent A_3B and AB_3 layers[23].

Several modifications of the archetype weberite structure exist, which not only crystallize in the orthorhombic (O), but also in the monoclinic (M) and trigonal (T)

crystal systems. These variants are classified according to the IMA (International Mineralogical Association) nomenclature as follows: a capital letter indicating the crystal system is preceded by the number of slabs of cations in the unit cell ($2O$, $2M$, $3T$ etc.). Each slab consists of one A_3B and one AB_3 layer[1,23]. A variant of the weberite structure relevant to this work is the so called 'weberite-type' structure. It is related to the canonical $2O$ weberites, but the typical layers with BO_6 and AO_8 polyhedra alternate with layers where A-cations are 7-fold coordinated (see for example Figure 1.8). Unlike weberites (or pyrochlores), the three-dimensional BO_6 network is not preserved in weberite-type materials[23].

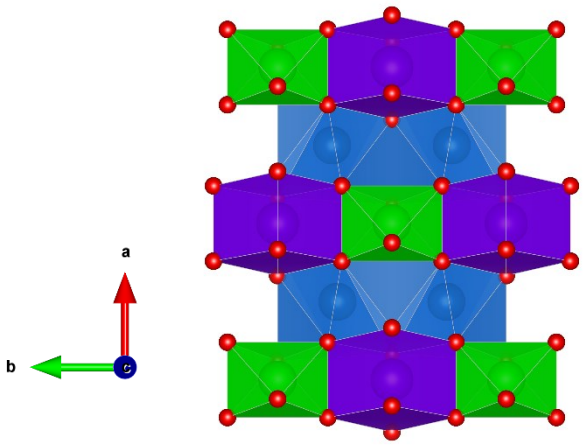

Figure 1.8 Unit cell of weberite-type structure A_3BO_7 in $Ccmm$ space group along [001]. A-site cations 8-fold coordinated are in purple polyhedra and B-site cations 6-fold coordinated are in green polyhedra; the 7-fold coordinated sites occupied by A-site cations are in blue. Oxygen atoms are represented by red spheres.

The weberite-type structure is found in Ln_3BO_7 compounds where Ln is a lanthanide element (La → Gd) and B is Nb or Ta[23,27–29]. In recent years, the weberite-type structure has been employed to describe the local order in disordered $A_2B_2O_7$ materials adopting a long-range defect fluorite structure[30,31]. The atomic positions for a weberite-type $A_2B_2O_7$ compound in space group *Ccmm* (alternative setting of space group *Cmcm*, n°63) are listed in Table 1.3. In analogy with the pyrochlore structure, A-cations are placed in 8-fold coordinated sites, indicated by the Wyckoff letter *4b*, while B-cations occupy 6-fold coordinated sites, labelled *4a* in Table 1.3. The oxygen anions are ordered in four crystallographic sites, three with multiplicity four (*4c*) and one with multiplicity 16 (*16h*). The anion vacancy is located at a *4c* site as well (not shown in table 1.3). In contrast with the pyrochlore structure, an additional 7-fold coordinated site is present (*8g*) and it is shared by both cations[30,32]. Further details on the weberite-type structural model will be given in the section dedicated to the $Gd_2(Ti_{1-x}Zr_x)_2O_7$ solid solution (Part 3).

Table 1.3 Atoms and their corresponding sites in the asymmetric unit of the weberite-type structure in *Ccmm* space group. Coordinates are taken from Ref. 30. Fixed coordinates are shown as fractions or zeros.

Atom	Wyckoff letter	Site symmetry	x	y	z	Occ.
A	*4b*	*2/m..*	0	1/2	0	1
B	*4a*	*2/m..*	0	0	0	1
A/B	*8g*	*..m*	0.230	0.244	0.25	1
O1	*16h*	1	0.125	0.227	0.970	1
O2	*4c*	*m2m*	0.084	0	1/4	1
O3	*4c*	*m2m*	0.125	1/2	1/4	1
O4	*4c*	*m2m*	0.844	1/2	1/4	1

Bixbyte

Another fluorite-related superstructure is the bixbyte, also known as C-type, which was originally identified in the mineral $(Fe,Mn)_2O_3$ and named after the mineral dealer Maynard Bixby[33,34]. In the case of the C-type structure, the general formula A_4X_{8-y}; has y = 2. With respect to the fluorite structure, one fourth of the oxygen ions is removed along <111> directions and the structure relaxes in such a way that the regular cubes, which are the cations coordination polyhedra in the fluorite, becomes distorted octahedra[34,35]. The ordering of the anions and vacancies results in a doubling of the unit cell parameter (a_c) with respect to the fluorite (e.g. Gd_2O_3, with $a_c \approx 10.81$ Å[36]) and a reduction of the overall symmetry to space group $Ia\bar{3}$[35,37].

The C-type structure is typically adopted by sesquioxides of rare earth elements with 3+ valence from Sm to Lu[34,38]. The metal atoms are distributed over two independent crystallographic sites; M1 and M2, with multiplicity 8 and 24 respectively, while anions occupy one site with multiplicity 48 (see Table 1.4). When tetravalent cations (typically Ce^{4+}, but also Zr^{4+}) are introduced and a solid solution is formed, excess anions balancing the positive charge may be incorporated at the *16c* site (*x, x, x*), ideally increasing the cations coordination from 6 to 8 (Figure 1.9)[35,39,40].

Table 1.4 Atoms and their corresponding sites in the asymmetric unit of the C-type structure. Coordinates are taken from Ref. 35. M1 and M2 represent the cation sites, while O1 and O2 are the anion sites. Fixed coordinates are shown as fractions or zeros.

Atom	Wyckoff letter	Site symmetry	x	y	z	Occ.
M1	*8b*	.$\bar{3}$.	1/4	1/4	1/4	1
M2	*24d*	2..	-0.0188	0	1/4	1
O1	*48e*	1	0.388	0.139	0.376	1
O2	*16c*	.3.	0.401	0.401	0.401	[a]

[a] Occupation of O2 site follows that of an additional tetravalent cation introduced at the M1 and M2 sites.

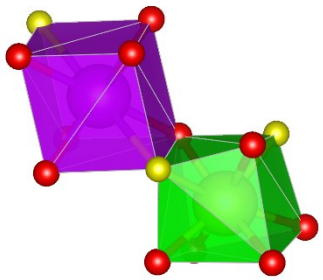

Figure 1.9 Coordination polyhedra of M1 (violet) and M2 (green) cations. O1 sites are shown as red spheres, while O2 sites are represented by yellow spheres.

Structural disorder in pyrochlore oxides

The pyrochlore structure can easily accommodate disorder. For example, the presence of atoms with an active lone pair such as Bi^{3+} might induce distortions and introduce disorder within the pyrochlore structure. In systems like $Bi_2(Hf_{1-x}Ti_x)_2O_7$, static disorder was modelled by displacement of Bi and O atoms towards interstitial sites *96g* (*x, x, z*), *96h* (*0, y, -y*) and *32e* (*x, x, x*)[41]. However, the most common defects that can affect a pyrochlore structure are cation antisite and anion Anti-Frenkel defects. These can be expressed in Kröger-Vink notation as follows[2,42]:

- cation antisite defects $A_{16d}^{\times} + B_{16c}^{\times} \rightarrow A_{16c}' + B_{16d}^{\bullet}$
- anion Anti-Frenkel defects $O_{48f}^{\times} + V_{8a}^{\times} \rightarrow V_{48f}^{\bullet\bullet} + O_{8a}''$

$$O_{8b}^{\times} + V_{8a}^{\times} \rightarrow V_{8b}^{\bullet\bullet} + O_{8a}''$$

Cations at the *16c* (B) and *16d* (A) sites exchange places, while anions at the *48f* (O1) or *8b* (O2) sites move to the interstitial *8a* (O3) site leaving a vacancy behind. Studies on ionic transport in pyrochlore oxides have identified the movement of oxygen ions to the interstitial site with vacancy at the *48f* site as the most probable intrinsic defect in the anionic substructure[43–45]. The *x*O1 parameter acts as a marker for the presence of defects in pyrochlore oxides[46]. Specifically, as anion Anti-Frenkel defects form at the *48f* and *8a* sites, a repulsive interaction arises between the freshly occupied O3 position and the remaining O1 oxygen ions. At the same time, the formation of cation antisite defects, with smaller B- substituting larger A-cations,

leads to a reduction of the average A-O1 distance[25]. These phenomena result in a diminishing of the shift of oxygen O1 from its ideal position (3/8, 1/8, 1/8) and an increase of *x*O1 towards the ideal coordinate 0.375. The coupling of cation antisite and anion Anti-Frenkel defects is associated with a disordering mechanism that takes the structure from a perfectly ordered state (defects-free pyrochlore, where *x*O1 = 0.3125) to an intermediate disordered state (defect or disordered pyrochlore) and, eventually, to a fully disordered state (defect fluorite, where *x*O1 = 0.375)[11,25,47–49].

In the context of radionuclides immobilization, the waste form is subjected to radiation damage, which, in turn, is related to the accumulation of disorder within the structure. It has been established that, when exposed to irradiation, pyrochlores are prone to form both cation antisite and anion Anti-Frenkel defects. Ultimately, defects accumulation can trigger an order-disorder phase transition at the long-range scale, resulting in either a transformation from the pyrochlore to the defect fluorite structure or even amorphization[50]. The tendency of a pyrochlore compound to undergo a phase transition to the defect fluorite or amorphous state (i.e. its radiation tolerance) can be related to structural considerations and defects formation energies[42,51]. It was already mentioned that not all possible combinations of A^{3+}/B^{4+} cations can generate a stable pyrochlore phase. In this regard, the radii ratio r_A/r_B was the first parameter used to define the stability field of pyrochlore oxides[52]. Besides the radii ratio r_A/r_B, Minervini and co-workers proposed another method to delineate the pyrochlore stability field. They used atomistic simulations based on energy

minimization of the pyrochlore structure described with a Born-like model to derive contour maps of cation antisite and anion Anti-Frenkel defects formation energies as a function of r_A and r_B[42]. They first highlighted that $A_2B_2O_7$ compounds with positive reaction enthalpy with respect to the binary A_2O_3 and BO_2 oxides would never form stable pyrochlore phases. Then, they calculated the formation energy of a cation antisite defect coupled with an anion Anti-Frenkel defect (disorder energy) for several combinations of A- and B-cations. $A_2B_2O_7$ compositions with a disorder energy per defect above 0.7 eV have the tendency to form stable pyrochlore phases. Those that lie below this threshold are prone to disorder and form defect-fluorite structures. The authors noticed that this criterion based on defects formation energies performed slightly better than the one based on the radii ratio in defining the stability of pyrochlore phases. Nevertheless, low defect formation energies were associated with high radiation resistance in pyrochlore or fluorite oxides. These materials can easily accommodate disorder in the crystal structure when subjected to irradiation. On the other hand, compositions with high defects formation energies, or large size mismatch between cations, are destabilized by the introduction of defects and therefore tend to amorphize under irradiation[51]. Remarkably, this behavior is exemplified in pyrochlore oxides with composition $Gd_2(Ti_{1-x}Zr_x)_2O_7$. Ti-rich samples are subjected to amorphization when exposed to high radiation doses. In contrast, Zr-rich samples are less susceptible to radiation-induced amorphization. Notably, the $Gd_2Zr_2O_7$ endmember does not undergo an amorphization process, but instead, a phase transition to the defect fluorite structure occurs[53]. Considering the

ionic radii of Gd^{3+} in 8- fold coordination (r_{Gd3+} = 1.053 Å) and $Zr^{4+}$and Ti^{4+} in 6-fold coordination (r_{Zr4+} = 0.72 Å, r_{Ti4+} = 0.605 Å)[54], the introduction of Zr in place of Ti in the structure of $Gd_2(Ti_{1-x}Zr_x)_2O_7$ compositions, leads to a decrease in the value of r_A/r_B. This implies that the cations become more similar in size and the energy for the formation of defects is reduced, allowing for the transformation into a defect fluorite composition $(A,B)_4O_7$. Conversely , the formation of a defect fluorite structure in samples with a large mismatch between cations radii (e.g. $Gd_2Ti_2O_7$) is not favorable and, therefore, the irradiation process and, the consequent defects formation, leads directly to an amorphous state[51]. It should be emphasized here that in general $Gd_2Ti_2O_7$ adopts an ordered and nearly defect-free pyrochlore structure, whereas $Gd_2Zr_2O_7$ already contains a certain amount of defects, which are the key features for its radiation resistance. In fact, as previously highlighted by Sickafus et al. in 2000, materials that already possess a certain degree of disorder exhibit high radiation tolerance and can readily accommodate additional disorder within their crystal structure when exposed to high radiation doses[51]. For this reason, $Gd_2Zr_2O_7$ is regarded as an ideal waste form for the immobilization of radionuclides.

Not only does the ordering of cations and anions influence the response towards irradiation of pyrochlore oxides, but it has also a profound impact on other physical properties. In their foundational work on structural disorder and ionic conductors, Moon and Tuller observed a sharp increase in oxygen ion conductivity in the solid solution $Gd_2(Ti_{1-x}Zr_x)_2O_7$ passing from the Ti- to the Zr-endmember. This increase

was related to the growing presence of anion Anti-Frenkel defects resulting from Zr-doping[55–59]. In fact, the anion Anti-Frenkel defects provide the necessary oxygen vacancies that are the charge carries in these pyrochlore systems, ultimately enhancing the ionic conduction[43,44,55]. The increase in oxygen ion conductivity follows the reduction of r_A/r_B in the $Gd_2(Ti_{1-x}Zr_x)_2O_7$ system, although a saturation is reached at about 0.60 of Zr fraction[55,60]. Excessive structural disorder can diminish or even have a detrimental effect on ionic conductivity. Indeed, depending on the annealing temperature, $Gd_2Zr_2O_7$ can be prepared as either pyrochlore or defect fluorite phase[11]. Notably, higher conductivity is achieved in the former case[61]. This result may be explained by considering that preferential pathways for oxygen jumps exist in an ordered pyrochlore structure compared to a disordered defect fluorite structure[43]. The degree of ordering clearly influences the oxygen ion conductivity in a pyrochlore or defect fluorite material and, in particular, clusters of defects determines to which extent ions interact and diffuse through the structure[60,62].

Structural distortions and reorganization induced by defects have also other implications. For example, distortions induced by chemical substitution in medium- and high-entropy pyrochlore oxides appear to play a major role in the reduction of thermal conductivity[63,64]. Considering the case of $Gd_2Zr_2O_7$, the presence of cation antisite and anion Anti-Frenkel defects alone does not affect much its thermal conductivity. As already mentioned, $Gd_2Zr_2O_7$ can be synthesized as either pyrochlore or defect fluorite phase[11,65] and it shows the same thermal conductivity in both cases[65]. However, it has been reported that the thermal conductivity in the

series $Gd_{1.6}Ln_{0.4}Zr_2O_7$ (with Ln = La^{3+}, Nd^{3+}, Sm^{3+}, Dy^{3+} and Er^{3+}) changes with lanthanide substitution[66]. The La-doped sample has a lower thermal conductivity than $Gd_2Zr_2O_7$, although the value is not as low as one would expect merely on the basis of mass and size difference between La and Gd. The larger and lighter La^{3+} ions act as point defects in $Gd_2Zr_2O_7$, locally distorting the structure. These defects easily scatter phonons, reducing their mean free path. As a consequence, the thermal conductivity by lattice vibrations decreases[67,68]. At the same time, the La-substitution produces a pyrochlore structure with anion vacancies more ordered (i.e. with less anion Anti-Frenkel defects) than in pristine $Gd_2Zr_2O_7$. The ordering process mitigates the phonons scattering by substitutional defects, limiting the reduction of thermal conductivity[66].

Compositionally induced disorder

The focus of this work is the observation that structural disorder is present in pyrochlore oxides and can be enhanced solely through chemical substitution. This phenomenon has been reported in early investigations on the $Gd_2(Ti_{1-x}Zr_x)_2O_7$ system[69–71]. Hess and co-workers studied the compositionally driven pyrochlore to defect fluorite phase transition in $Gd_2(Ti_{1-x}Zr_x)_2O_7$ pyrochlores prepared at 1600°C[70]. XRD patterns revealed a step-like behavior in the phase transition. In fact, all the samples crystallized in the pyrochlore structure except for the $Gd_2Zr_2O_7$ endmember, which adopted a defect fluorite structure. Furthermore, by means local probes such

as Extended X-ray Absorption Fine Structure (EXAFS) and vibrational spectroscopy, progressive anion disorder was detected with increasing Zr substitution across the entire compositional range. EXAFS data indicated a gradual change in the coordination environment of Gd from a pyrochlore-like configuration (6+2 oxygen nearest-neighbors, two set of distances) in $Gd_2Ti_2O_7$ to a defect fluorite-like environment (7 oxygen nearest-neighbors at a single distance) in $Gd_2Zr_2O_7$. In contrast, the coordination of Ti and Zr showed no significant changes with chemical substitution, suggesting a similarity in the (Ti/Zr) site local environment between pyrochlore compositions and the defect fluorite compound.

Structural disorder was induced also by introducing different elements at the Gd-site in $Gd_2Zr_2O_7$. Blanchard and colleagues completed a systematic study of the lanthanoid $Ln_2Zr_2O_7$ series (Ln = La, Ce, Pr, Nd, Sm, Eu, Gd, Tb, Dy, Ho, Er, Tm)[72]. X-ray and neutron diffraction patterns were used to assess the average structure of the samples. A pyrochlore structure was found for lanthanide elements from La to Gd, whereas a defect fluorite structure was detected in the case of Ln = Tb → Tm. A tetragonal fluorite-like phase with formula $(Ce,Zr)O_2$ was obtained in the case of Ce. Interestingly, $Gd_2Zr_2O_7$ is placed at the boundary between pyrochlore and defect fluorite with a r_A/r_B =1.46. The analysis of crystal field splitting derived by Zr-L_3 edge XANES allowed Blanchard and colleagues to study the coordination number (CN) of Zr as a function of r_A/r_B in this lanthanide series. A progressive increase in CN was observed for pyrochlore compositions, while no significant changes were

detected for defect fluorite samples. This result was interpreted as a continuous transformation of Zr-coordination environment from pyrochlore-like (6-fold coordination) to defect fluorite -like (7-fold coordination) in the series.

In the last decade, the effects of chemical substitution on structural disorder in different pyrochlore oxides related to $Gd_2(Ti_{1-x}Zr_x)_2O_7$ have been documented by several studies. Systems like $Y_2(Ti_{1-x}Zr_x)_2O_7$[73], $Y_2(Sn_{1-x}Zr_x)_2O_7$[74,75], $Y_2(Ti_{1-x}Hf_x)_2O_7$[76] and $(Gd_{1-x}Tb_x)_2Zr_2O_7$[77] have been extensively characterized by diffraction and spectroscopic tools. The reports focused on the emergence of cations and anions disorder with decreasing r_A/r_B, which drives the pyrochlore to defect fluorite phase transition. Diffraction methods were employed to investigate the long-range order, while spectroscopic tools such as vibrational spectroscopy, X-ray absorption spectroscopy (XAS), solid-state nuclear magnetic resonance (NMR), and the analysis of Pair Distribution Function (PDF) from total scattering data were used to explore the atomic arrangement at the local scale. In this scenario, a recent study by Drey et al. focused on the $Ho_2(Ti_{1-x}Zr_x)_2O_7$ solid solution[31]. Analyses with synchrotron X-ray and neutron diffraction confirmed an abrupt phase transition from pyrochlore ($Ho_2Ti_2O_7$) to defect fluorite ($Ho_2Zr_2O_7$) within a narrow compositional range around 0.60 of Zr fraction. Conversely, the PDF analysis based on both X-ray and neutron data revealed a gradual increase of disorder in the short-range structure, which was modeled using the weberite-type. The study suggested that, on Zr-substitution, nanodomains with the weberite-type structure progressively

accumulated within the pyrochlore matrix until a critical density is reached and a phase transition at the average scale is triggered. This work clarifies the relationship between changes in chemical composition and the extent of structural disorder in pyrochlore oxides across various length scales: despite having the same average structure, pyrochlore oxides can exhibit varying degrees of local-scale disorder depending on their composition. Recently, weberite-like domains have been extensively recognized as building blocks of the local structure of several pyrochlore oxides subjected to disordering processes by mechanical milling[122,191], irradiation[123,192–194] and chemical substitution[31,195–197].

To summarize, the ordering of cations and anions in $Gd_2Zr_2O_7$ and related pyrochlore compositions can be modified by chemical substitution resulting in a change of physical properties. The study of these ordering phenomena in pyrochlore materials is fundamental in view of their application as host-matrices for radionuclides disposal.

Thesis objective and outline

The aim of the present thesis is to conduct a systematic investigation of the long-range and short-range structure of $Gd_2Zr_2O_7$ pyrochlore composition, varying both the A- and B-cations. Specifically, building upon previous investigations, the Gd-Ti-

Zr-O system, in the form of $Gd_2(Ti_{1-x}Zr_x)_2O_7$ solid solution, is chosen as the first model system to investigate the disorder induced by chemical substitution. Furthermore, an additional step is taken by introducing Nd^{3+} and Ce^{4+} cations into the structure of $Gd_2Zr_2O_7$, resulting in the formation of a $(Nd_{1-y}Gd_y)_2(Zr_{1-z}Ce_z)_2O_7$ solid solution. Nd^{3+} and Ce^{4+} have been selected for their potential to act as surrogates for Am^{3+} and Pu^{4+} respectively on the basis of isomorphic substitution[78,79]. Specifically, the ionic radius of Nd^{3+}in 8-fold coordination (r_{Nd3+} = 1.109 Å) is comparable to that of Am^{3+} (r_{Am3+} = 1.09 Å), while the ionic radius of of Ce^{4+} in 6-fold coordination (r_{Ce4+} = 0.87 Å) is similar to that of Pu^{4+} (r_{Pu4+} = 0.86 Å)[54]. The use of neodymium and cerium simulates the effect that the size of actinides americium and plutonium would have on the structure of $Gd_2Zr_2O_7$, avoiding at the same time the use of real active elements. All the samples are produced by solid-state synthesis and characterized by means of diffraction and spectroscopic techniques. Synchrotron High-Resolution X-ray diffraction is used to examine the average structure of the materials, while Raman spectroscopy and PDF analysis are employed to probe the short-range structure.

This first introductory part of the thesis has provided an in-depth description of the pyrochlore structure, highlighting its connections with other significant structural types. In addition, the scientific background for the present work has been reviewed. Part 2 outlines the procedure adopted for preparing the materials, along with the characterization techniques employed to analyze their structural properties. These

first two chapters establish the foundation for the subsequent sections, which are dedicated to the presentation of the experimental results and their interpretation in the context of existing scientific literature. Of special importance is the chapter devoted to the investigation of the $Gd_2(Ti_{1-x}Zr_x)_2O_7$ solid solution (Part 3), which serves as the central focus of this thesis. As the analysis of the data regarding double-doped samples in the $(Nd_{1-y}Gd_y)_2(Zr_{1-z}Ce_z)_2O_7$ solid solution is still ongoing, this thesis presents preliminary results that are limited to the $(Nd_{1-x}Gd_x)_2Zr_2O_7$ (Part 4) and $Gd_2(Zr_{1-x}Ce_x)_2O_7$ (Part 5) series. Finally, the concluding chapter offers a comprehensive summary of the findings, ultimately leading to the formulation of concluding remarks and future prospects.

It should be noted for future reference the '*x*' coordinate of the oxygen atom placed at the *48f* site will be indicated *x*O1, while the molar fraction of Zr, Gd and Ce in the corresponding solid solutions will be designated x_{Zr}, x_{Gd} and x_{Ce}

Part 2

Experimental section

Synthesis

All the samples analyzed in the context of this PhD thesis were prepared by solid-state reaction at 1500 °C starting from the commercially available metal oxides as precursors (Gd_2O_3, ZrO_2, TiO_2, Nd_2O_3 and CeO_2). The temperature value (*T*) was selected on the basis of thermodynamic data and previous investigations on these systems[39,78,80–82]. Special care was taken regarding the $Gd_2Zr_2O_7$ composition, , for it was known that it crystallizes as defect fluorite at *T* values higher than 1500 °C[70,83,84]. In particular, the reaction was carried out according to the following procedure:

- reactants were stored at 110°C under vacuum prior to the reaction in order to minimize the presence of moisture traces or other volatile impurities;
- reactants were weighed according to specific stoichiometric ratios for the production of the target compound;
- reactants were intimately mixed in an ethanol/acetone slurry by using an agata mortar and pestle for about 20 minutes;
- the mixture was dried and the pressed into a 13 mm diameter pellet with an 8-ton operating press;

- the pellet was placed onto an alumina crucible and fired in air in a vertical tube furnace with $MoSi_2$ heaters at 1500 °C for 24 hours with a heating/cooling rate of 5 °C/min;
- after sintering, the pellet was ground in a mortar and re-pelletized for the next annealing cycle (this step was repeated until a homogeneous sample was obtained; usually 5/6 annealing cycles were performed).

The homogeneity of the produced sample was monitored by means of laboratory X-Ray Powder Diffraction. Powder patterns were collected at room temperature on a Rigaku MiniFlex600 diffractometer with Cu Kα radiation ($5°<2\theta<90°$, step 0.02°, 5°/min). An XRD pattern was recorded after each annealing step for all the samples of solid solution $Gd_2(Ti_{1-x}Zr_x)_2O_7$. In the case of the $(Nd_{1-y}Gd_y)_2(Zr_{1-z}Ce_z)_2O_7$ series, a diffraction pattern was collected after the first, third and last annealing cycle.

Characterization techniques

High-resolution X-ray diffraction and total scattering experiments

X-ray diffraction patterns were collected at the European Synchrotron Radiation Facility (ESRF), Grenoble (France), during two experiments held at beamline ID22[85,86]. The $Gd_2(Ti_{1-x}Zr_x)_2O_7$ series was investigated in the context of experiment CH-5900[87], along with selected samples doped with Nd and Ce. A more extensive investigation on the $(Nd_{1-x}Gd_x)_2Zr_2O_7$ and $Gd_2(Zr_{1-x}Ce_x)_2O_7$ solid solutions was performed within experiment CH-6218[88].

Samples were loaded into 0.5 mm diameter Kapton® capillaries and mounted parallel to the axis of the diffractometer. The capillaries were spun during the measurements to ensure a good powder average and to reduce preferred-orientation effects. A nitrogen blower was employed to cool the samples down to 90K (Figure 2.4).

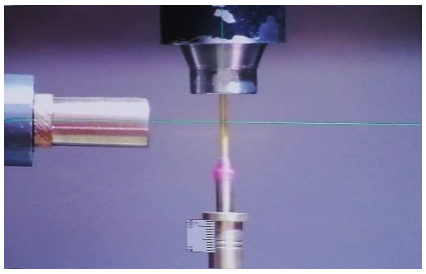

Figure 2.4 Close-up of a loaded capillary mounted on a brass head on the diffractometer with the aid of some red wax. The nitrogen blower is on top, while the collimator, where the incident beam comes from, is visible on the left.

The study of the average structure of the solid solutions was performed through Rietveld refinements of diffraction patterns[89]. The analysis was based on the refinement of lattice constants, positional and thermal displacement parameters and fractional occupancies of shared sites in the structural models. In order to extract these structural parameters, an accurate determination of peaks position and intensity was required. To these purposes, the high-resolution setup of the beamline was exploited and High-resolution X-ray Diffraction (HR-XRD) patterns were collected. Specifically, a nine-element detector was scanned vertically as a function of 2θ in the range $0° \leq 2\theta \leq 48°$ at 35 keV (with λ=0.354176 Å for experiment CH-5900 and λ=0.352780 Å for experiment CH-6218; in both experiments a counting time of 60 min/pattern was used and $Q_{max} \approx$ 14.4 $Å^{-1}$ was reached). The high resolution was granted by the presence of nine Si 1 1 1 analyser crystals, giving instrumental contribution to FWHM of about 0.003° 2θ[86] (Figure 2.5).

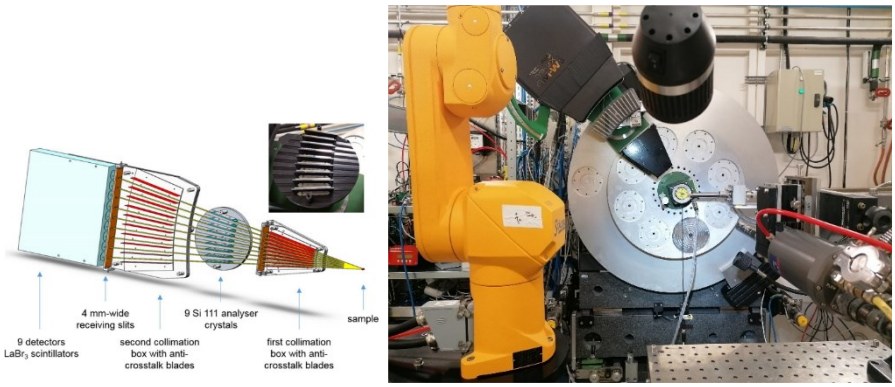

Figure 2.5 On the left a schematic representation of the 9 crystals multi-analyser stage at ID22 is depicted [from Ref. 86]; on the right a picture taken inside the ID22 experimental hutch displaying the diffractometer and the robotic arm (in orange) for automated sample change.

The Rietveld analysis was performed within the GSAS software suite of programs[90] and its graphical interface EXPGUI[91]. The background has been fitted through Chebyshev polynomial. Line profiles have been fitted using a modification of TCH pseudo-Voigt function as implemented in GSAS. In the refinements, scale factor, cell constants, positional and isotropic atomic mean square displacement parameters (U_{iso}), have been varied, as well as background, and peak profile parameters. Details on the structural models will be provided in the next chapters.

Powder patterns suitable for Pair Distribution Function (PDF) analysis were recorded following another strategy. Total scattering experiments were performed and to maximize the value of Q in reciprocal space and have high counting statistic at Q_{max},. the flat panel Perkin Elmer XRD 1611CP3 detector available at ID22 was used[85]

(Figure 2.6). The detector consists of CsI:Tl scintillator bonded to amorphous silicon, which acts as the active element of the detector.

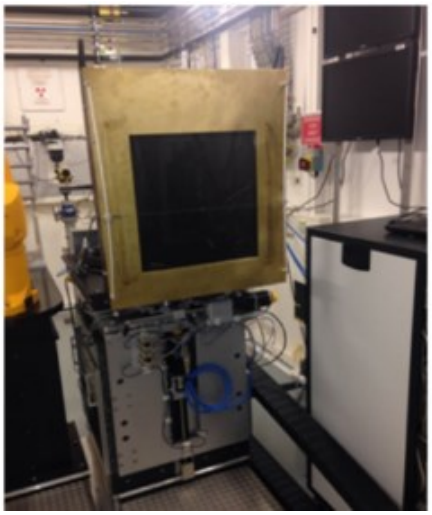

Figure 2.6 Picture of the 2D Perkin Elmer detector at ID22 (from website of the beamline)

In this case, several frames for a total counting time of 40 min were averaged for each measurement, reaching a $Q_{max} \approx 32$ Å^{-1}. Wavelength (≈ 70 keV), sample-detector distance and azimuthal integration parameters were calibrated on a LaB_6 reference (λ=0.17704 Å and sample-detector distance 379.3 mm for experiment CH-5900; λ=0.17219 Å and sample-detector distance 372.0 mm for experiment CH-6218). The detector mask was created with the program FIT2D[92] calibration and azimuthal integration were all performed using the program pyFAI[93].

After data reduction, the PDF for real space analysis was calculated in the form of the reduced PDF, G(r). This function is the product of the sine Fourier transform of the experimental total scattering function, S(Q), defined as[94]:

$$G(r) = 4\pi r[\rho(r) - \rho_0] = \frac{2}{\pi}\int_{Q_{min}}^{Q_{max}} Q[S(Q) - 1]\sin(Qr)\,\mathrm{d}Q$$

where ρ(r) is atomic pair density function and indicates the probability of finding an atom at a distance r from another atom, while ρ_0 is the atom number density. A positive peak in the G(r) pattern indicates a range of r values whereby the probability of finding interatomic vectors is greater than that determined by the number density, while the opposite holds for negative G(r) peaks. G(r) curves were computed using the PDFgetX3 program[95] using data up to Q_{max}= 27.0 Å^{-1} for experiment CH-5900 and Q_{max} = 26.0 Å^{-1} for experiment CH-6218. Structural models were fitted to the G(r) curves in small-box refinements using PDFgui[96]. The instrumental parameter Q_{damp} (=0.01) was determined fitting G(r) data collected on a LaB_6 reference in the same experimental conditions. PDF peaks in the low-r region were also fitted with Gaussian functions using the Origin software[97] to extract the position and FWHM.

The primary features of the X-ray diffraction patterns and PDF functions of the pyrochlore and related structure types will be presented in the next section.

At this stage it is clear that the pyrochlore structure is based on the fluorite structure type with a cell parameter $a_p = 2a_f$. This structural relationship can be directly visualized in a powder diffraction pattern. An example is displayed in Figure 2.7.

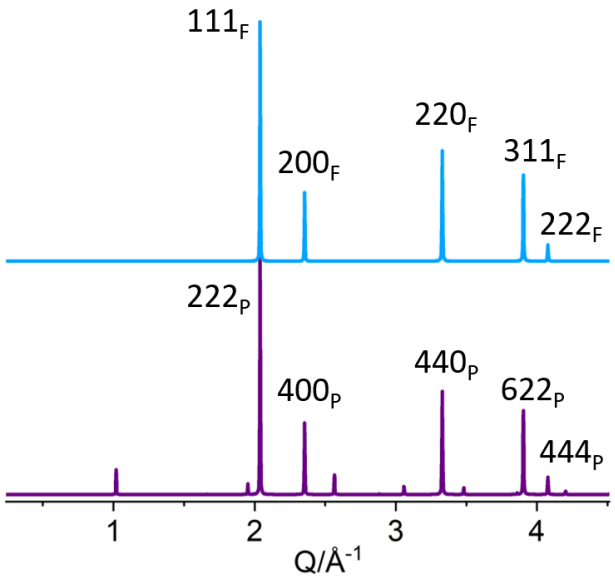

Figure 2.7 Simulated X-ray powder diffraction patterns of a defect fluorite (top, blue) and pyrochlore phase (bottom, violet) with $a_p = 2a_f$ and $Gd_2Zr_2O_7$ composition. 'Fluorite peaks' are indexed in each pattern with *hkl* Miller indices followed by a subscript indicating the structure type.

The most intense reflections in the pyrochlore diffraction pattern correspond to the reflections found in the fluorite pattern, but with doubled Miller indices. They are called 'fluorite peaks' and obey to the following condition (in the pyrochlore setting, s.g. $Fd\bar{3}m$)[47]:

$h + k = 4n$

hkl: $k + l = 4n$

$h + l = 4n$

The appearance of fluorite peaks in an X-ray powder diffraction pattern is a clear indication of an fcc packing of cations within the structure.

Beside the fluorite peaks, the presence of a set of weaker reflections in the pyrochlore diffraction pattern can be seen in Figure 2.7. These are designated 'pyrochlore' or 'superstructure peaks' and they arise from the additional ordering in the cation and anion sublattices of a pyrochlore with respect to a fluorite structure. The intensity of the pyrochlore peaks depends on the difference of the scattering power between A and B-cations, the scattering power of oxygen, the distribution of oxygen atoms and vacancies (i.e. concentration of anion Anti-Frenkel defects) and the fractional coordinate *x*O1[47].

The additional ordering allows for extra conditions[82,98]:

$h = 2n + 1$

hkl: or $h + k + l = 4n$

or $h, k, l = 4n + 2$

or $h, k, l = 4n$

Since all atoms in the pyrochlore structure occupy special positions, it is possible to ascribe specific class of reflections to certain atoms[47]. In particular, the subset of fluorite peaks that fulfils the condition

$$h = 4n + 2$$

hkl: $k = 4n + 2$

$$l = 4n + 2$$

derives from the scattering of cations at the A and B sites of the pyrochlore structure (e.g. 222_P, 622_P, 662_P …). Among the superstructure peaks, those with

$$h \neq 4n$$

hkl: $k \neq 4n$ and $h + k + l = 4n$

$$l \neq 4n$$

arise only from the oxygen sublattice (e.g. 220_P, 620_P, 642_P, 422_P…). Some of these reflections, such as 422_P, might be hardly visible by using X-rays as probe, while neutrons can allow a better contrast[31].

Simulated X-ray powder diffraction pattern of a defect fluorite, pyrochlore, C-type and weberite structure are shown in Figure 2.8. Those of pyrochlore and C-type look quite similar, even though different superstructure peaks arise in the C-type pattern with respect to the pyrochlore pattern. The orthorhombic symmetry of the weberite-type structure results in the appearance of more reflections in the diffraction pattern,

compared to the other cubic structures. Specifically, the typical fluorite peaks shared by all the fluorite-related structures, are split into two or three maxima in the weberite-type pattern[23].

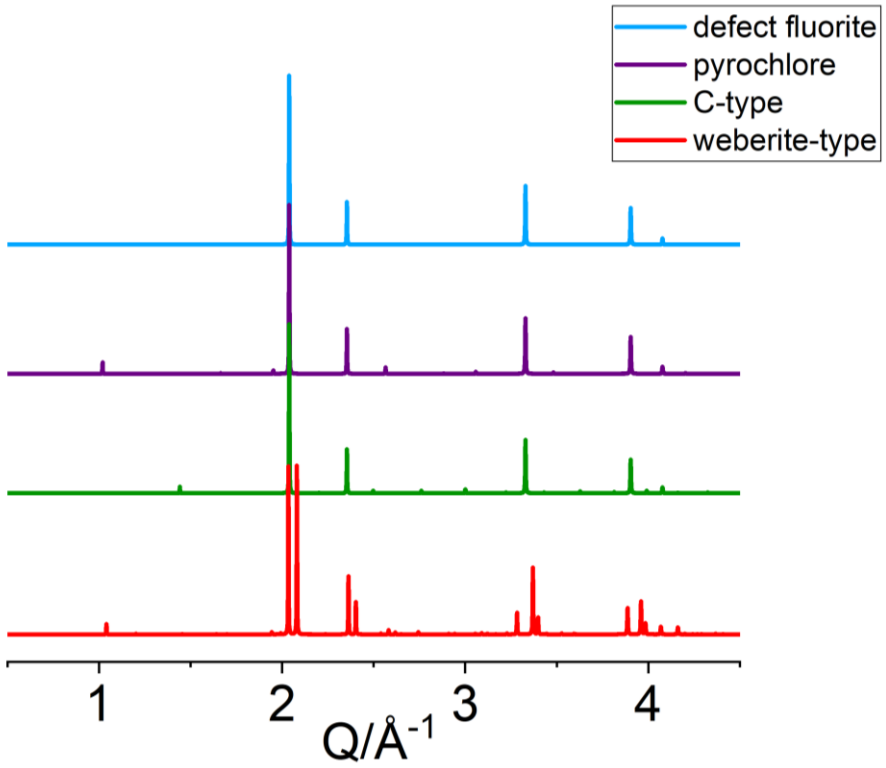

Figure 2.8 Simulated X-ray powder diffraction patterns of a defect fluorite, pyrochlore, C-type and weberite-type phase with $Gd_2Zr_2O_7$ composition and $a_p = a_c = b_{weberite\text{-}type} = 2a_f$. and $a_{weberite} \approx c_{weberite} \approx a_f\sqrt{2}$.

Figure 2.9 displays the simulated G(r) functions from X-ray scattering for a defect fluorite and pyrochlore structure in the low-r region. The two limiting values of *x*O1 (0.3125 and 0.375) were considered for the calculation of the pyrochlore pair distribution function.

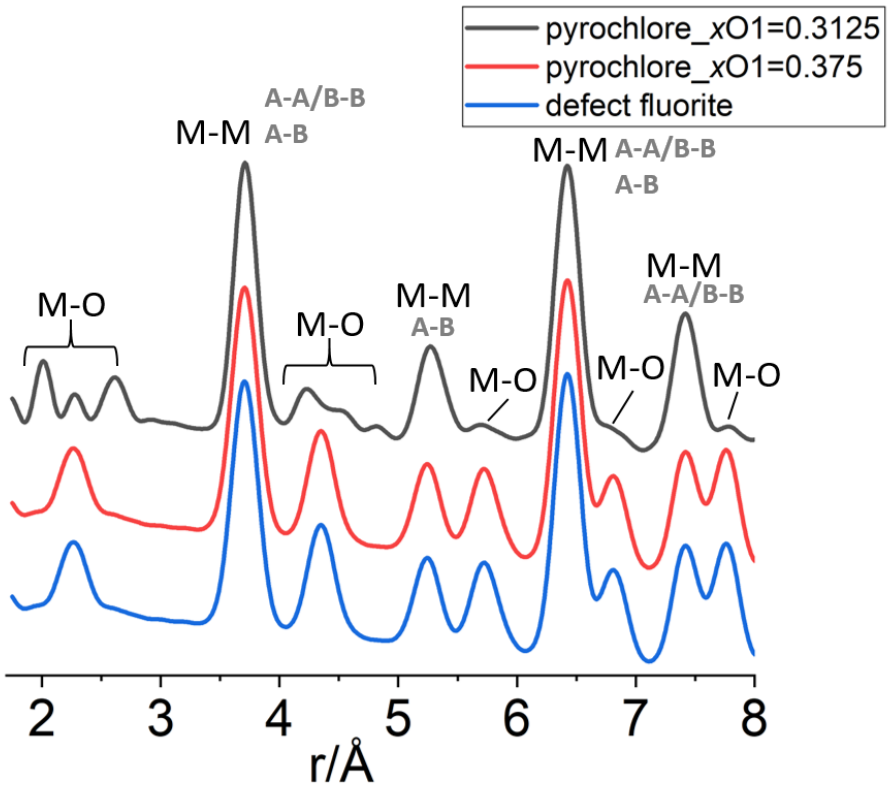

Figure 2.9. Simulated G(r) of pyrochlore structures with *x*O1=0.3125 and 0.375 and a defect fluorite structure with $Gd_2Zr_2O_7$ composition, *Qmax* = 30 $Å^{-1}$, and Uiso parameters of cations and anions set to the value of 0.006 $Å^2$. Metal-metal correlations are labelled M-M (with A-A/B-B and A-B contributions in grey), while metal-oxygen correlations are labelled M-O.

As one would expect, all metal-metal (M-M) correlations fall the under the same r value in all the G(r) functions shown in Figure 2.9. In this regard, it is worth remembering that cations are in special positions with fixed coordinates in both the defect fluorite and pyrochlore structure. The PDF of a pyrochlore structure with *x*O1=0.375, in particular, is indistinguishable from that of a defect fluorite structure with the same composition, having also the same metal-oxygen (M-O) correlations. This confirms that the two structural types are practically equivalent in terms of the positions of the atoms in the structure when *x*O1 in the pyrochlore structure is 0.375. In the opposite case, when *x*O1=0.3125, the metal-oxygen interatomic distances related to the A- and B-cations are different and the corresponding PDF peaks split and spread out. For example, the peak associated with the first M-O distance centered at ≈ 2.3 Å in the G(r) of the defect fluorite and pyrochlore structure with *x*O1=0.375 splits into three peaks at ≈ 1.9, 2.2 and 2.7 Å in the G(r) of the pyrochlore structure with *x*O1=0.3125. These peaks correspond to the first B-O1, A-O2 and A-O1 distances respectively. However, the most intense peaks (e.g. ≈3.7, 5.2, 6.4 and 7.4 Å) in all the simulated G(r) displayed in Figure 2.9 belong to metal-metal correlations. Indeed, X-rays are more sensitive to heavy metals than oxygen atoms in these oxide systems. As already stated, neutrons would allow a better contrast and even O-O correlations would be visible in a PDF from neutron scattering. Unfortunately, neutron scattering experiments were not performed, because all samples under investigation contain Gd that has the highest neutron absorption cross section of all elements in the periodic table.

Simulated G(r) functions from X-ray scattering of all the structural types cited in this work are presented in Figure 2.10.

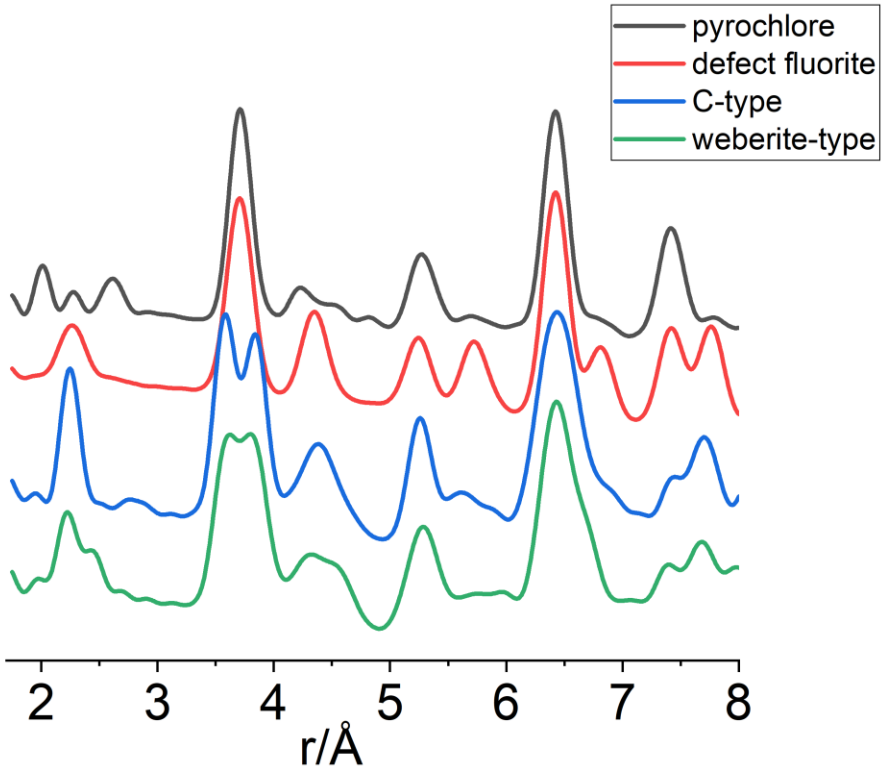

Figure 2.10. Simulated G(r) of a pyrochlore structure with *x*O1=0.3125, a defect fluorite, C-type and weberite-type structure with $Gd_2Zr_2O_7$ composition, *Qmax* = 30 $Å^{-1}$, and Uiso parameters of cations and anions set to the value of 0.006 $Å^2$.

Besides the changes in M-O correlations, a splitting of the metal-metal coordination shells occurs in the weberite-type and C-type structures when compared to the pyrochlore and defect fluorite. This can be easily visualized by looking at the PDF

peak at ≈3.7 Å in Figure 2.10. Some of the cations in the weberite type and C-type structure have variable positional coordinates (see Table 1.3 and 1.4). This creates additional M-M interatomic distances that are absent in the defect fluorite or pyrochlore structure.

Raman measurements

Micro-Raman spectroscopy was carried out using a Horiba LabRam HR evolution at the Dipartimento di Scienze della Terra "A. Desio" of the Università degli Studi di Milano (Figure 2.11). The spectrometer is equipped with a Nd-YAG 532 nm/100mW with Ultra Low Frequency (ULF) filters. Scattered light was collected by a 100X objective (NA aperture = 0.9) in backscattering geometry; a diffraction grating with 600 lines/mm and the hole set at 100 μm were used. The spectrum has been detected by a Peltier-cooled Charge Couple Detector. To balance signal to noise 2 accumulations for 30 seconds were collected. Instrument calibration was performed before each round of analysis using the peak at 520.70 cm-1 of a silicon wafer. After background subtraction, Raman bands were fitted with Gaussian functions using the Origin software[97] to extract values for frequency and FWHM.

Figure 2.11 Micro-Raman spectrometer supplied by Dipartimento di Scienze della Terra "A. Desio" (picture from the Department website)

The first-order Raman spectrum of pyrochlore and other fluorite-related structures will be considered. In this approximation, only long-wavelength phonons are scattered in a one-phonon process at the center of Brillouin zone (Γ-point), where $\boldsymbol{k}$ (or $\boldsymbol{Q}$, scattering vector) is zero[99,100]. These phonons can be classified in terms of their symmetry properties by factor group analysis[101,102]. For the pyrochlore structure with space group $Fd\bar{3}m$ (Z=8), point group O_h, atoms in sites *16c*, *16d*, *48f* and *8b*, the factor group analysis predicts a total of 26 normal modes at centre of Brillouin zone

$$\Gamma = A_{1g} + E_g + 2T_{1g} + 4T_{2g} + 3A_{2u} + 3E_u + 8T_{1u} + 4T_{2u}$$

One out of eight T_{1u} modes is associated with the three degrees of translation of the entire unit cell (acoustic) and is subtracted to find the total number of optic vibrational modes allowable. Looking at the O_h character table, the $7T_{1u}$ modes are IR-active and the A_{1g}, E_g and $4T_{2g}$ modes are Raman-active. The remaining modes

($2T_{1g}$, $3A_{2u}$, $3E_u$ and $4T_{2u}$) are inactive according to the selection rules of both IR and Raman spectroscopy[99]. The factor group analysis also allows the separation of each lattice mode per set of ions. Focusing on the Raman active modes, the *48f* oxygen (O1) of the pyrochlore structure is responsible for the A_{1g}, E_g and $3T_{2g}$ modes, while the *8b* oxygen (O2) is involved in just one T_{2g} mode[22]. Interestingly, since all Raman active modes are even modes of vibration and the cations occupy positions with centre of symmetry, they do not contribute to the Raman spectrum of an ideal pyrochlore structure[100]. At this point of the study, it is worth noting that the Raman spectroscopy served as direct probe of the anion sublattice of this class of materials where the X-rays were clearly more sensitive to the positions of the heavy metals and another valuable probe such as the neutron scattering was precluded for the high neutron absorption cross section of the natural abundant isotope of Gd.

As an example, the Raman spectrum of $Gd_2Ti_2O_7$ collected in this study is displayed in Figure 2.12.

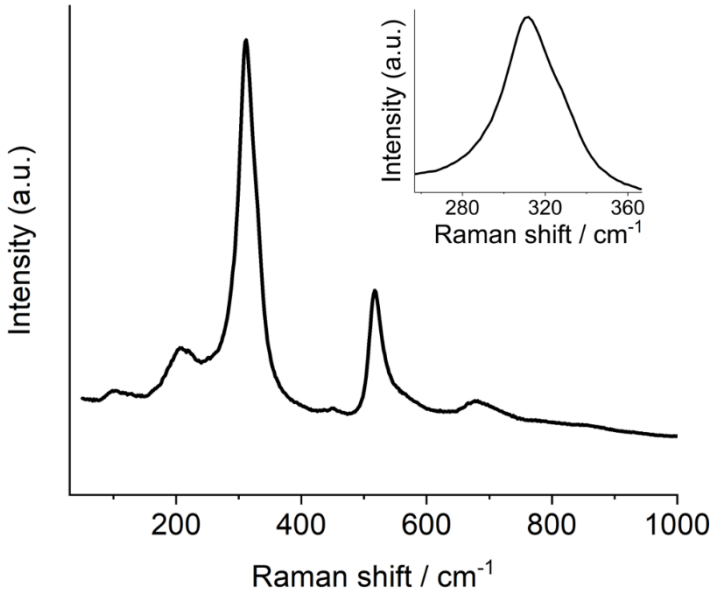

Figure 2.12 Raman spectrum of $Gd_2Ti_2O_7$ between 50 and 1000 cm^{-1}. A shoulder to the main band around 311 cm^{-1} can be noted at ≈ 330 cm^{-1} in the inset.

The vibrational modes of pyrochlores correspond to spectral bands that lie approximately in the range 200-600 cm^{-1} of the spectrum[103,104]. The fingerprints of the pyrochlore spectrum are two intense bands at about 300 and 500 cm^{-1} (Figure 2.12)[105]. As a matter of fact, the band at ≈ 300 comprises two vibrational modes, wavenumbers ≈ 311 and 330 cm^{-1} (see inset in Figure 2.12), which have been assigned to T_{2g} and E_g symmetry respectively, while the band at ≈ 500 cm^{-1} has been assigned to A_{1g} symmetry[106–110]. More details on the band assignment in the Raman spectrum of the pyrochlore structure will be given in the following chapter.

In the case of a fluorite compound (s.g. $Fm\bar{3}m$, Z=4, point group O_h, atoms at *4a* and *8c* sites), the factor group analysis predicts one T_{1u} IR-active mode and one T_{2g} Raman-active mode at the centre of the Brillouin zone. Also in this case, due to symmetry considerations, the oxygen atoms are the ones that, vibrating in antiphase, generate the Raman spectrum[111]. Consequently, the Raman spectrum of an ordered fluorite oxide is characterized by a single vibrational band[112] (Figure 2.13).

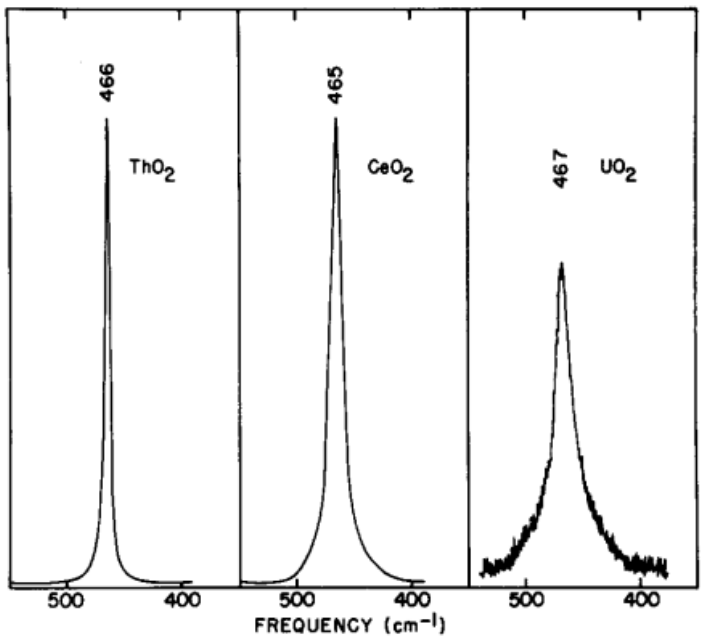

Figure 2.13 Raman spectrum of oxides with a fluorite structure, showing one vibrational band with T_{2g} symmetry [from Ref. 112].

The introduction of defects and disorder in the structure results in the breakdown of selection rules for the vibrational spectroscopy. In detail, the randomization of anions and vacancies in a defect fluorite compound leads to the complete broadening of the

band related to the T_{2g} mode and the Raman spectrum corresponds to a temperature-weighted density of states[49,100] (Figure 2.14).

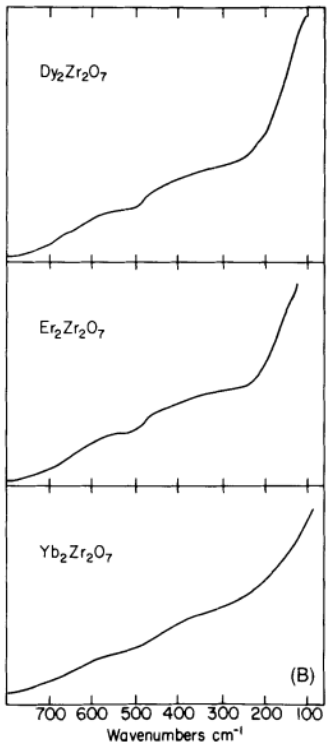

Figure 2.14 Raman spectrum of oxides with a defect fluorite structure, showing a broad continuous function [from Ref. 100].

The inherent lower symmetry of materials with a weberite-type or bixbyte structure compared to those with a pyrochlore or defect fluorite structure determines a more complex Raman spectrum. 24 modes are allowed in the Raman spectrum of a weberite-type compound ($5A_{1g} + 5B_{1g} + 7B_{2g} + 7B_{3g}$)[113], while 22 modes are predicted

for a C-type compound ($4A_g + 4E_g + 14T_g$)[114]. Examples for these structural types are shown in Figure 2.15.

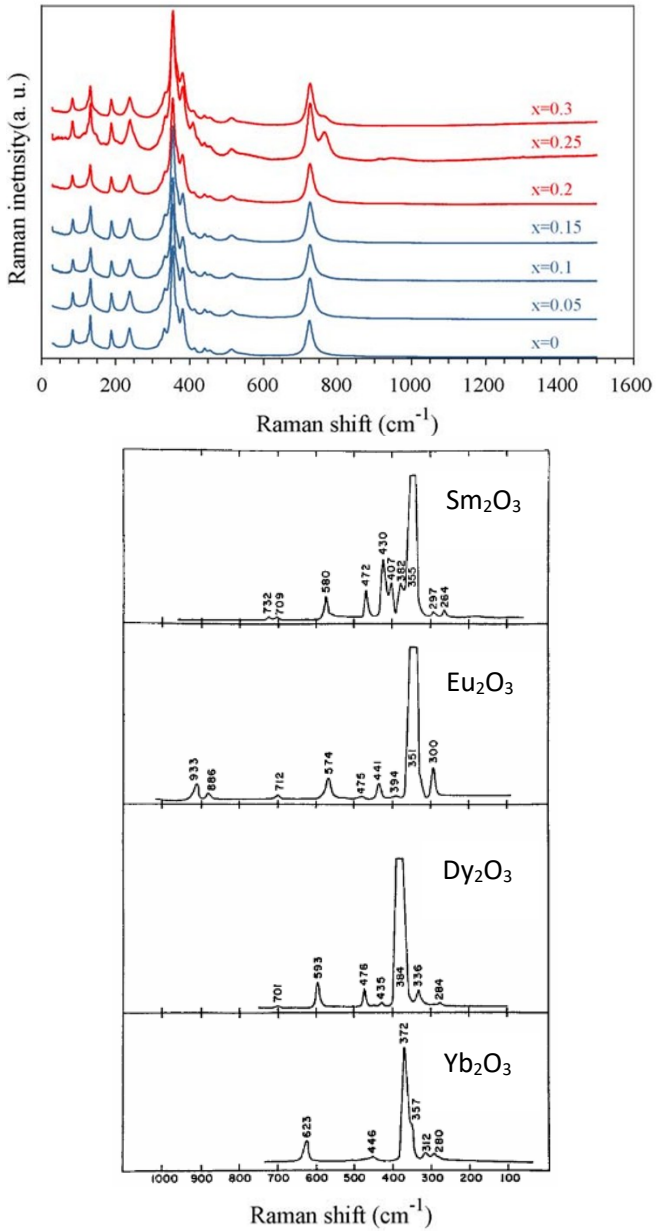

Figure 2.15 Raman spectra of (top) $La_{3-x}Sr_xTaO_{7-x/2}$ solid solution with weberite-type structure [from Ref. 115] and of (bottom) rare earth oxides with C-type structure [from Ref. 114].

Part 3

$Gd_2(Ti_{1-x}Zr_x)_2O_7$ solid solution

The following samples were synthesized by solid-state reaction starting from Gd_2O_3, TiO_2 and ZrO_2 as precursors.

Compound	Annealing cycles (#)
$Gd_2Ti_2O_7$	4
$Gd_2(Ti_{0.85}Zr_{0.15})_2O_7$	5
$Gd_2(Ti_{0.75}Zr_{0.25})_2O_7$	6
$Gd_2(Ti_{0.50}Zr_{0.50})_2O_7$	6
$Gd_2(Ti_{0.25}Zr_{0.75})_2O_7$	6
$Gd_2(Ti_{0.15}Zr_{0.85})_2O_7$	6
$Gd_2Zr_2O_7$	7

In this solid solution, the phase homogeneity seems to increase with Ti-content. As an example, the change in the laboratory diffraction patterns with annealing cycles for the $Gd_2Zr_2O_7$ sample is shown in Figure 3.1.

It is evident that at least three phases are present in the $Gd_2Zr_2O_7$ sample after the first annealing cycle (#1 in Figure 3.1). An increase in phase homogeneity is achieved when several annealing steps are repeated. A secondary phase can be recognized from the second step onwards (see the shoulder on the right side of the 222_P and 400_P peaks in Figure 3.1) and it has been regarded as another pyrochlore phase with a different cell constant and composition with respect to the primary phase.

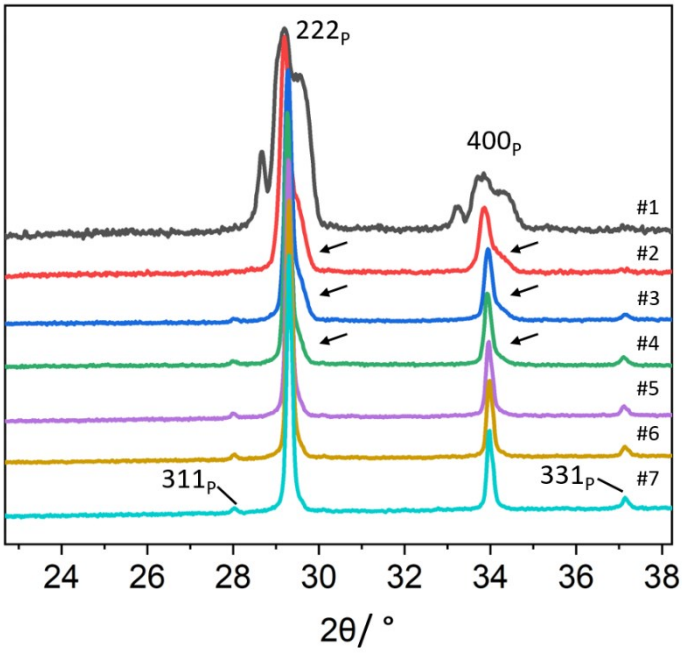

Figure 3.1 Evolution of the 222_P and 400_P reflections of $Gd_2Zr_2O_7$ at different annealing cycles (#n) (subscript 'P' indicates the pyrochlore structure type). XRD patterns were normalized and offset on the Y axis. Black arrows highlight the presence of the secondary phase. Note the growth of the 311_P and 331_P superstructure peaks at $2\theta \approx 28°$ and 37° respectively.

The changes in the weight fractions and cell constants for the primary phase (phase 1) and secondary phase (phase 2) in the $Gd_2Zr_2O_7$ sample are plotted in Figure 3.2. Cell constants and weight fractions of the phases of interest were extracted from Rietveld refinements of powder patterns with GSAS software[90,91]. As the number of annealing cycles increases, the weight fraction of the secondary phase decreases and that of the primary phase increases accordingly (Figure 3.2a). A third phase, with the lowest weight fraction (Figure 3.2a, blue triangle), readily disappears after the 2nd annealing cycle and the cell constants appear to converge towards a common value

(Figure 3.2b). These results indicate that several annealing cycles, with intermitting grinding and re-pelletizing, are needed for the production of a homogeneous $Gd_2Zr_2O_7$ compound.

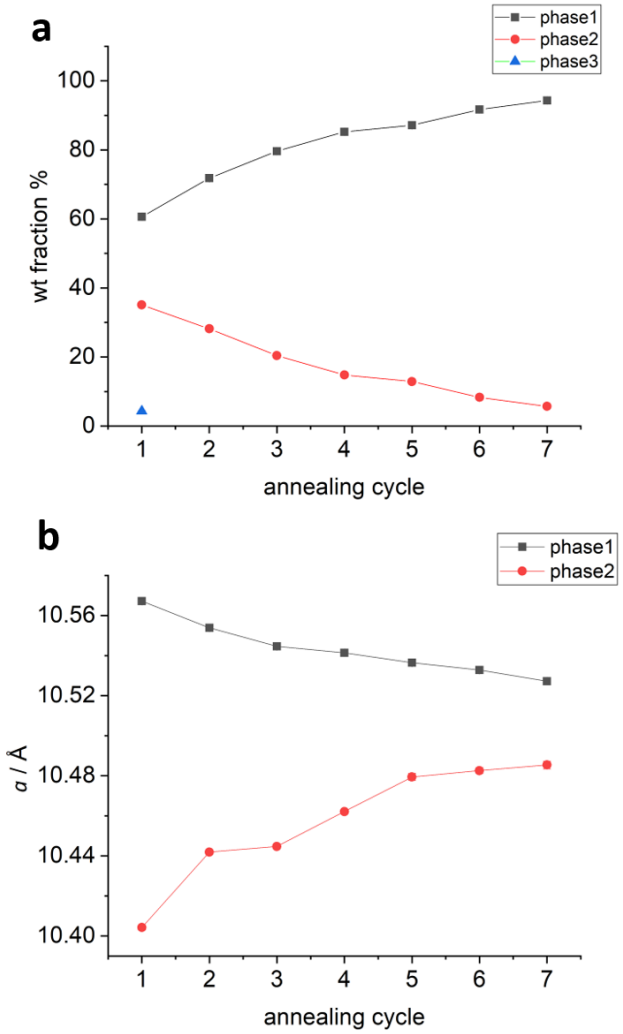

Figure 3.2. (**a**) weight fraction % of different pyrochlore phases in $Gd_2Zr_2O_7$ sample and (**b**) lattice constant of these phases as a function of # annealing cycle.

In the case of the $Gd_2Ti_2O_7$ sample a good phase homogeneity is achieved after just one annealing cycle (see Figure 3.3).

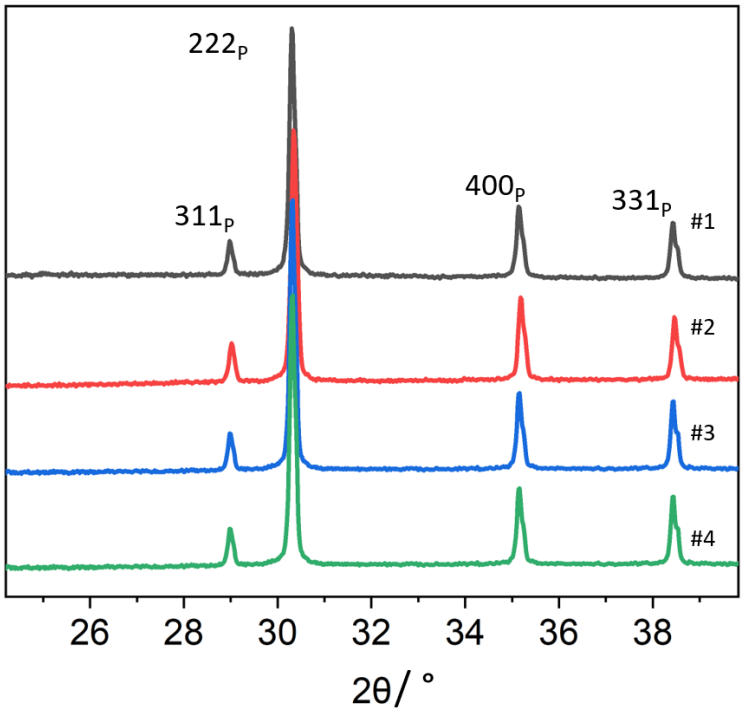

Figure 3.3 Evolution of the 222_P and 400_P reflections of $Gd_2Ti_2O_7$ at different annealing cycles (#n). XRD patterns were normalized and offset on the Y axis. 311_P and 331_P superstructure peaks at $2\theta \approx 29°$ and 38.5° respectively are clearly visible after the first cycle.

The solid-state synthesis was employed to prepare all the samples in the context of this work. The method is simple, since all the reactants are easily found in the form of metal oxides and the procedure can be easily implemented[116]. However, it requires long reaction times at high temperatures (e.g. 1500 °C) with intermediate steps in which the reaction mixture is grounded and then re-pelletized to ensure homogeneity.

Such a procedure could be unfeasible for an industrial scale process. As confirmed by the present thesis, a homogeneous sample with the desired crystalline phase is not always straightforward to obtain by solid-state synthesis. Indeed, an equilibrium distribution of cations in solid-state reactions is difficult to achieve[5]. Given that the reactants were all in the form of polycrystalline powders with micrometric size of the crystallites, the reaction rates were limited by the diffusion of cations at the reaction interface[117]. Clearly, the composition of the desired material plays an important role. Of all the synthesized compositions, those close to the $Gd_2Zr_2O_7$ endmember were particularly challenging, because required the longest reaction times. Similar observations were made by Laverov and colleagues. In their work on synthetic pyrochlore and garnet materials, they showed that the crystallization of the pyrochlore phase is slow in the $Gd_2O_3 – ZrO_2$ system, while higher reactions rates are observed for the $Gd_2O_3 – TiO_2$ system[118]. These findings are consistent with the results of Reynolds and coworkers. They prepared $Gd_2Zr_2O_7$ by standard solid-state synthesis and a 30 days-long protocol of annealing was employed with the intermediate grindings. Even after such long reaction time, asymmetry in peak shapes was detected by synchrotron X-ray diffraction and interpreted as residual inhomogeneity in the sample[77]. In recent years, the difficulty in obtaining a homogeneous product with a pyrochlore or defect fluorite structure by solid-state synthesis has been related to the persistence of disordered weberite-type nanodomains at the local scale in these oxides[119,120]. As will be clarified, the

weberite-type structure can effectively describe the local atomic arrangement in disordered pyrochlore oxides.

An in depth study of the phase formation in these pyrochlore systems was beyond the scope of this thesis. The use of electron microprobe analysis (EMPA) and scanning electron microscopy (SEM) after each annealing step would have certainly complemented the diffraction results and provided a more precise picture of the phase inhomogeneity and morphology. The solid-state synthesis was chosen for it is a standard technique for preparing highly crystalline oxide materials and the purpose of this study was to follow the evolution of the structural disorder and defect chemistry of pyrochlore oxides only as a function of composition. As a matter of fact, materials produced by solid-state synthesis are employed as references when studying the effect of other sources of structural disorder such as mechanical milling or ion irradiation[121–123].

An alternative approach to the solid-state reaction might be the sol-gel method. In principle, homogeneity at the atomic scale can be attained by producing a gel from a solution of the selected metal ions. Burning the gel at about 500 °C leads to a nanocrystalline phase after just one annealing step. Obviously, high temperature sintering is always required for obtaining a highly crystalline compound with the desired phase. Additional samples with the same composition of those employed in this study have been produced by this technique and preliminary investigations using synchrotron High-resolution X-ray diffraction (HR-XRD) showed a greater phase homogeneity of the sol-gel samples compared to those synthesized by solid-state

reaction. Further studies are needed in order to compare different methodologies and to understand the kinetic of these reactions. The samples synthesized by the sol-gel method will be the subject of an upcoming work.

The dissertation continues with the structural study of $Gd_2(Ti_{1-x}Zr_x)_2O_7$ solid solution by synchrotron HR-XRD, Raman spectroscopy and PDF analysis.

The average structure of all $Gd_2(Ti_{1-x}Zr_x)_2O_7$ compositions is that of a pyrochlore throughout the solid-solution, as demonstrated by the appearance of superstructure peaks in the HR-XRD patterns (see Fig 3.4 superstructure peaks at $2\theta \approx 3.4, 6.6, 8.7, 10.4, 11.8, 13.1$ with $\lambda = 0.354176$ Å). Therefore, no phase transition occurs at the long-range scale in the $Gd_2(Ti_{1-x}Zr_x)_2O_7$ series. However, the substitution of Ti^{4+} with Zr^{4+} clearly affects the structure of these materials. Firstly, the cell expands on Zr-substitution, because Zr^{4+} is bigger in size than Ti^{4+}. This leads to an increase of the cell parameter and to a shift of diffraction peaks to lower 2θ angles (Fig 3.4). Secondly, the X-ray scattering power of Zr^{4+} is greater than Ti^{4+} (Zr has more electrons). This difference is primarily reflected in the intensity of superstructure peaks, which become weaker and weaker as Zr^{4+} replaces Ti^{4+} (Fig 3.4, see for example the peak 111_P at $2\theta = 3.45°$).

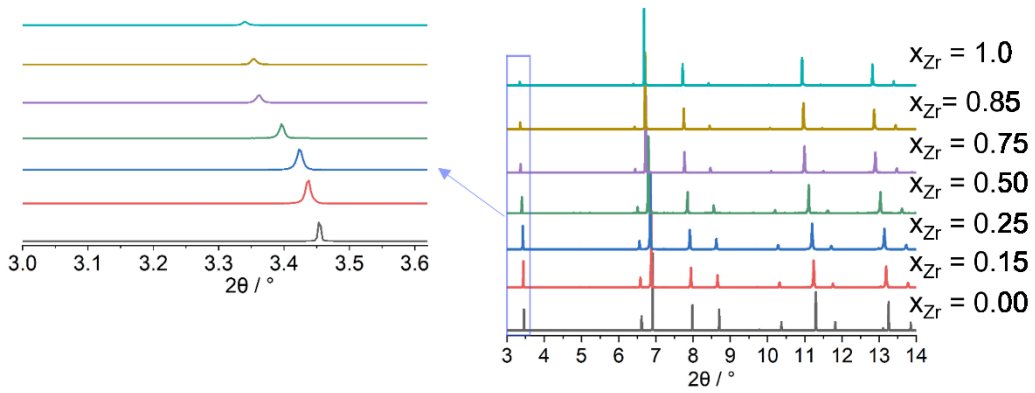

Figure 3.4 HR-XRD patterns of $Gd_2(Ti_{1-x}Zr_x)_2O_7$ series between 3 and 14 degrees. The evolution of the superstructure peak 111_P between 3 and 4 degrees is highlighted.

All powder patterns were analyzed through Rietveld refinements to extract structural parameters. A disordered pyrochlore model was employed for all compositions. The term 'disordered' refers to the introduction of anion Anti-Frenkel and cation antisite defects within the ideal pyrochlore structure. The structural model was constructed starting from the coordinates given in Table 1.2, setting 2. Anion Anti-Frenkel defects were introduced by refining the occupancy of both *8a* (O3) site and *48f* (O1) site. To ensure that stoichiometry changes were avoided, the occupancy of O1 was constrained to that of O3. Taking into account the multiplicity of both sites (48 and 8 for O1 and O3 respectively), the constraint was defined in GSAS software as $-\Delta o.f.(O1) = 6\Delta o.f.(O3)$ (where $\Delta o.f.$ is the variation of the site occupation factor). Attempts to vary also the oxygen occupancy at the *8b* site (O2) brought to o.f.(O2) slightly larger than 1. Therefore, these tests will not be considered in the following discussion. Moreover, the mixing of cations *via* cation antisite defects was allowed. Since a single X-ray diffraction experiment is not sufficient to determine the distribution of three cations over two different crystallographic sites[47], it was assumed that only Zr^{4+} would replace Gd^{3+} at the A site (*16d*) and vice versa. For this purpose, two additional ions were introduced in the structural model, a zirconium atom at the A-site (Zr_A) and a gadolinium atom at the B-site (Gd_B). Their occupancy was constrained to that of the parent atom to avoid stoichiometry changes and allowed to vary. Specifically, the constraints were set as $-\Delta o.f.(Zr_B) = \Delta o.f.(Zr_A)$ and $-\Delta o.f.(Gd_A) = \Delta o.f.(Gd_B)$. The lattice parameter (*a*), the *x* coordinate for O1 (*x*O1)

and three isothermal displacement parameters (one for each cation plus one for the oxygen atoms) were refined as well.

The phase inhomogeneity described above resulted in some sample dependent peaks asymmetries. Similar effects were already detected in patterns collected at synchrotron radiation sources by other authors while investigating the $Gd_2Zr_2O_7$ composition prepared by solid state synthesis. The asymmetry was interpreted as residual sample inhomogeneity caused by poorly crystalline defect fluorite material and modelled using an additional cubic fluorite phase in the refinements[72,77]. In the present work, it was not possible to determine with absolute certainty whether the asymmetry affected both the structure (fluorite) and superstructure (pyrochlore) peaks and, thus whether the secondary phase adopted a defect fluorite or pyrochlore structure. For convenience, the patterns were refined using two pyrochlore phases, with different lattice constants and with the structural parameters *x*O1 and U_{iso} constrained to be the same. In addition, the profile terms of the two phases were allowed to be different in the Rietveld refinements to account for the different peak shape. In all samples, either the second phase has a very small weight fraction or the cell constants of the two phases are very close to each other. Selected portions of two phases refined patterns are shown in Figure 3.5. Examples of Rietveld refinements are plotted in Figure 3.6, while the results of all Rietveld refinements are summarized in Table 3.1 and the change of the relevant structural parameters is displayed in Figure 3.7.

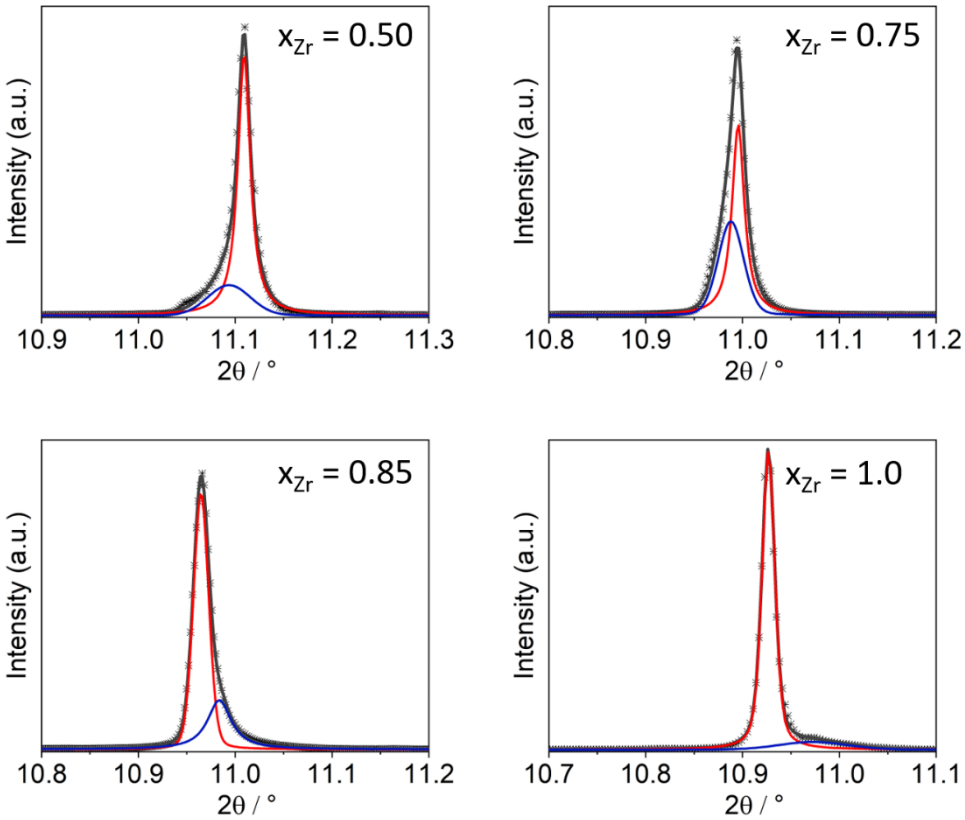

Figure 3.5 Close-up view of 440_P reflection in selected HR-XRD patterns of $Gd_2(Ti_{1-x}Zr_x)_2O_7$ solid solution. Cross symbols represent the observed pattern; the dark grey solid line is the total calculated profile by Rietveld refinement, while solid red and blue lines are the calculated profile for Phase 1 and Phase 2 respectively.

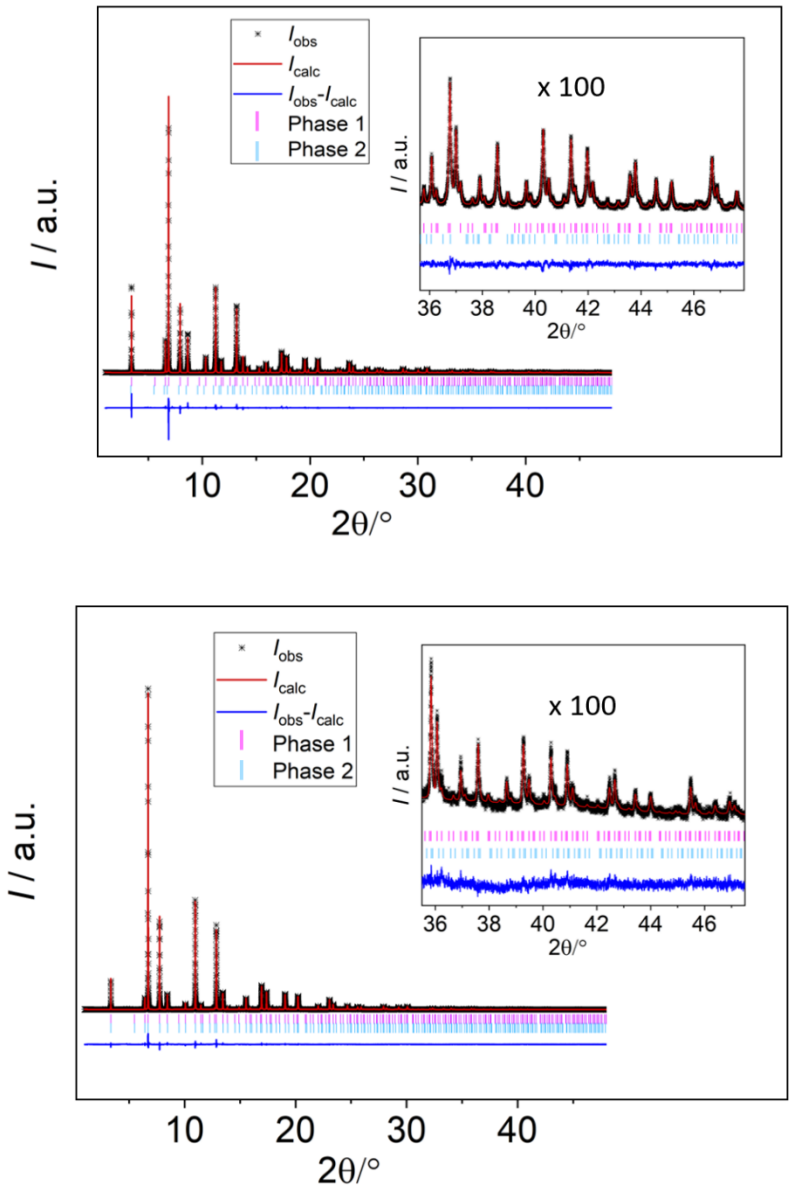

Figure 3.6 Rietveld refinements of synchrotron HR-XRD profiles of (top) $Gd_2(Ti_{0.85}Zr_{0.15})_2O_7$ and (bottom) $Gd_2(Ti_{0.15}Zr_{0.85})_2O_7$ samples

Table 3.1 Structural parameter derived from Rietveld refinements of HR-XRD patterns of $Gd_2(Ti_{1-x}Zr_x)_2O_7$ solid solution. Estimated standard deviation values are in parentheses. Those of weight fractions are not indicated because underestimated by the software.

xZr		**0**	**0.15**	**0.25**	**0.50**	**0.75**	**0.85**	**1.0**
Phase 1 s.g. $Fd\bar{3}m$	Weight Fraction %	94.3	99.9	98.0	79.2	57.9	70.8	89.6
	a / Å	10.178215(8)	10.23104(3)	10.26928(3)	10.35152(2)	10.45829(3)	10.48699(3)	10.52304(2)
Phase 2 s.g. $Fd\bar{3}m$	Weight Fraction %	5.7	0.01	2.0	20.7	42.1	29.2	10.4
	a / Å	10.232(3)	10.42(2)	10.3372(8)	10.3659(2)	10.46544(6)	10.4690(1)	10.4790(6)
*x*O1		0.3260(2)	0.3279(2)	0.3294(2)	0.3337 (2)	0.3415(2)	0.3438(2)	0.34698(4)
o.f.(O3)		0	0.06(1)	0.08(1)	0.20(1)	0.27(1)	0.338(9)	0.40(1)
o.f.(Zr_A)		0	0	0	0	0.026(1)	0.045(1)	0.048(2)
U_{iso} / $Å^2$	A	0.00447(3)	0.00449(4)	0.00536(5)	0.00918 (6)	0.01198(6)	0.01203(6)	0.01135(8)
	B	0.00372(7)	0.0040(1)	0.0055(1)	0.0090(1)	0.0144(1)	0.0165(1)	0.0182(2)
	O	0.0030(3)	0.0034(4)	0.0052(5)	0.0098(6)	0.0233(7)	0.0236(6)	0.0233(9)
wRp(%)		11.5	9.5	9.2	8.4	7.2	6.8	7.6

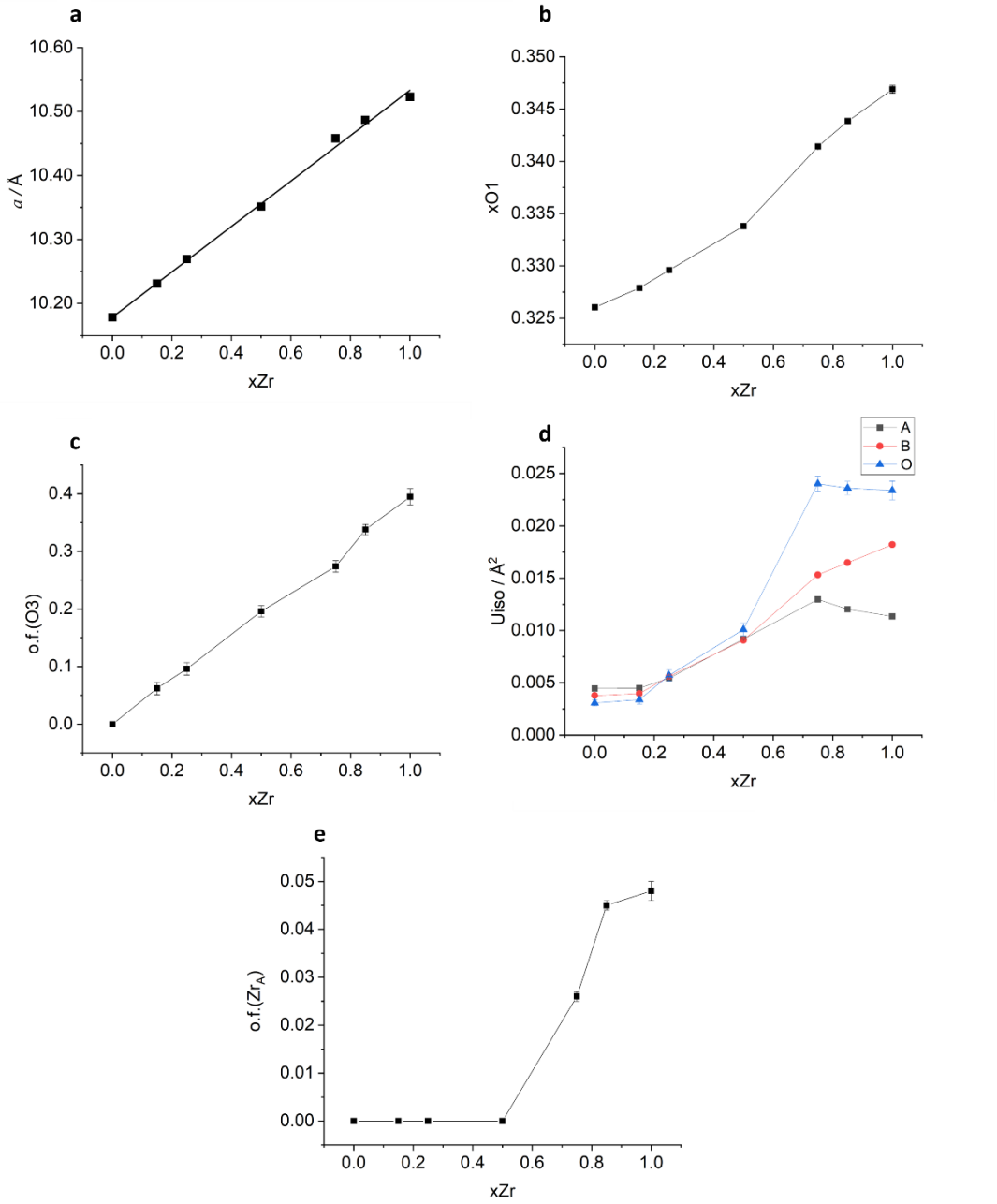

Figure 3.7 (**a**) lattice constant, (**b**) x-coordinate of O1, (**c**) occupancy factor of O3 site, (**d**) U_{iso}·and (**e**) occupancy factor of Zr at the A site as a function of Zr-content in $Gd_2(Ti_{1-x}Zr_x)_2O_7$ solid solution. Solid line in plot (a) is a linear fit.

The lattice constant in Figure 3.7a is calculated as weighted average of those of Phase 1 and Phase 2. Since Phase 2 has either a small weight fraction or a lattice constant quite close to that of Phase1, it could be easily verified that this trend is identical to that obtained with the lattice constants of Phase 1 alone. The trend is linear[47] and a similar increase is displayed by the *x*O1 coordinate (Fig. 3.7b) and the occupancy factor of O3 (Fig. 3.7c). The isothermal displacement parameters (U_{iso}) stay almost constant for the first Ti-rich compounds and then significantly increase for the Zr-rich compositions (Fig. 3.7d), especially those of oxygen atoms. An interesting trend is shown in Figure 3.7e for the occupation factor of Zr at the A-site (o.f.(Zr_A)). As can be seen, the concentration of Zr atoms at the A-site is practically zero for all compositions up to x_{Zr} =0.50. Attempts to refine o.f.(Zr_A) in those compositions with $x_{Zr} \leq 0.50$ yielded unphysical results and, for this reason, o.f.(Zr_A) was kept at zero. For $x_{Zr} > 0.50$, there is an abrupt boost of o.f.(Zr_A). However, the absolute values of o.f.(Zr_A) remain minimal. The change in *x*(O1), o.f.(O3) and U_{iso} with x_{Zr} detected by Rietveld refinements points to a progressive structural disordering in the $Gd_2(Ti_{1-x}Zr_x)_2O_7$ solid solution with increasing Zr-content. As described in Part 1, O1 is displaced in a pyrochlore structure from the position it would have in a defect fluorite structure (3/8, 1/8, 1/8), and 'relaxes' towards the vacant O3 site, providing electrostatic shielding to its neighboring two B-cations with a limiting *x*O1= 0.3125[11] (see also Part 1). In the $Gd_2(Ti_{1-x}Zr_x)_2O_7$ series, O1 moves upon Zr-substitution away from the vacancy O3 as this is gradually filled and its *x* coordinate (*x*O1) goes from 0.3260 in $Gd_2Ti_2O_7$ to 0.34698 in $Gd_2Zr_2O_7$ (see Fig. 3.7b).

As stated before, the rate of *x*O1 shift appears to be constant in the whole compositional range. This is in line with a similar behavior observed in related $Gd_2(Sn_{1-x}Ti_x)_2O_7$ and $Y_2(Sn_{1-x}Ti_x)_2O_7$ solid solutions, where *x*O1 changes linearly with the composition[25]. In those cases, the linear change in *x*O1 was associated to the more ordered nature of the structures under investigation (limited variation of *x*O1 and o.f.(O3)) in contrast to zirconate analogues. In fact, for $Y_2(Sn_{1-x}Zr_x)_2O_7$ and $Y_2(Ti_{1-x}Zr_x)_2O_7$ the *x*O1 shift follows a quadratic relation which suggests a rapid increase in disorder for Zr-rich samples[25,47]. However, it is worth noting that the $Y_2Zr_2O_7$ endmember is defect fluorite at the average scale. The same quadratic trend for xO_{48f} was found by Hess and co-workers in $Gd_2(Ti_{1-x}Zr_x)_2O_7$ solid solution[70]. In that case, the samples were annealed at 1600°C, which is beyond the temperature for the pyrochlore to defect fluorite transition in $Gd_2Zr_2O_7$ (1530 °C)[11,83]. For this reason, the long-range structure of the Zr-endmember was defect fluorite and the value of *x*O1 was only extrapolated from the data. Nevertheless, it was still displaced from 0.375 to a value close to the one refined by Moriga and co-workers in a single crystal investigation of $Gd_2Zr_2O_7$ (0.4089, considering setting 1, A-cations at the origin, *16c* (0,0,0))[70,124].

As anticipated, the O1 site in $Gd_2(Ti_{1-x}Zr_x)_2O_7$ is gradually depleted of its oxygen-content, while the o.f.(O3) steadily increases and o.f.(O2) is kept fixed at full occupancy. This is physically reasonable since O3 site is the nearest neighbour of O1 and studies on oxygen migration in pyrochlores have shown that a *48f* → *48f* hopping pathway *via* vacant *8a* sites is the most energetically favorable[43,45,125].

Again, this result is in accordance with previous investigation on $Y_2(Sn_{1-x}Zr_x)_2O_7$ and $Y_2(Ti_{1-x}Zr_x)_2O_7$ systems[25,47]. Furthermore, the gradual occupation of the vacant O3 site leads to an increase in the average coordination number of cations at the B site of the structure (from 6 to 7). It is likely that, at the local scale, the Zr^{4+} ions are those that become 7-fold coordinated rather than Ti^{4+}[72,121,126].

Other features concerning the structural disorder, which are not fully captured by the disordered pyrochlore model, affect the change of isothermal displacement parameters. It is worth remembering that all patterns were recorded at 90 K with the purpose of minimizing the contribution of thermal motion (dynamic disorder) to the diffraction patterns. Therefore, the increase in U_{iso} for Gd, Zr/Ti and O atoms with Zr-content (Figure 3.7d) suggests an increase in the static structural disorder[127,128]. This evidence, together with the randomization of anions through the formation of Anti-Frenkel defects, points to the fact that the long-range structure of $Gd_2(Ti_{1-x}Zr_x)_2O_7$ compounds is approaching the defect fluorite on Zr-substitution. However, if one tries to refine the occupancy of Zr^{4+} at the A site (o.f.(Zr_A)) of the structure, the obtained values are almost negligible even for the $Gd_2Zr_2O_7$ endmember. Looking at the trend in o.f.(Zr_A) (Figure 3.7e), one can see how the cation mixing between the A and B sites only occurs in the most Zr-rich compositions of the phase diagram with a maximum value for o.f.(Zr_A) of 0.05. The multiplicity of the A site, as that of the B site, is 16 and this means that only ~0.8 Zr^{4+} ions per cell form cation antisite defects with Gd^{3+} in $Gd_2Zr_2O_7$. It appears that the disordering process induced by chemical substitution in the $Gd_2(Ti_{1-x}Zr_x)_2O_7$

solid solution is dominated by anion Anti-Frenkel defects, while cation antisite defects have only a marginal role.

To further investigate the evolution of the long-range structure of $Gd_2(Ti_{1-x}Zr_x)_2O_7$ compositions upon Zr-substitution, having at the same time a first insight at the local scale, Raman spectra were recorded.

The Raman spectra of $Gd_2(Ti_{1-x}Zr_x)_2O_7$ samples are presented in Figure 3.8, where the observed vibrational modes are labelled from M1 to M7. The variation in frequency as obtained by fitting the bands with Gaussian functions is plotted in Figure 3.9, while selected fits are shown in Figure 3.10. The experimental spectra recorded in this study reproduce quite well those already reported in the literature for the $Gd_2(Ti_{1-x}Zr_x)_2O_7$ solid solution[69,70,82,129–132]. To identify the relevant bands that change upon Zr-substitution, one may-focus on the spectrum of $Gd_2Ti_2O_7$, which has the sharpest lines among all the spectra. As shown in Figure 3.8, the weak feature at ≈113 cm^{-1} (M1) in the spectrum of $Gd_2Ti_2O_7$ sharpens, while the band situated at ≈212 cm^{-1} (M2) appears to broaden on Zr-substitution. The most intense peak centered at ≈311 cm^{-1} (M3) also experiences an appreciable broadening with increasing xZr. A band centered at ≈450 cm^{-1} (M4) is hardly visible in the spectrum of $Gd_2Ti_2O_7$. However, as the Zr-content increases, M4 rises and shifts towards lower frequencies (i.e., is red-shifted), until it becomes one of the most prominent features in the Raman spectrum of $Gd_2Zr_2O_7$ at ≈400 cm^{-1}.

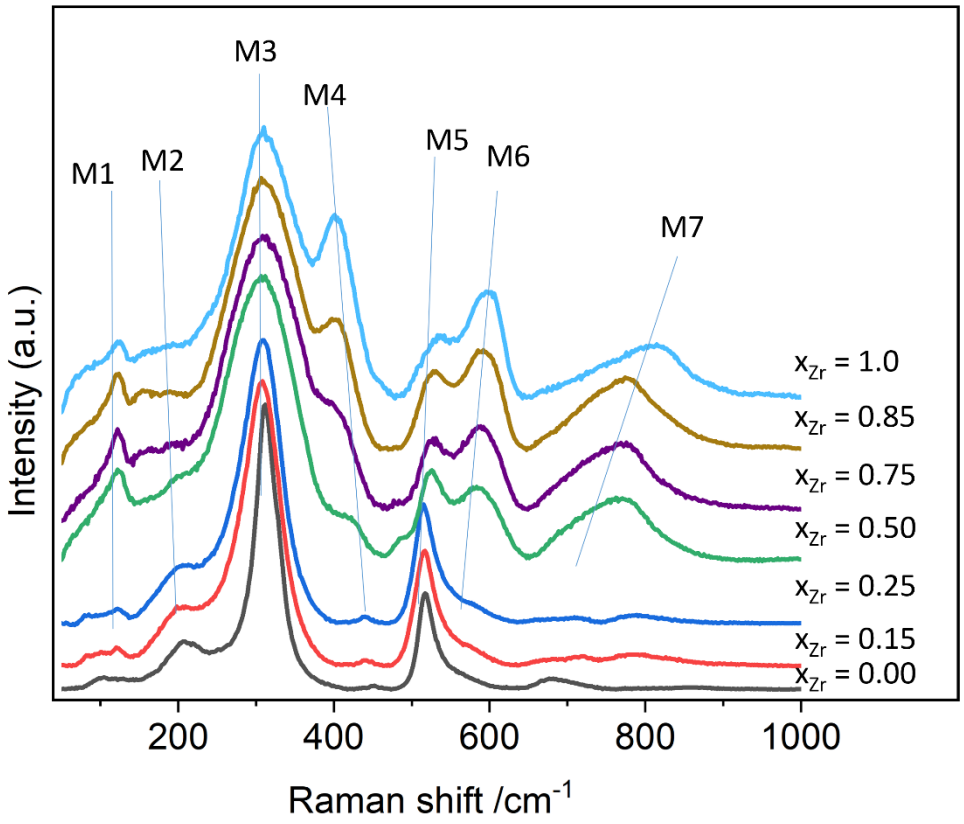

Figure 3.8 Raman spectra of $Gd_2(Ti_{1-x}Zr_x)_2O_7$ solid solution between 50 and 1000 cm^{-1} offset on the Y axis. After background subtraction, each spectrum was normalized between 0 and 100. The observed vibrational bands are labelled from M1 to M7.

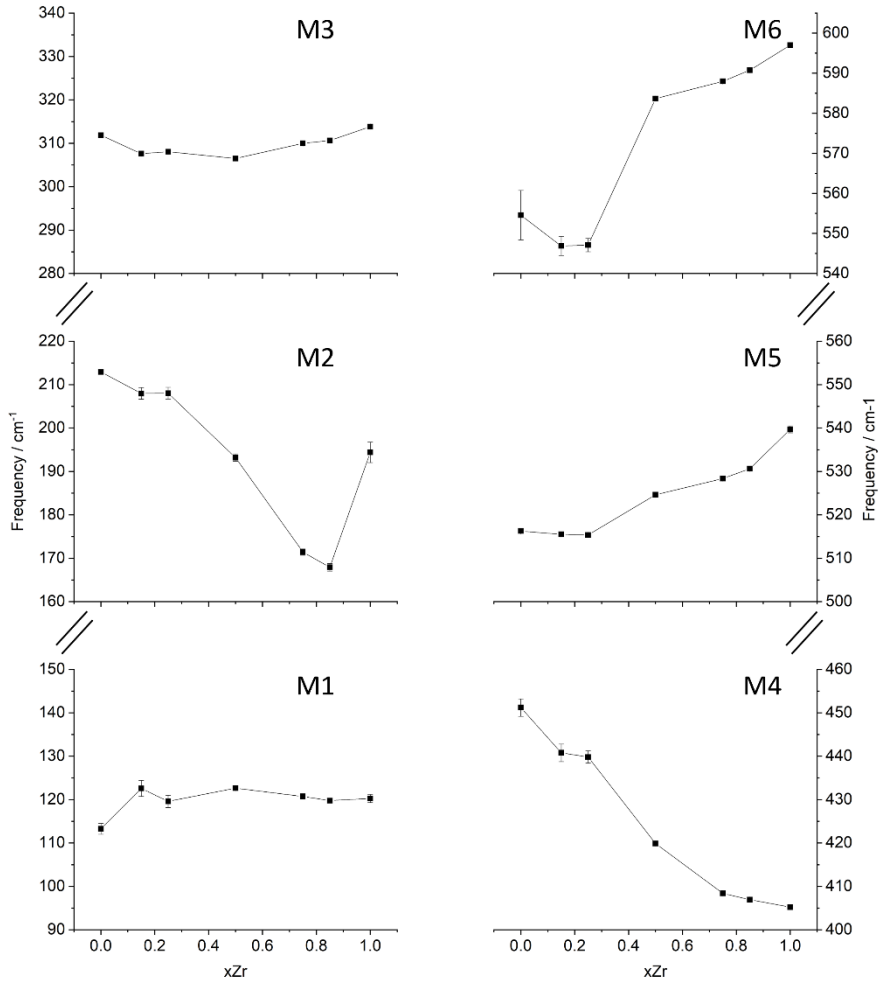

Figure 3.9 Frequency of vibrational bands in the Raman spectra of $Gd_2(Ti_{1-x}Zr_x)_2O_7$ solid solution as a function of Zr-content.

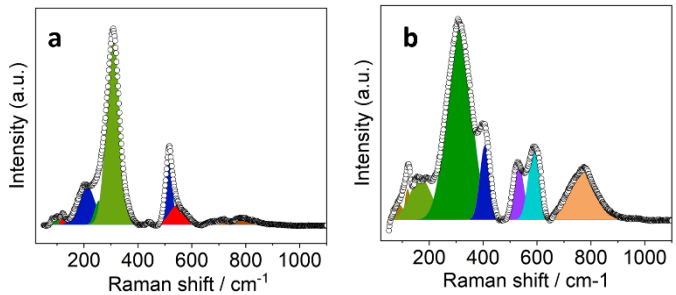

Figure 3.10 Selected fits with Gaussian functions of Raman bands in the spectra of compositions with xZr (**a**) 0.15 and (**b**) 0.85.

The lines at ≈516 cm^{-1} (M5) and ≈550 cm^{-1} (M6) are both blue-shifted with increasing Zr-content. However, their behavior regarding intensity is different. Specifically, while the intensity of M5 decreases, the intensity of M6 increases (see Figure 3.11). A subtle spectral feature is present in the spectrum of $Gd_2Ti_2O_7$ around 690 cm^{-1} (M7). It seems to split into two broad and weak bands for x_{Zr} = 0.15, 0.25, and then suddenly grows for x_{Zr} = 0.50 while being blue-shifted.

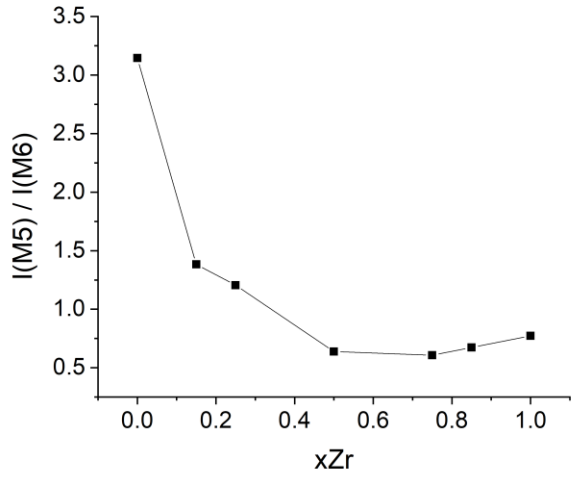

Figure 3.11 Intensity ratio between Raman bands M5 and M6 in the $Gd_2(Ti_{1-x}Zr_x)_2O_7$ series as a function of Zr-content.

It was mentioned in Part 2 that the vibrational modes of pyrochlores correspond to spectral bands that lie approximately in the range 200-600 cm^{-1} of the spectrum[103,104]. The assignment of Raman bands to the corresponding lattice modes has been done in previous studies by measuring polarized Raman spectra on single crystals and/or by theoretical calculations[104,106,107,109,133]. From the experimental point of view, no spectrum completely fulfils the selection rules under light polarization[108]. Nonetheless, there is a general agreement on the assignment of the most intense bands, M3 and M5, which are the fingerprints of the pyrochlore spectrum[105]. The peak M3 is actually consisting of two overlapping modes, T_{2g} and E_g, which are placed at 311 and 330 cm^{-1} respectively and involve O1 at the *48f* site through the Ti-O stretching and O-Ti-O bending[104,107–110,134,135]. Gupta and coworkers interchanged their frequencies[133,136,137]. The band M5 has also been assigned to two vibrational modes, which have adjacent frequencies and symmetry labels A_{1g} and T_{2g}[104,107]. The splitting of these two modes is more evident in rare earth zirconate and hafnate pyrochlores[104,138,139]. The A_{1g} mode is associated with the modulation of *x*O1 by the vibration of O1 along the [100] axis toward the O3 vacant site[70,105,121,140]. Oueslati and coworkers[129], instead, followed by others[108,141,142], assigned the bands M3 and M5 at ≈300 and 500 cm^{-1} to O-Gd-O bending and Gd-O stretching vibrations respectively, on the basis of the evolution of their wavenumber in the $Gd_2(Ti_{1-x}Zr_x)_2O_7$ solid solution with x_{Zr}. More controversial is the assignment of the remaining T_{2g} modes, which might be attributed to some of the weaker bands that are visible in the spectrum of $Gd_2Ti_2O_7$ at ≈ 113 (M1), 212 (M2), 450 (M4), 550

(M6) and 690 (M7) cm^{-1}. A brief discussion on these additional bands is provided in the following section.

As can be evidenced from Figure 3.8, modes M3 and M5 are clearly affected by line broadening on Zr-substitution. The corresponding values of FWHM as a function of x_{Zr} are plotted in Figure 3.12. In particular, the data for M3 (≈ 311 cm^{-1}) are comparable with those already reported by Hess and coworkers[70].

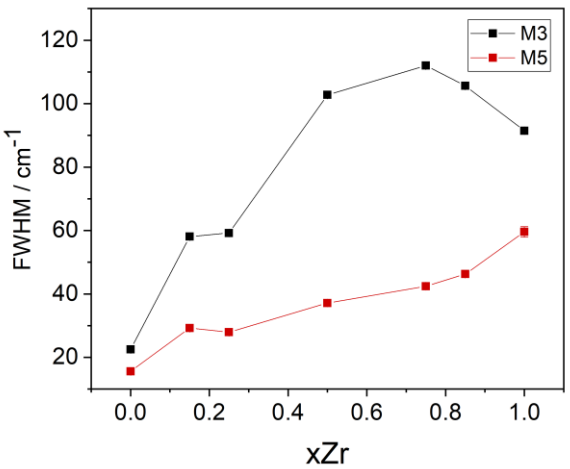

Figure 3.12 FMWH for Raman bands M3 and M6 in the $Gd_2(Ti_{1-x}Zr_x)_2O_7$ series as a function of Zr-content. Lines are guide to the eye.

The lines broadening suggests that static disorder is accumulating within the structure *via* defects formation[129]. The partial loss of translational symmetry at the local scale, caused by static disorder, relaxes the $k = 0$ selection rule and allows phonons from other parts of the Brillouin zone to contribute to the spectra. The phonons mixing, in turn, results in lines broadening in the spectrum[100]. What is

striking is the evolution of the M5 line with respect to the M6 upon Zr-substitution. M6 has been regarded as one of the T_{2g} modes in previous investigations on related pyrochlore systems[48,70,134]. However, it might be associated with extra vibrational modes activated by the chemical substitution at the B site of the structure[143]. The progressive filling of O3 (*8a*) vacant site through the formation of an Anti-Frenkel defect would activate a forbidden mode related to B-O vibration. It is worth remembering at this point that O3 is surrounded by four B-cations in the pyrochlore structure. The newly activated mode M6 moves toward higher wavenumbers on increasing x_{Zr} and reaches ≈600 cm^{-1} for the $Gd_2Zr_2O_7$ compound. The Anti-Frenkel defect leaves the O1 (*48f*) site depleted and this leads to a decrease in intensity of M5[105,144,145] (see for example Figure 3.11). Both modes related to M5 and M6 harden on Zr-substitution because of short O1-O3 distances in Zr-rich composition, being M5 particularly sensitive to O-O interactions[105,145]. Indeed, as revealed by Rietveld analysis, Zr doping in $Gd_2(Ti_{1-x}Zr_x)_2O_7$ brings to progressive O3 site occupation and O1-O3 distances (2.334 Å in $Gd_2Zr_2O_7$) that are much shorter than the O1-O1 (2.664 Å) and O1-O2 ones (2.928 Å).

Another interesting spectral feature is the broad band at ≈700 cm^{-1} (M7), which becomes evident at x_{Zr} =0.50 and is probably a combination of more than just one vibrational mode. This band is commonly assigned to an overtone or second-order scattering process related to the main band at ≈310 cm^{-1}[109,110,146–148]. On the other hand, the intensity of such second-order line is quite surprising in comparison with

the other spectral bands of the first order[82]. DFT calculations have shown that a T_{2g} mode is allowed beyond 700 cm^{-1} in the case of $Gd_2Ti_2O_7$[134]and $La_2Zr_2O_7$ pyrochlores[149]. The high wavenumber suggests that a B-O vibration is involved[150,151]. Glerup and coworkers assigned this M7 band to a BO_7 cluster in line with a gradual disordering from the pyrochlore to the defect fluorite structure in the $Y_2Ti_{2-y}Zr_yO_7$ solid solution and a change of the B-coordination number (CN) from 6 to 7[22]. Sanjuan and *al*. argued that the actual coordination of B species is based on preferential CN of each cation involved[121], causing a disordering of the oxygen atoms in the solid solution based on the following mechanism: an oxygen atom moves from the *48f* site to the vacant *8a*, increasing selectively the CN of Zr to 7. Conversely, the CN of Ti should remain unaffected or even decrease to 5. The presence of Ti atoms in a 5-fold or 6-fold coordination environment and a random displacement of the metal from its ideal position in the coordination polyhedron would activate breathing modes above 700 cm^{-1} (M7)[121]. Moreover, it should be noted that this band is one of the dominant modes associated to B-O stretching in other fluorite-derived superstructures such as weberite[113,140], zirconolite[147,152,153] and brannerite[154–156]. This observation may account for a local ordering in the $Gd_2(Ti_{1-x}Zr_x)_2O_7$ series that is different from the pyrochlore or fluorite structure type.

Besides the fundamental bands of the pyrochlore structure discussed so far, other modes are observed as well. The band at ≈115 cm-1 (M1) in the spectrum of the Ti-endmember has been already reported in previous investigations on $Gd_2Ti_2O_7$ [108,141]

and could be ascribed to a lowering of the local symmetry, which activates formally forbidden IR modes[104]. This evidence suggests that although $Gd_2Ti_2O_7$ approaches the ideal pyrochlore structure more than any composition in this study, some degree of distortion is present as well. The progressive introduction of Zr in the structure enhances the distortion and deviation from the ideal pyrochlore structure and leads to a relaxation of the selection rules. Moving on to the line at ≈215 cm^{-1} (M2), this has been assigned to one of the remaining three T_{2g} modes by several authors[70,107,108,121] and related to the vibration of O2 at the center of OGd4 tetrahedra[108]. The decrease in intensity with Zr-substitution may be ascribed to a change in the position of O2 and/or distortion of the corresponding OGd4 tetrahedron. A similar trend was observed in the case of pressure-induced distortion in $Gd_2Ti_2O_7$[107]. Kumar and coworkers showed by means of DFT calculations that no Raman active modes should be allowed below 220 cm^{-1} and it is likely that the M2 line is another forbidden IR mode activated by displacive disorder of Gd and O2 ions[105,134]. The band at ≈ 258 cm^{-1}, which is hardly visible in the spectrum of $Gd_2Ti_2O_7$ and completely disappears in the other spectra of the solid-solution, has been assigned to a T_{2g} mode by Lummen and coworkers[108]. The other weak feature in the spectrum of $Gd_2Ti_2O_7$ is the band at ≈450 cm^{-1}(M4), which could be assigned again to one of the remaining T_{2g} modes[70,121,146]. Kumar and coworkers predicted this mode with contributions of Gd-O2 stretching and O1-Gd-O2 bending force constants in addition to the dominant O1-Ti-O1 bending force constant from TiO_6 octahedra[134]. The band was already observed in $Gd_2Ti_2O_7$[157] and other lanthanide titanates

$Ln_2Ti_2O_7$ with Ln =Dy, Lu[158] and Tb[109]. Oueslati and colleagues assigned the M4 band to B-O vibration and the red-shift with increasing x_{Zr} was regarded as a clear indication of lighter Ti^{4+} being substituted by heavier Zr^{4+} in the structure[129]. A wavenumber of ≈ 400 cm^{-1} is reached in $Gd_2Zr_2O_7$ for M4 and similar values were recorded for the same composition[159] and other related zirconate pyrochlores like $Nd_{2-y}Y_yZr_2O_7$[160], $Nd_{1-x}Dy_xZr_2O_7$[161] and $Sm_2Zr_2O_7$[162].

High-resolution X-ray diffraction has revealed that $Gd_2(Ti_{1-x}Zr_x)_2O_7$ compounds are affected by increasing structural disorder upon Zr-substitution, despite having the same average structure. Raman spectroscopy has supported this evidence and indicated that the source of disorder needs to be sought at the local scale. This has prompted a deeper investigation of the short-range structure through PDF analysis.

The G(r) of $Gd_2(Ti_{1-x}Zr_x)_2O_7$ solid solutions in the low-r region are shown in Figure 3.13.

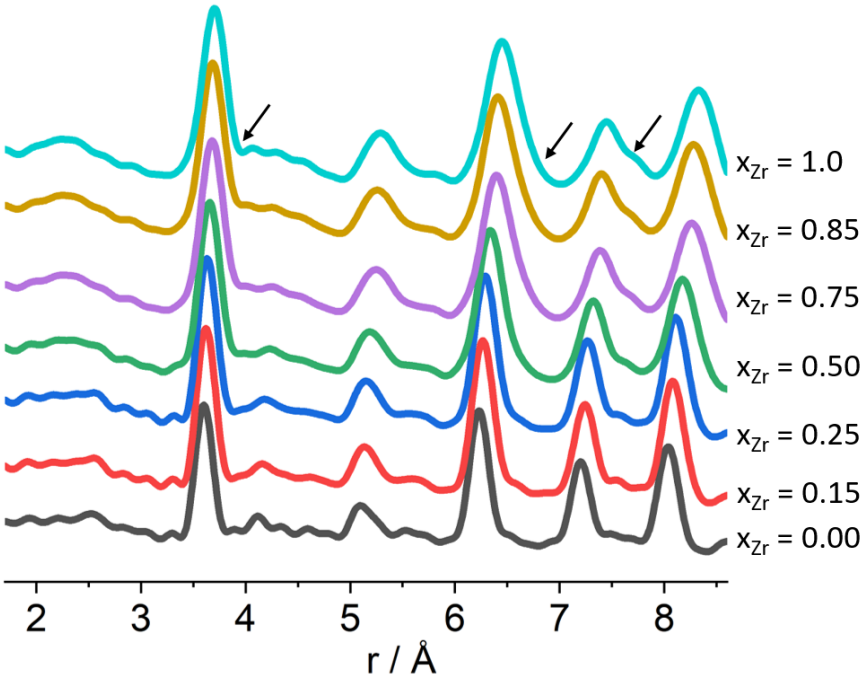

Figure 3.13 G(r) of $Gd_2(Ti_{1-x}Zr_x)_2O_7$ compounds between 1.8 and 9 Å. PDFs were normalized and offset on the Y axis for a better comparison. Black arrows indicate the new M-M correlations arising with Zr-doping.

The change in peak position and FWHM with Zr-doping for the first M-M correlation, as obtained by single peak fitting with a Gaussian function, is shown in Figure 3.14.

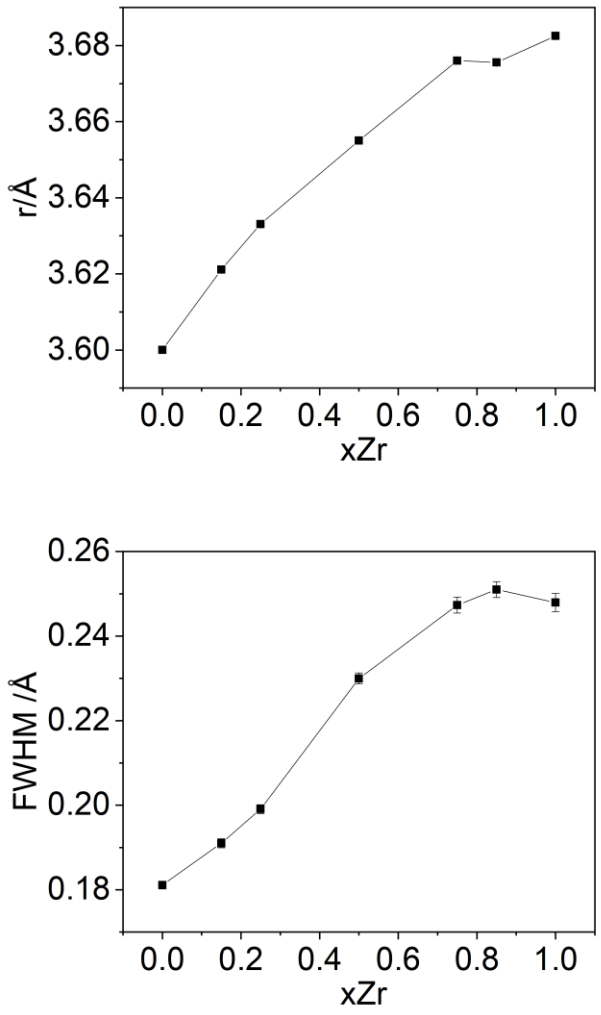

Figure 3.14 Peak r value (top) and FWHM (bottom) for the first M-M correlation in the PDFs of $Gd_2(Ti_{1-x}Zr_x)_2O_7$ compounds

The model-free analysis confirms that Zr-doping induces a progressive shift of the peaks towards high r values (Figure 3.14, top), according to the corresponding increase in cell parameters. Furthermore, a general broadening is observed upon chemical substitution (Figure 3.14, bottom). This can be interpreted as inhomogeneous strain caused by non-uniform distribution of interatomic distances[163]. In analogy with Raman spectroscopy results, PDF analysis suggests that structural disorder arises at the local scale upon Zr-substitution. More subtle is the appearance of new metal-metal correlations, as for example around 3.9, 6.5 and 7.5 Å, although not clearly visible in Figure 3.13 (highlighted by black arrows). The question of whether these correlations are symptoms of structural disorder or the indication of residual sample inhomogeneity can be simply answered by simulating the G(r) of the two phases with the lattice parameters obtained in the Rietveld refinements of HR-XRD patterns (Table 3.1). By doing so, it can be verified that the interatomic distances for the two phases are too close to each other to be distinguished with the resolution of the experimental PDFs.

Structural models were used to analyze the short-range ordering and establish a connection with the average structure. The G(r) functions were initially fitted in the interval 1.8 – 8.0 Å by using the pyrochlore model already employed for describing the average structure in Rietveld refinements. The resulting fits are displayed in Figure 3.15. It can be seen that the residuals increase with x_{Zr} and the major misfits are located between 3.5 and 4.0 Å, at ≈6.5 and 7.5 Å. Clearly, the pyrochlore model fails in fitting the experimental G(r) in the low-r region for Zr-rich compositions of

the $Gd_2(Ti_{1-x}Zr_x)_2O_7$ solid solution. The introduction of a defective pyrochlore model with anion Anti-Frenkel and cation antisite defects, as attempted for the Rietveld refinements of HR-XRD, did not improve the fits. This result can be explained considering that new metal-metal correlations arise in the PDFs upon Zr-substitution, as previously stated. Even though anion Anti-Frenkel and cation antisite defects allow for more degrees of freedom in the structure, they do not provide new positional degrees of freedom required for modelling these additional metal-metal correlations. In fact, the cations remain fixed in their highly symmetrical sites within the pyrochlore structure. It appears that the accumulation of anion Anti-Frenkel defects detected on the long-range scale by HR-XRD is coupled with some sort of structural relaxation at the local scale, which leads in turns to additional interatomic distances visible in the PDF. As indicated also by Raman spectroscopy, a new structural model of lower symmetry is needed to properly describe the local structure of Zr-rich compositions.

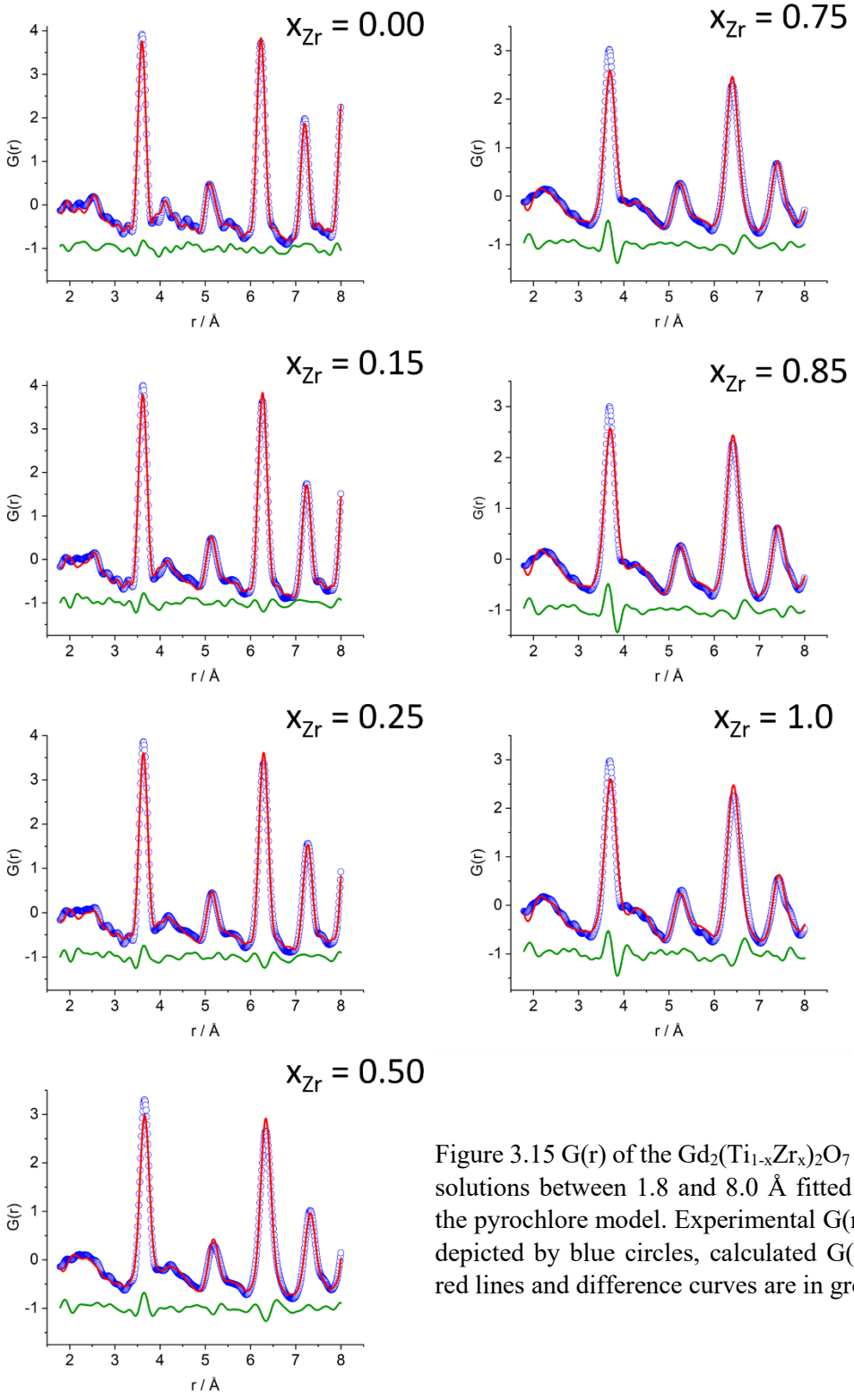

Figure 3.15 G(r) of the $Gd_2(Ti_{1-x}Zr_x)_2O_7$ solid solutions between 1.8 and 8.0 Å fitted with the pyrochlore model. Experimental G(r) are depicted by blue circles, calculated G(r) by red lines and difference curves are in green.

Before discussing the new model employed for the refinement of PDFs in the low-r region, it should be mentioned that the correlation length of these structural distortions was probed. All the experimental G(r) of the $Gd_2(Ti_{1-x}Zr_x)_2O_7$ solid solution were also fitted in the 9-22 Å window with the pyrochlore model. The fit for the Zr-endmember is shown in Figure 3.16 as an example. The difference curve is essentially flat and a low Rw is obtained (≈ 0.05).

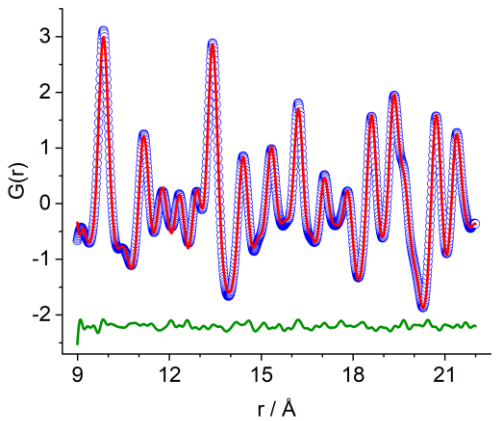

Figure 3.16 G(r) of $Gd_2Zr_2O_7$ fitted with the pyrochlore model between 9 and 22 Å.

This result indicates that the pyrochlore structure is effective in describing the atomic ordering of $Gd_2Zr_2O_7$ in the medium/high r-range. Satisfactory fits in the 9-22 Å window were also obtained for all other compositions and the corresponding Rw values are compared to those for the 1.8-8.0 Å interval in Figure 3.17. The outcome is not unexpected for it was already known that the long-range structure of $Gd_2(Ti_{1-x}Zr_x)_2O_7$ compounds was pyrochlore-like.

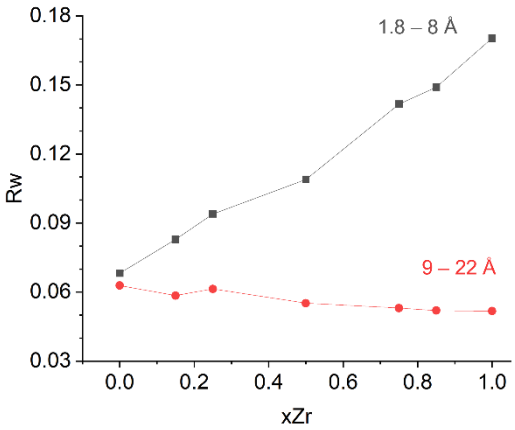

Figure 3.17 Rw values of PDF fits in the 1.8-8 (black) and 9-22 (red) Å windows with the pyrochlore model in $Gd_2(Ti_{1-x}Zr_x)_2O_7$ series as a function of Zr-content.

The interesting result is that the deviation from the pyrochlore structure in the $Gd_2(Ti_{1-x}Zr_x)_2O_7$ series for Zr-rich compositions is confined at a sub-nanometer scale with a correlation length of just few angstroms.

To analyze the PDFs in the low-r region, the weberite-type model was invoked. As stated in the Introduction, the local structure of other fluorite-related oxides was already described with the weberite-type model[30–32]. Shamblin and co-workers used the weberite-type in the orthorombic *Ccmm* space group (n°63, see Part 1) to refine the low-r region of the PDF from neutron total scattering data collected on $Ho_2Zr_2O_7$[30]. Drey and colleagues extended this approach to the $Ho_2(Ti_{1-x}Zr_x)_2O_7$ solid solution using the $C222_1$ setting (space group n°20), in which more oxygen sites and more positional and vibrational degrees of freedom are available with respect to the *Ccmm* space group[31]. The $Ho_2(Ti_{1-x}Zr_x)_2O_7$ solid solution is closely related to the $Gd_2(Ti_{1-x}Zr_x)_2O_7$ series under investigation. Nevertheless, Ho^{3+} is smaller than Gd^{3+} (ionic radius of Ho^{3+}in VIII coordination is 1.015, while that for Gd^{3+} is 1.053) The difference in the ionic radii of the two rare earth cations obviously affects the radii ratio $r_A/r_{(Ti/Zr)}$ and the average structure in the $A_2(Ti_{1-x}Zr_x)_2O_7$ series. In particular, $Gd_2(Ti_{1-x}Zr_x)_2O_7$ compounds are pyrochlore-like throughout all the series and a low concentration of cation antisite defects is detected by Rietveld refinements of HR-XRD patterns. On the other hand, $Ho_2(Ti_{1-x}Zr_x)_2O_7$ materials firstly display pyrochlore ordering for low Zr-concentrations and, then, a defect fluorite structure emerges for $x_{Zr} \geq 0.70$[31,164]. The dissimilar behavior of the two solid solutions at the long-range scale has prompted a modification of the models employed in the description of the local structure for the samples under investigation. The weberite-type structure in $C222_1$ space group adopted by Drey and colleagues in small-box refinements of the PDFs is presented in Table 3.2. The *8c* site at

(0.2360, 0.2374, 0) is seven-fold coordinated and it is shared by both Ho and Zr cations.

Table 3.2 Weberite-type model in *C222₁* space group (n°20) used by Drey and colleagues for $Ho_2Zr_2O_7$ [from Ref. 31]. Fixed coordinates are indicated in fractions or zeros.

Atom	Wyckoff letter	Site symmetry	x	y	z	Occ.
Ho	*4b*	*.2.*	0	0.4956	1/4	1
Zr	*4b*	*.2.*	0	0[a]	1/4	1
Ho/Zr	*8c*	*1*	0.2360	0.2374	0[a]	1
O1	*8c*	*1*	0.139	0.181	0.304	1
O2	*8c*	*1*	0.121	0.770	0.267	1
O3	*4a*	*2..*	0.131	1/2	0	1
O4	*4a*	*2..*	0.131	1/2	1/2	1
O5	*4a*	*2..*	0.072	0	0	1

[a] These coordinates are free parameters.

While one could attempt to apply this model to $Gd_2Zr_2O_7$, the local mixing of cations in the weberite-type structure could not be reconciled with the nearly perfect cation ordering observed at the average scale. Therefore, in the present study the cations were kept separated also in the weberite-type model to retain the pyrochlore ordering. The eight available sites with Wyckoff letter *8c* generated by PDFgui software starting from the site (0.2360, 0.2374, 0) were distributed between Gd and Zr atoms in such a way that the resulting cations distribution would be compatible with that obtained by a 45° rotation of the pyrochlore unit cell around the *a* axis. This operation resulted in a new structural model, and the corresponding space group was identified through the FINDSYM tool[165]. As a consequence of the cations separation, the *C*-centering of the original lattice was lost, leading to a change in the space group

from $C222_1$ to $P222_1$ (n°17). A similar procedure was applied to the weberite-type model in the *Ccmm* space group, resulting in space group *Pcmm*, a non-standard setting of space group *Pmma* (n°51).

Small-box refinements of the PDF of $Gd_2Zr_2O_7$ were conducted in the 1.8-8.0 Å range using both $P222_1$ and *Pmma* models. The refinements were performed in PDFgui preserving the symmetry constraints of the original $C222_1$ and *Ccmm* space groups, while also keeping the cations separated. Eventually, the constrained $P222_1$ model was discarded because it required numerous positional degrees of freedom particularly for the oxygen atoms and, when refined, could yield non-physical oxygen-oxygen distances. However, it should be underlined that the final choice of the structural model for PDF analysis was mainly based on the ability of fitting the metal-metal correlations with the minimum amount of refined parameters within the specific short r-interval. Comparing the models in space groups $C222_1$ and *Ccmm* (see Tables 3.2 and 1.3), it is obvious that the former setting contains more positional degrees of freedom for both cations and anions. Later in this section, it will be shown that only one of the cations coordinates have a significant effect. In addition, as described in Part 2, the PDF of pyrochlore oxides from X-ray scattering data is inherently more sensitive to M-M correlations than M-O or O-O interatomic distances. Also, the peaks in the experimental G(r) functions involving anions are significantly broader than those in the simulated PDFs (see for example Figures 3.13 and 2.9), indicating severe structural disorder of the oxygen atoms. These aspects

limit the possibility of using the PDF for probing distortions in the anions array. Taking into account all the available positional degrees of freedom of both $C222_1$ and *Ccmm* models and considering also three cell parameters, a scale factor, a short range correlated motion parameter (delta2 in PDFGui) and four isothermal displacement parameters (one for each of the three cationic sites and one for oxygen atoms), there are 23 parameters for the $C222_1$ setting and 18 for *Ccmm.* The number of independent data points in the experimental PDFs can be calculated as follows[166]:

$$N = \frac{(r_{max} - r_{min})Q_{max}}{\pi}$$

where r_{max} is 8.0 Å, r_{min} is 1.8 Å and Q_{max} is 27 $Å^{-1}$. N is about 53 and a parameter-to-data ratio of ~2 is obtained for the $C222_1$ model, while ~3 for the *Ccmm* model. Consequently, the structural model in *Ccmm* space group with cations separated at the *8g* site (final space group *Pmma*) was selected for fitting the PDFs in the low-r region.

An improvement in fit quality is obtained for the refinements with the constrained *Pmma* weberite-type model (Rw = 0.091) compared to the pyrochlore model (Rw = 0.17). The refined weberite-type model in space group *Pmma* for $Gd_2Zr_2O_7$ is shown in Table 3.3 and the fitted G(r) between 1.8 and 8.0 Å is plotted in Figure 3.18. 7-fold coordinated cations are Gd3 and Zr1 at the *4k* sites.

Table 3.3 Refined weberite-type model in *Pmma* space group (n°51) for the G(r) $Gd_2Zr_2O_7$. Fixed coordinates are indicated in fractions or zeros.

Atom	Wyckoff letter	Site symmetry	x	y	z	Occ.
Gd1	*2b*	*.2/m.*	0	1/2	0	1
Gd2	*2c*	*.2/m.*	0	0	1/2	1
Gd3	*4k*	*m..*	1/4	0.23846	0.75 [a]	1
Zr1	*4k*	*m..*	1/4	0.73846	0.25 [a]	1
Zr2	*2a*	*.2/m.*	0	0	0	1
Zr3	*2d*	*.2/m.*	0	1/2	1/2	1
O1	*8l*	*1*	1/2	0.21921	0.87884	1
O2	*8l*	*1*	1/2	0.71921	0.37884	1
O3	*2e*	*mm2*	1/4	0	0.04846	1
O4	*2f*	*mm2*	1/4	1/2	0.54846	1
O5	*2f*	*mm2*	1/4	1/2	0.08635	1
O6	*2e*	*mm2*	1/4	0	0.58635	1
O7	*2f*	*mm2*	1/4	1/2	0.83476	1
O8	*2e*	*mm2*	1/4	0	0.33476	1

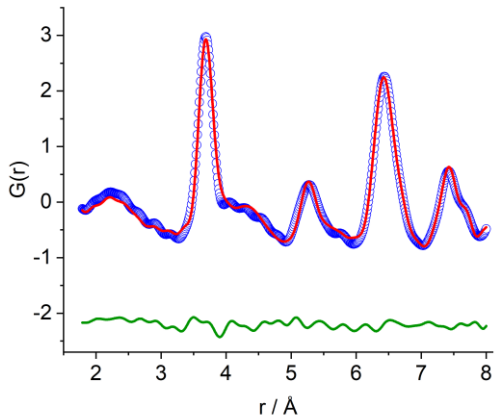

Figure 3.18 G(r) of $Gd_2Zr_2O_7$ fitted with the weberite-type model (space group *Pmma*) between 1.8 and 8.0 Å.

From the data presented in Table 3.3, it is evident that Gd and Zr cations at the *4k* sites are considerably shifted along the b-axis compared to the special position in a pyrochlore-like cell (0.23846 instead of 0.25 for Gd3 and 0.73846 instead of 0.75 for Zr1). The z-coordinates did not exhibit an appreciable change and were kept fixed at the values 0.75 and 0.25 respectively. The shifts of cations along the b-axis of the weberite-type cell results in a 1D-modulation of metal-metal distances. This implies that metal-metal correlations can span a certain range of values in the different cation shells of the weberite-type structure. In contrast, the pyrochlore (or fluorite) structure features special positions of cations with fixed coordinates, setting the value of metal-to-metal correlations to a specific value. The positional degrees of freedom provided by the weberite-type structure allow to account for the peak broadening and/or splitting in the G(*r*) of $Gd_2Zr_2O_7$ and to resolve misfits at ≈3.9 Å, ≈6.5 Å and ≈7.5 Å (see Figures 3.15 and 3.18). An attempt was made to extend the refinement 'box' to at least the length of the longer axis in the weberite-type structure (≈10-12 Å). A poor fit is obtained if none of the parameters is allowed to vary (Rw = 0.213). Relaxing the structure improves the fit quality (Rw =0.12), but it also leads to the reappearance of the misfits already observed for the pyrochlore model (Figure 3.15). This result confirms that the distortions and deviations from the average structure in $Gd_2Zr_2O_7$ are limited to a sub-nanometer scale. The weberite-type model employed in the case of $Gd_2Zr_2O_7$ was also applied for the solid solution $Gd_2(Ti_{1-x}Zr_x)_2O_7$. Starting with the Zr-endmember, Ti was initially introduced into the 6-fold coordinated sites (*2a* in Table 3.3), while Zr was distributed over both the 6-fold and

7-fold coordinated sites (*4k* in Table 3.3). In the $Gd_2(Ti_{0.5}Zr_{0.5})_2O_7$ composition, Ti and Zr cations were entirely separated into the 6-fold and 7-fold coordinated sites respectively, while for $x_{Zr} < 0.50$, Ti entered also the 7-fold coordinate site. The variation of Rw in the fit of PDFs across the $Gd_2(Ti_{1-x}Zr_x)_2O_7$ series is plotted in Figure 3.19. The outcome is that the weberite-type model works quite well when Ti is confined at the 6-fold coordinated site and the best fit is obtained precisely for $Gd_2(Ti_{0.5}Zr_{0.5})_2O_7$, (Rw = 0.073) when Ti and Zr form TiO_6 and ZrO_7 polyhedra.

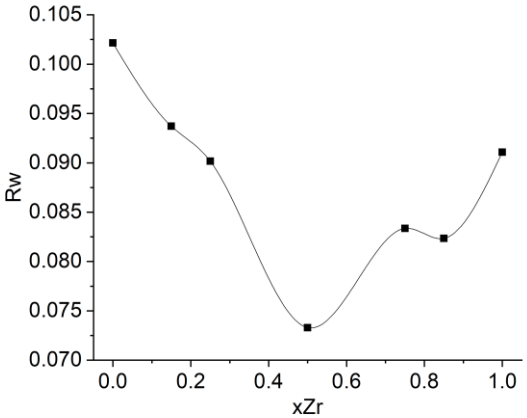

Figure 3.19 Rw values of PDF fits in the 1.8-8.0 Å windows with the weberite-type model in $Gd_2(Ti_{1-x}Zr_x)_2O_7$ series as a function of Zr-content.

Instead, an increase in Rw values is found for $x_{Zr} < 0.50$, for which the Ti^{4+} ions are forced into 7-fold polyhedra. These results are in accordance with those obtained by Drey and colleagues on $Ho_2(Ti_{1-x}Zr_x)_2O_7$ solid solution[31]. In their analysis of the

short-range structure by small-box refinements of PDFs from both neutron and X-ray data, a two-phase approach was adopted. Ti atoms were maintained into a $Ho_2Ti_2O_7$ pyrochlore phase, whereas Zr atoms were confined into a $Ho_2Zr_2O_7$ weberite-type phase ($C222_1$ space group). Going from the Ti-endmember to the Zr-endmember of the series, the phase fraction of the weberite-type structure varied from zero to one. For the $Ho_2(Ti_{0.5}Zr_{0.5})_2O_7$ composition, the PDF from X-ray data was refined in the range 3.2-12.5 Å to a Rw value of 0.057, with a weberite-type phase fraction of 0.46. According to Drey and coworkers, a weberite-type model provides a way to reconcile the varying degrees of structural disorder observed at both the long-range and short-range scale in the $Ho_2(Ti_{1-x}Zr_x)_2O_7$ system. It was already mentioned in the Introduction that compositions in the $Ho_2(Ti_{1-x}Zr_x)_2O_7$ solid solution undergo a phase transition from the pyrochlore to defect fluorite structure when $x_{Zr} \approx 0.625$. However, accumulation of anion Anti-Frenkel defects is detected upon Zr-substitution in the pyrochlore part of the phase diagram. The random movement of oxygen O1 into the vacant O3 site creates a specific cations coordination environment at the short-range scale, where the typical AO_8 and BO_6 polyhedra of the pyrochlore structure are accompanied by new AO_7 and BO_7 polyhedra. This configuration is characteristic of weberite-type compounds with formula A_3BO_7 (see the structure description Part 1). In the $Ho_2(Ti_{1-x}Zr_x)_2O_7$ system, it is assumed that, due to differences in size, Zr at the B site is more likely to become 7-fold coordinated rather than Ti. This assumption is supported by the evidence that seven oxygen atoms coordinate Zr^{4+} in monoclinic zirconia[167], and an increase in

coordination number of Zr has been reported in related pyrochlore systems[72,74]. Using an approach based on Pauling's rules, O'Quinn et al. shed light on the disordering process that occurs in $Ho_2(Ti_{1-x}Zr_x)_2O_7$ on Zr-substitution[24]. The formation of an anion Anti-Frenkel defect, leading to 7-fold cations coordination polyhedra, restricts the movement of nearby oxygen atoms. As a result, weberite-type nanodomains maintain a certain distance from other weberite-type clusters until a critical density is reached, triggering a long-range phase transition to the defect fluorite structure. Moreover, the presence of disordered weberite-type nanodomains in $Ho_2(Ti_{1-x}Zr_x)_2O_7$ samples is responsible for the diffuse scattering in neutron and X-ray diffraction patterns[24,31]. The increasing structural disorder detected in $Gd_2(Ti_{1-x}Zr_x)_2O_7$ with increasing Zr-content might be explained with a similar picture. However, it is essential to consider two crucial points. First, despite the rising concentration of anion Anti-Frenkel defects, the pyrochlore structure is retained at the long-range scale for all samples in the $Gd_2(Ti_{1-x}Zr_x)_2O_7$ solid solution. Second, the coherence length for the structural distortions mapped through a weberite-type model in $Gd_2(Ti_{1-x}Zr_x)_2O_7$ appears to be shorter (approximately 8Å) compared to the $Ho_2(Ti_{1-x}Zr_x)_2O_7$ system (≈12Å)[31]. It is interesting to underline that in the present work the application of the weberite-type model to the refinements of the PDFs in the low-r region gives the best result for $x_{Zr} = 0.50$. An increase in Rw values is observed for Zr-rich compositions (see Fig. 3.19). An analogous trend has been also observed by Drey and coworkers for their refinements of X--ray PDFs in the $Ho_2(Ti_{1-x}Zr_x)_2O_7$ system with the two-phase method[31]. These findings point to the

fact that the scheme of structural disorder might be more complex than that described by a weberite-type model. As a result, models with multiple phases (usually two) have been applied in small-box refinements of PDFs. These models combine pyrochlore, defect fluorite and weberite-type structures to describe the local coordination environments of cations[31,195,196].

An alternative description might be provided by big-box modelling of PDF data. For instance, Marlton and co-workers have analyzed neutron total scattering data collected on the $Y_2(Sn_{1-x}Zr_x)_2O_7$ series using a Reverse Monte Carlo (RMC) method[168]. They have shown that upon Zr-substitution, anion Anti-Frenkel pairs form and 7-fold coordination polyhedra are generated at the A- and B-sites. The new polyhedral configuration is accompanied by distortions of bond angles and bond distances in both the cation and anion substructures. Marlton and co-workers argued that the good fits of the X-ray and neutron PDFs with the weberite-type model obtained for the $Ho_2(Ti_{1-x}Zr_x)_2O_7$ series by Drey[31] and Shamblin[30] were essentially due to data collected at room temperature. The thermal broadening of the peaks would have hidden subtle structural features, which could not be properly modelled with the weberite-type.

Another approach for developing a structural model of the local disorder in $Gd_2(Ti_{1-x}Zr_x)_2O_7$ oxides was envisaged through atomistic and DFT calculations in collaboration with Dr. Davide Ceresoli of Italian CNR (Consiglio Nazionale delle Ricerche). Here the central findings are highlighted. Atomistic simulations were used

to rapidly generate several configurations of the pyrochlore structure of $Gd_2Zr_2O_7$ (cubic cell of 88 atoms) with variable amounts of anion Anti-Frenkel defects. Subsequently, the lowest in energy of these configurations were selected and the corresponding atomic positions were relaxed at the DFT level. The resulting structures were used as models in small-box refinements of the G(r) of $Gd_2Zr_2O_7$ in the 1.8-8.0 Å interval. During the refinements, only the lattice constant, the scale factor, the correlated motion parameter, and three isotropic displacement parameters (one for Gd, Zr and O ions) were varied, while the atomic positions were kept fixed at the optimized value. Low fit residuals (Rw = 0.096) were obtained when a combination of two simulated structures was implemented in a two-phase refinement. The G(r) of samples with $0 < x_{Zr} < 1$ were treated also with a biphasic model. However, Ti was introduced only into a pyrochlore phase with composition $Gd_2Ti_2O_7$, while Zr was distributed over the pyrochlore phase and one of the simulated structures with Anti-Frenkel defects. The primary result is that the calculated G(r) from the simulated structures can effectively fit the experimental G(r) of $Gd_2Zr_2O_7$, reproducing those features that were not adequately mapped by the pyrochlore model. The simulated structures are characterized by Anti-Frenkel defects, which are clustered around Zr atoms. As mentioned, the atomic positions are relaxed in response to defects formation and, therefore, the cations are shifted from their highly symmetric sites of the pyrochlore structure. Furthermore, some oxygens are found in 'bridging' positions between two Zr-ions and those occupying

the vacant O3 site tend to move towards the edge or face of a B_4 tetrahedron. This work has been the subject of a recent publication[169].

To summarize, the structural distortions detected at the local scale in Zr-rich pyrochlores of $Gd_2(Ti_{1-x}Zr_x)_2O_7$ solid solution can be suitably described by a weberite-type model. Zr^{4+} ions can expand their coordination sphere and additional degrees of freedom results in new M-M correlations with respect to the pyrochlore structure. However, the short coherence length (smaller than its longest cell axis) and the mixing of cations assumed by the original weberite-type model, but negligible in these samples, suggest that alternative descriptions are possible. In particular, structural distortions caused by anion Anti-Frenkel defects need to be considered. Big-box modelling and theoretical calculations might represent important tools for developing new structural models.

Part 4

$(Nd_{1-x}Gd_x)_2Zr_2O_7$ solid solution

The following samples were synthesized by solid-state reaction starting from Nd_2O_3, Gd_2O_3 and ZrO_2 as precursors.

Compound	Annealing cycles (#)
$Nd_2Zr_2O_7$	4
$(Nd_{0.917}Gd_{0.083})_2Zr_2O_7$	4
$(Nd_{0.833}Gd_{0.167})_2Zr_2O_7$	4
$(Nd_{0.750}Gd_{0.250})_2Zr_2O_7$	4
$(Nd_{0.625}Gd_{0.375})_2Zr_2O_7$	4
$(Nd_{0.500}Gd_{0.500})_2Zr_2O_7$	4
$(Nd_{0.375}Gd_{0.625})_2Zr_2O_7$	4
$(Nd_{0.250}Gd_{0.750})_2Zr_2O_7$	4
$(Nd_{0.167}Gd_{0.833})_2Zr_2O_7$	5
$(Nd_{0.083}Gd_{0.917})_2Zr_2O_7$	5

As will be clarified, $(Nd_{1-x}Gd_x)_2Zr_2O_7$ and $Gd_2(Ti_{1-x}Zr_x)_2O_7$ solid solutions share a lot of similarities regarding the investigation of both the average and short-range structure. Firstly, at the average scale, all compounds of the $(Nd_{1-x}Gd_x)_2Zr_2O_7$ series adopt the pyrochlore structure, as can be deduced from the presence of superstructure peaks in HR-XRD patterns (see for example 111_P, 311_P and 331_P reflections in Figure 4.1). In contrast with $Gd_2(Ti_{1-x}Zr_x)_2O_7$ system, the chemical substitution of Gd^{3+} in place of Nd^{3+} at the A site of the structure (*16d*) does not result in a visible reduction of the intensity of superstructure peaks, because of comparable X-ray scattering power of Gd^{3+} and Nd^{3+}.

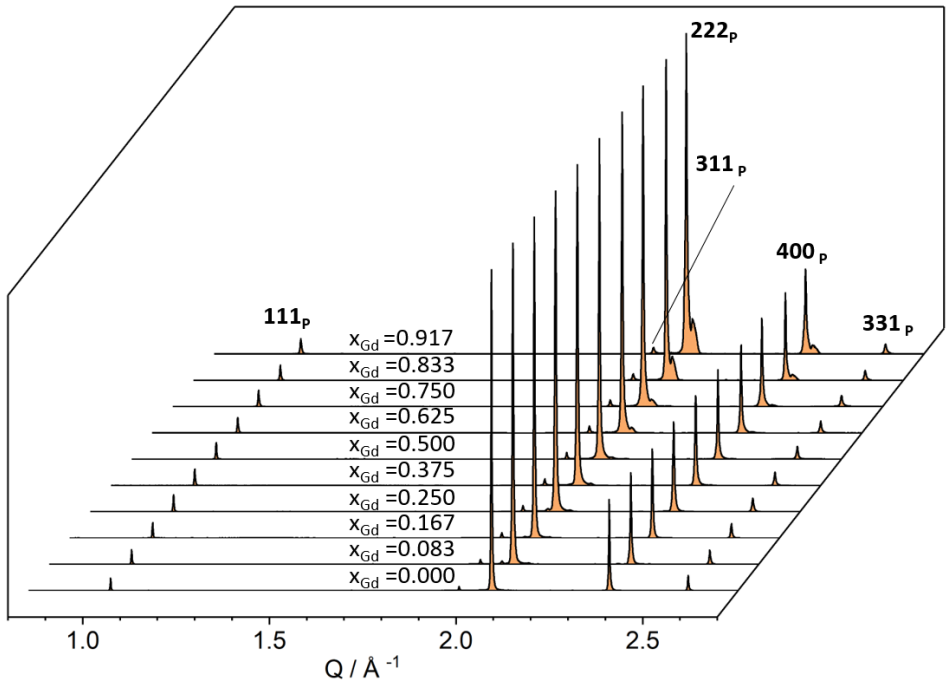

Figure 4.1 Evolution of HR-XRD patterns of $(Nd_{1-x}Gd_x)_2Zr_2O_7$ series with xGd in the Q range 0.7 - 2.7 $Å^{-1}$. Patterns were normalized and offset in a 3D graph for a better comparison. Superstructure peaks 111_P, 311_P and 331_P are visible in the pattern of each composition.

The evolution of the average structure upon chemical substitution was followed by Rietveld refinements of HR-XRD patterns. As in the case of $Gd_2(Ti_{1-x}Zr_x)_2O_7$ solid solution, a disordered pyrochlore model was employed (see also Part 3). The structural parameters that were allowed to vary were the lattice constant, *x*O1, U_{iso} of A- , B- and oxygen-sites, occupancy of the O3 site and occupancy of Zr at the A-site. In particular, the occupancy of O3 site was constrained to that of O1, forming

an anion Anti-Frenkel pair, while the occupancy of O2 site was fixed to unity. This is in line with the findings of neutron diffraction studies on $Nd_2Zr_2O_7$[170] and $Nd_2Hf_2O_7$[171], where Anion Frenkel defects were detected between O1 and O3 sites, whereas O2 site was found fully occupied. The problem of determining the distribution of three cation species over two crystallographic sites was solved by assuming that, except for $x_{Gd} = 0.000$, only the Gd^{3+} would replace the Zr^{4+} at the B site and vice versa[47] (see also Part 3 for details). As in the case of $Gd_2(Ti_{1-x}Zr_x)_2O_7$ solid solution, a residual phase inhomogeneity derived from the solid-state synthesis was detected in the form of peak asymmetry (Figure 4.2). This feature was modeled using a second pyrochlore phase with a different lattice constant and larger profile terms to account for the broader peak shape. All the other structural parameters were constrained to those of the primary pyrochlore phase. With increasing Gd-content, an additional phase become visible and broad reflections can be identified in the HR-XRD patterns near the structure (fluorite) peaks at higher Q values (see for example reflections 222_P and 400_P in Figure 4.1 and reflection 440_P in Figure 4.3). The peaks of this additional phase were quite separated and could be clearly distinguished from the structure peaks of the main phase. Since no residual intensity was detected near the superstructure peaks instead, it was excluded that the additional phase had a pyrochlore structure. In particular, for compositions with $x_{Gd} = 0.625$, 0.750, 0.833 and 0.917, this residual intensity was treated in the refinements as a defect fluorite phase with the same composition of the main pyrochlore phase. Again, the structural parameters were constrained to those of the primary phase and only a lattice constant

and profile terms were allowed to vary. A similar was reported in the literature for $(Gd_{1-x}Tb_x)_2Zr_2O_7$[77] and $(Ho_{1-x}Nd_x)_2Zr_2O_7$ [172] solid solutions prepared by conventional solid state synthesis and characterized by means of synchrotron and/or neutron diffraction.

Examples of Rietveld refinements are plotted in Figure 4.4,

The results of Rietveld analysis performed on HR-XRD patterns of $(Nd_{1-x}Gd_x)_2Zr_2O_7$ samples are summarized in Table 4.1 and displayed in Figure 4.5. Lattice parameter is given as weighted average of lattice parameters of phase 1, phase 2 and phase 3 (considering doubling of the unit cell for phase 3, see Table 4.1)

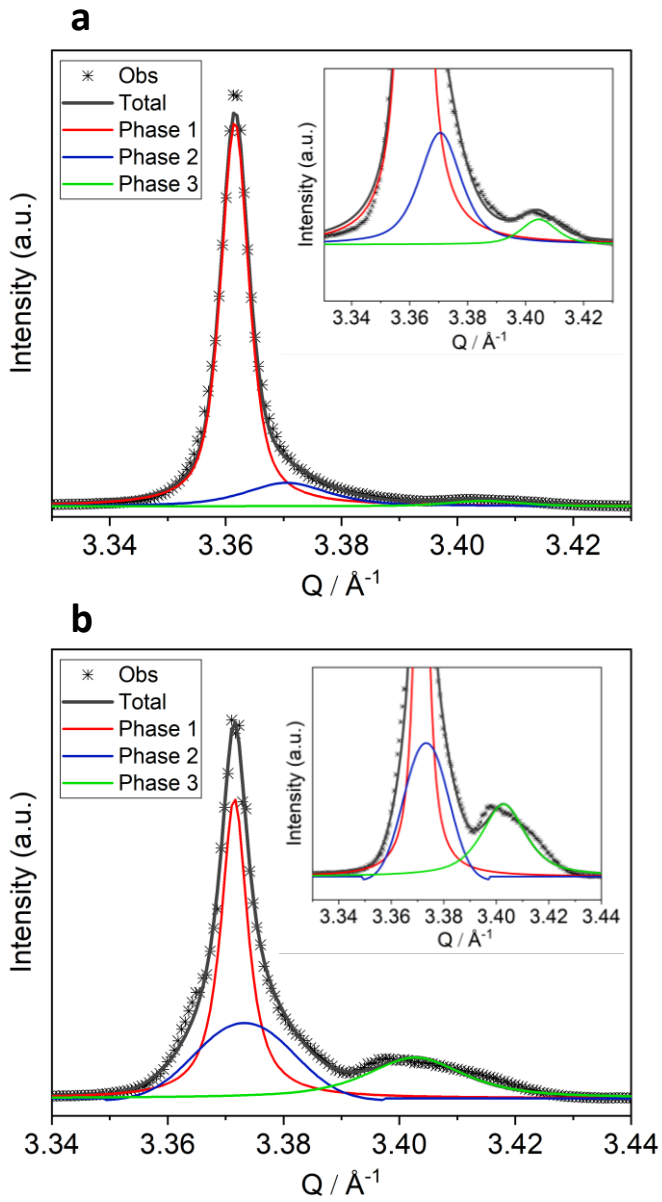

Figure 4.3 Detail of 440_P reflection in HR-XRD patterns of compositions with xGd = (**a**) 0.625 and (**b**) 0.917. Symbols represent the observed pattern, while solid lines are the calculated profile by Rietveld refinement. The green line is associated to the defect fluorite phase detected in the patterns (220_F reflection)

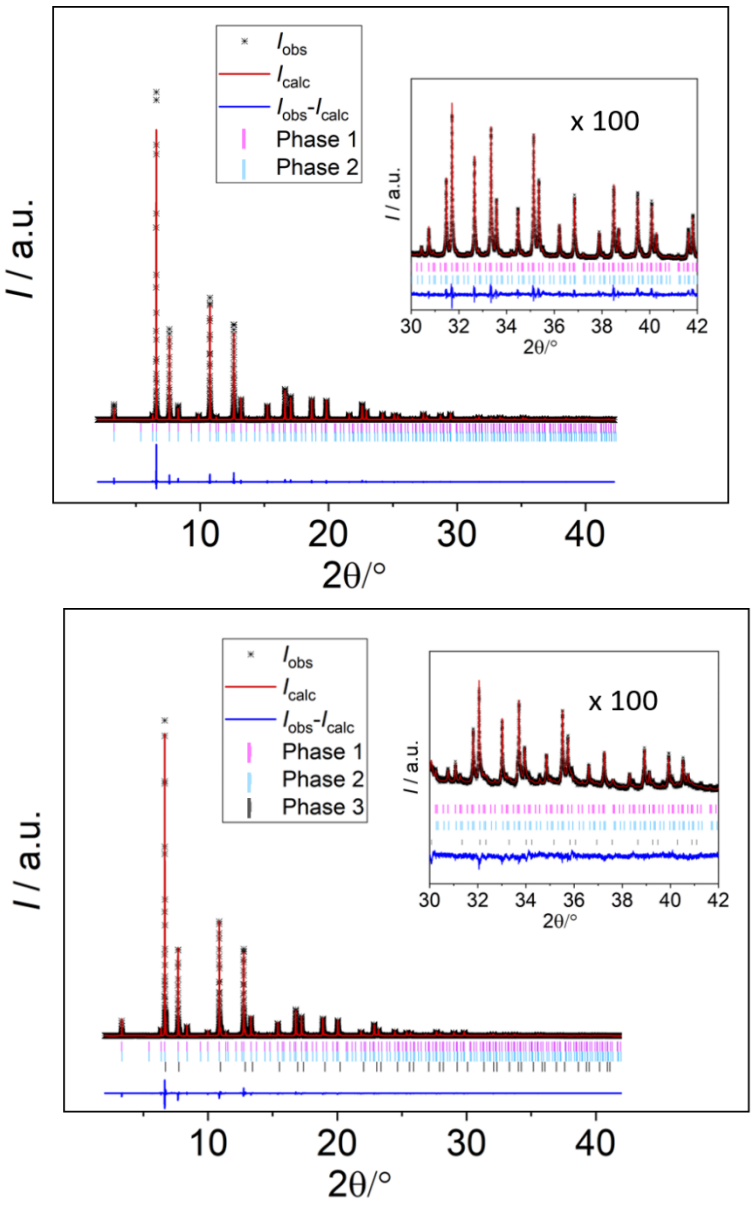

Figure 4.4 Rietveld refinements of synchrotron HR-XRD profiles of (top) $(Nd_{0.833}Gd_{0.167})_2Zr_2O_7$ and (bottom) $(Nd_{0.167}Gd_{0.833})_2Zr_2O_7$ samples

Table 4.1 Structural parameter derived from Rietveld refinements of HR-XRD patterns of $(Nd_{1-x}Gd_x)_2Zr_2O_7$ solid solution. Estimated standard deviation values are in parentheses. Those of weight fractions are not indicated because underestimated by the software.

xGd		**0.000**	**0.083**	**0.167**	**0.250**	**0.375**	**0.500**	**0.625**	**0.750**	**0.833**	**0.917**
Phase 1 s.g. $Fd\bar{3}m$	Weight Fraction %	74.5	70.3	78.7	89.3	87.7	95.3	83.1	75.8	67.9	50.8
	a / Å	10.67053(1)	10.66309(2)	10.64838(2)	10.6396(2)	10.6228(4)	10.60503(3)	10.57277(3)	10.57199(3)	10.53713(3)	10.54151(4)
Phase 2 s.g. $Fd\bar{3}m$	Weight Fraction %	25.5	29.7	21.3	10.7	12.3	4.7	14.4	19.5	14.7	27.1
	a / Å	10.66309(9)	10.65306(9)	10.6385(2)	10.6205(2)	10.6020(4)	10.537(2)	10.5451(6)	10.5538(3)	10.5208(2)	10.5359(1)
Phase 3 s.g. $Fm\bar{3}m$	Weight Fraction %	-	-	-	-	-	-	2.5	4.7	17.4	22.1
	a / Å	-	-	-	-	-	-	5.2196(1)	5.2219(2)	5.22303(6)	5.22235(7)
*x*O1		0.3353(2)	0.3367(2)	0.3373(2)	0.3380(2)	0.3390(3)	0.3392(3)	0.3416(3)	0.3412(2)	0.3456(3)	0.3472(4)
o.f.(O3)		0.092(9)	0.15(1)	0.23(1)	0.23(1)	0.25(1)	0.28(1)	0.39(1)	0.38(1)	0.46(1)	0.50 (1)
o.f.(Zr_A)		0.013(2)	0.014(2)	0.013(2)	0.016(2)	0.016(2)	0.014(2)	0.025(2)	0.020(1)	0.041(1)	0.061(2)
Uiso / $Å^2$	A	0.00473(5)	0.00566(7)	0.00630(6)	0.00703(7)	0.00749(8)	0.00988(9)	0.00861(6)	0.01129(7)	0.01018(7)	0.01152(9)
	B	0.00423(7)	0.0067(1)	0.0082(1)	0.0093(1)	0.018(1)	0.0133(2)	0.0139(1)	0.0152(1)	0.0152(1)	0.0172(2)
	O	0.0056(4)	0.0071(6)	0.011(7)	0.0097(7)	0.0103(8)	0.0126(8)	0.0113 (7)	0.0106(6)	0.0223(7)	0.0272(8)
wRp(%)		9.3	10.1	9.5	9.3	10.8	9.1	8.2	6.6	8.2	8.8

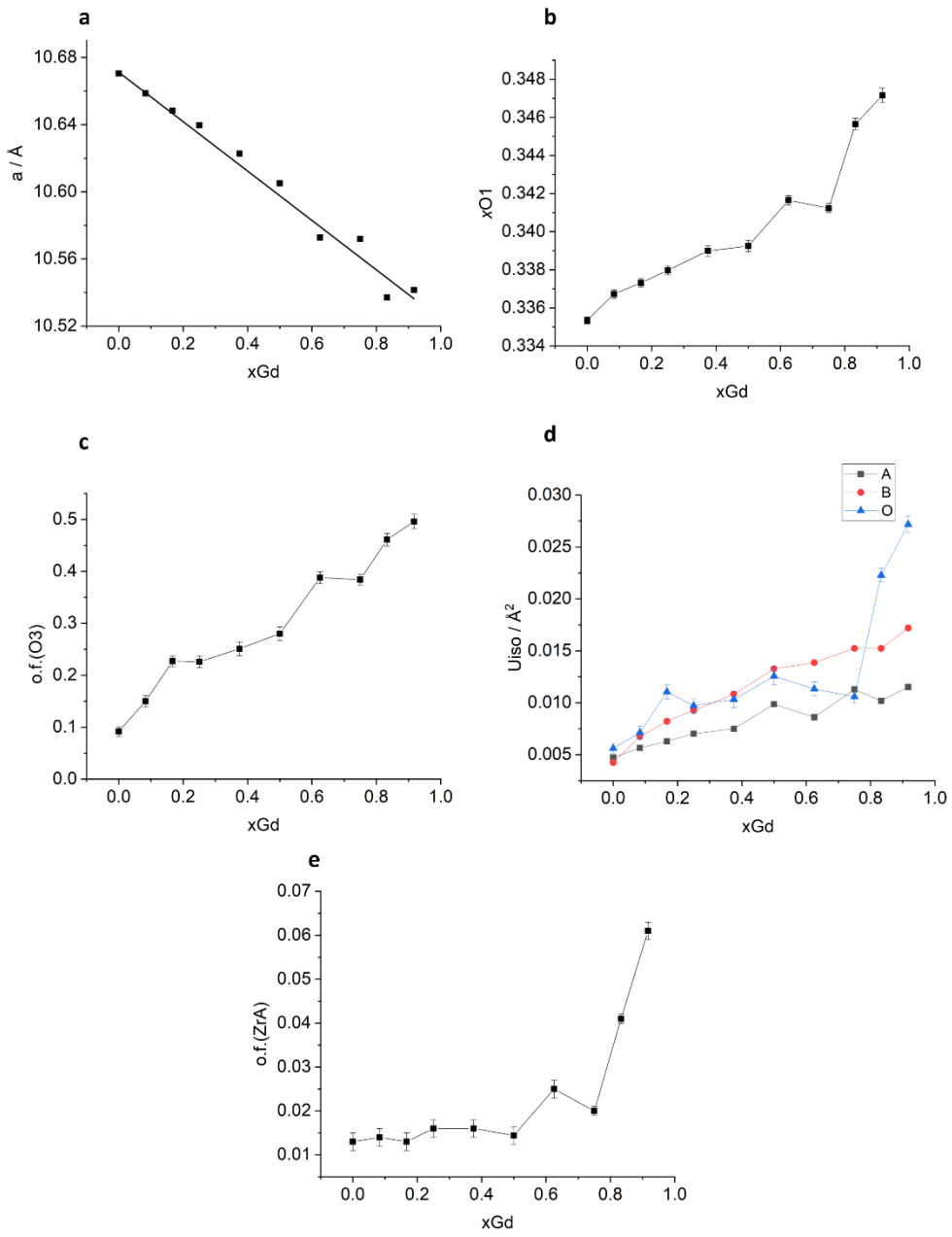

Figure 4.5 (**a**) lattice parameter, (**b**) x-coordinate of O1, (**c**) occupancy factor of O3 site, (**d**) U_{iso}·and (**e**) occupancy factor of Zr at the A site as a function of Gd-content in the $(Nd_{1-x}Gd_x)_2Zr_2O_7$ solid solution. Solid line in plot (a) is a linear fit.

The substitution of Nd^{3+} with Gd^{3+} at the A site of the structure (*16d*) induces a linear reduction of the lattice parameter (Figure 4.5a) and a consequent shift of diffraction peaks to higher Q values. This trend aligns with previous reports on $(Nd_{1-x}Gd_x)_2Zr_2O_7$ solid solution[48,173] or other zirconate systems where A-site substitution with cations of different sizes occurs[49,77,174]. In fact, the ionic radius of Nd^{3+} in 8-fold coordination is 1.109 Å, while that of Gd^{3+} is 1.053 Å. A reversed situation was observed in the previous section on $Gd_2(Ti_{1-x}Zr_x)_2O_7$ solid solution when substituting the smaller Ti^{4+} with the bigger Zr^{4+} at the B-site. However, the chemical substitution associated with the reduction of r_A/r_B ratio in both $Gd_2(Ti_{1-x}Zr_x)_2O_7$ and $(Nd_{1-x}Gd_x)_2Zr_2O_7$ solid solution leads to an increase of *x*O1 (Figure 4.5b), o.f.(O3) (Fig. 6.4c), U_{iso} (Fig. 4.5d) and o.f.(Zr_A) (4.5e) (see previous chapter for data on $Gd_2(Ti_{1-x}Zr_x)_2O_7$ series). The coordinate *x*O1 steadily increases with Gd-substitution up to x_{Gd}=0.75, then it is boosted in the Gd-rich part of the phase diagram (x_{Gd} = 0.833, 0.917) (Figure 4.5b), while a more linear trend was observed for $Gd_2(Ti_{1-x}Zr_x)_2O_7$ compositions. A sudden change of slope is also experienced by U_{iso}_O (Fig. 4.5d) and o.f.(Zr_A) (Fig. 4.5e). The change of slope in the plot of *x*O1 vs. x_{Gd} was related to a discontinuous transition from 'ordered pyrochlore' to 'defect pyrochlore' in the $(Nd_{1-x}Gd_x)_2Zr_2O_7$ system by Mandal and coworkers[48]. They identified this transition at $x_{Gd} \geq 0.90$, while, in the present study, it appears that such transition can be detected for $x_{Gd} > 0.75$. It is worth remembering that, in general, the *x*O1 parameter acts as a marker of disorder in pyrochlore oxides[46]. As was already discussed, the steps of the disordering process at the long-

range scale are the randomization of anions and vacancies through the formation of anion Anti-Frenkel defects and the randomization cations over their crystallographic sites by cation antisite defects. It appears that in analogy with the $Gd_2(Ti_{1-x}Zr_x)_2O_7$ series, there is a gradual accumulation of anion Anti-Frenkel defects between O1 and O3 sites, while the concentration of cation antisite defects remains low throughout the whole $(Nd_{1-x}Gd_x)_2Zr_2O_7$ series. Indeed, o.f.(O3) progressively increases from 0.092 in $Nd_2Zr_2O_7$ to 0.496 in $(Nd_{0.083}Gd_{0.917})_2Zr_2O_7$ (Figure 4.5c), while o.f.(Zr_A) ranges from 0.01 and 0.02 up to $x_{Gd} = 0.750$, before reaching 0.06 for $x_{Gd} = 0.917$ (Fig. 4.5e). Disorder in the anion substructure with a reduction of r_A/r_B has been already documented in related systems such as $(Gd_{1-x}Tb_x)_2Zr_2O_7$[77], $(La_{1-x}Y_x)_2Zr_2O_7$, $(La_{1-x}Y_x)_2Hf_2O_7$[175] and $(Nd_{1-x}Ho_x)_2Zr_2O_7$[172]. Although the refined occupancies might be different in those cases, there is a clear relationship with the increase of *x*O1, indicating an increase in structural disorder[172]. The rise in U_{iso} parameters is also a clear indication of static disorder growing within the structure on increasing x_{Gd} (Figure 4.5d). A similar trend was observed in Part 3 for the $Gd_2(Ti_{1-x}Zr_x)_2O_7$ solid solution as well. Residual static disorder that cannot be fully described by the defective pyrochlore model affects the atomic displacement parameters.

The structural disorder within the solid solution was further investigated by means of Raman spectroscopy. Figure 4.6 displays the Raman spectra of the $(Nd_{1-x}Gd_x)_2Zr_2O_7$ samples. The relevant bands that change upon chemical substitution are labeled from B1 to B5. Changes in frequency values are shown in Figure 4.7, and selected fits of vibrational bands with Gaussian functions are reported in Figure 4.8.

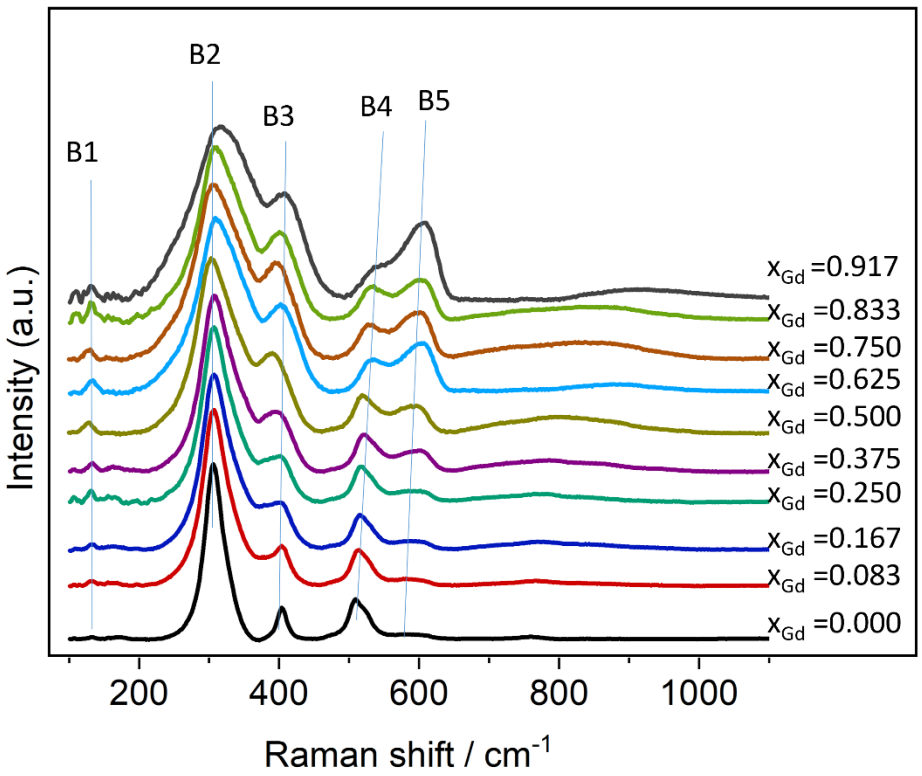

Figure 4.6 Raman spectra of $(Nd_{1-x}Gd_x)_2Zr_2O_7$ solid solution between 100 and 1100 cm^{-1} offset on the Y axis. After background subtraction, each spectrum was normalized between 0 and 100. The observed vibrational bands are labelled from B1 to B5.

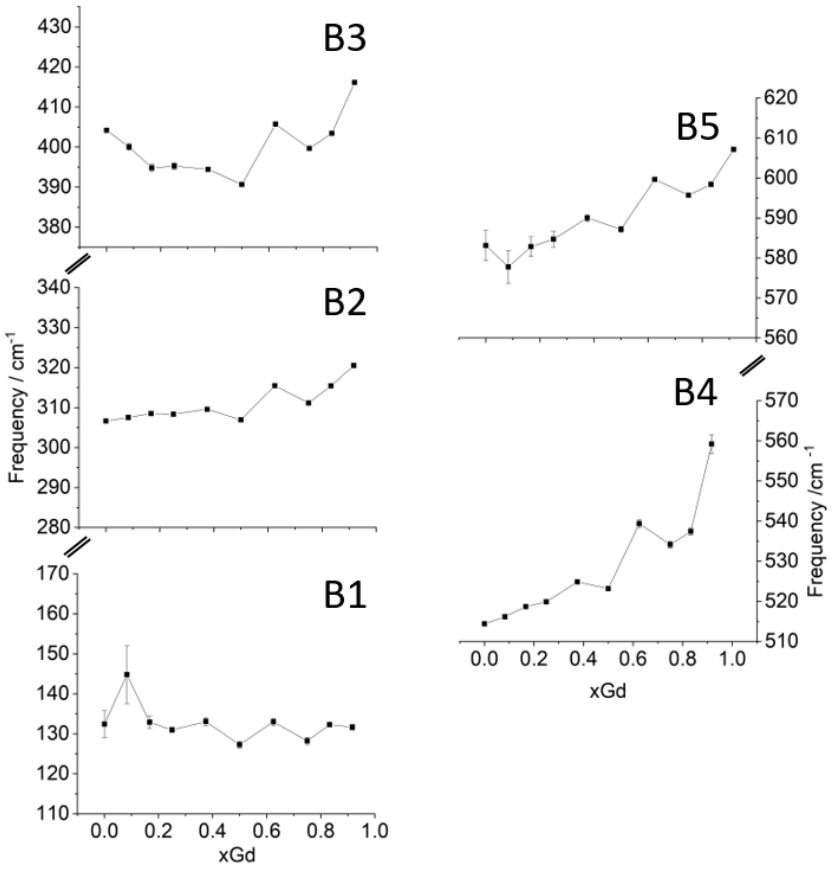

Figure 4.7 Frequency of vibrational bands in the Raman spectra of $(Nd_{1-x}Gd_x)_2Zr_2O_7$ solid solution as a function of Gd-content.

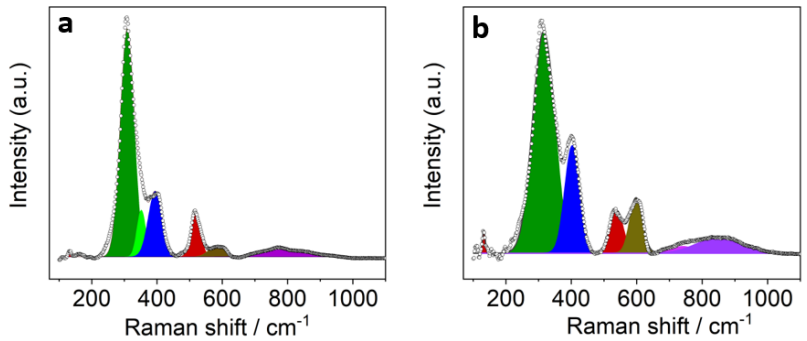

Figure 4.8 Selected fits with Gaussian functions of Raman spectra recorded on samples with xGd = (**a**) 0.167 and (**b**) 0.833.

The experimental spectra obtained in this study closely reproduce those previously documented in the literature for $(Nd_{1-x}Gd_x)_2Zr_2O_7$ compositions[48] or related systems like $Nd_{2-y}Y_yZr_2O_7$[160] and $Nd_{1-x}Dy_xZr_2O_7$[161]. Starting from the $Nd_2Zr_2O_7$ endmember (x_{Gd} = 0.000 in Figure 6.5), B1 is barely noticeable around 132 cm^{-1} and it seems to increase in intensity on Gd-substitution, though remaining quite weak. The most intense band B2 around 300 cm^{-1} clearly broadens with increasing x_{Gd}, while being blue-shifted. The band B3 at ≈400 cm^{-1} grows in intensity and, after an initial red-shift with x_{Gd}, it appears to be blue-shifted for $x_{Gd} \geq 0.625$. The second most intense line in the spectrum of $Nd_2Zr_2O_7$ is B4 around 500 cm^{-1} with a shoulder near 520 cm-^{1}. The increase in Gd-content results in a decrease in intensity and broadening of B4, which merges with the weak band at ≈520 cm^{-1}. At the same time, a new band (B5) around 580 cm^{-1}, barely visible in the spectra of Nd-rich compositions, grows and moves towards higher wavenumbers upon Gd-addition. Furthermore, a broad spectral feature can be recognized in the high-wavenumber region of the spectra around 800 cm^{-1} (see Figure 4.8). The changes in the spectra of $(Nd_{1-x}Gd_x)_2Zr_2O_7$ compositions with chemical substitution closely resembles those of $Gd_2(Ti_{1-x}Zr_x)_2O_7$ samples presented in the previous chapter. Therefore, the band B4 can be assigned to the closely spaced A_{1g} and T_{2g} vibrational modes of the pyrochlore structure (note that here in $Nd_2Zr_2O_7$ the splitting is more evident compared to $Gd_2Ti_2O_7$), while the band B2 is actually a superposition of two peaks related to the E_g and to one of the T_{2g}. vibrational modes[49]. B1 might be assigned to a forbidden IR mode activated by structural distortions at the local scale and involving A-site cations[11,176]. Two of the

remaining T_{2g} modes can be attributed to the spectral lines B3 and B5[48]. However, an alternative assignment will be proposed for the B5 line. Additionally, one of the T_{2g} modes has been linked to the weak band at approximately 520 cm^{-1}, which is noticeable in the spectrum of $Nd_2Zr_2O_7$ [177–180]. The broad feature present in the spectra of $(Nd_{1-x}Gd_x)_2Zr_2O_7$ compositions around 800 cm^{-1} (refer to Figure 4.8) has been also observed in the spectra of $Gd_2(Ti_{1-x}Zr_x)_2O_7$ samples with lower wavenumbers (see previous chapter). A similar band was reported for the spectra of pyrochlore compounds with U incorporated at the B-site of the structure and it is likely a result of a combination of multiple vibrational modes arising from distortions of the B-site polyhedron[180,181].

The two main bands B2 and B4 progressively broaden with Gd-substitution. The corresponding FWHM is plotted in Figure 4.9.

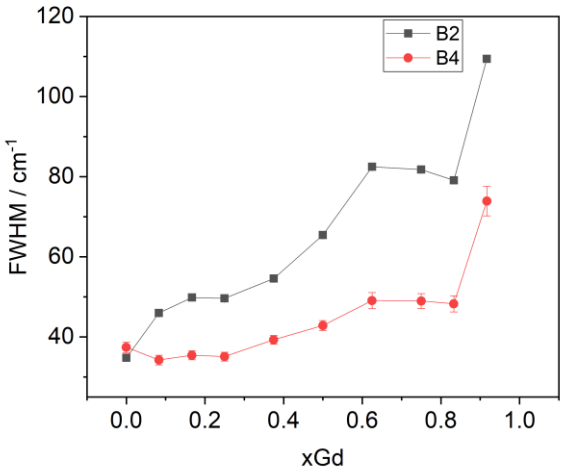

Figure 4.9 FMWH for Raman bands B2 and B4 in the $(Nd_{1-x}Gd_x)_2Zr_2O_7$ series as a function of Gd-content.

The broadening of Raman bands has been associated with increasing structural disorder at the local scale in the form of defects and vacancies, which allow a relaxation of the $k = 0$ selection rule and the combination of non-zone-center phonons[48]. In their work on the $(Nd_{1-x}Gd_x)_2Zr_2O_7$ system, Mandal and co-workers argued that a direct relationship exists between the increasing width of Raman bands with chemical substitution and disorder generated by cation antisite defects[48]. On the other hand, the analysis of the average structure of these compositions performed in the present thesis, revealed that the concentration of cation antisite defects remains low throughout the solid solution, whereas that of anion Anti-Frenkel defects increases. Therefore, the broadening of the Raman bands can be ascribed solely to disorder of anions by Anti-Frenkel defects formation. In addition, the variation in the

intensity of spectral lines B4 and B5 can be explained with an argument similar to that used in the previous chapter on $Gd_2(Ti_{1-x}Zr_x)_2O_7$ solid solution. The gradual filling of the O3 (*8a*) site with oxygen atoms from the O1 site would activate a new vibrational mode, which can be associate to line B5. The depletion of O1 site results in a loss of intensity of B4 (Figure 4.10). The filling of the O3 site leads also to an increase in the O1-O3 interaction, which in turn results in the blue-shift of B4 and B5 bands (Figure 4.7).

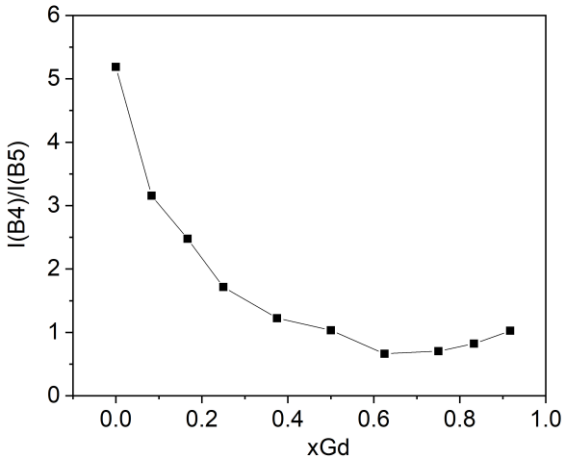

Figure 4.10 Intensity ratio between Raman bands B4 and B5 in the $(Nd_{1-x}Gd_x)_2Zr_2O_7$ series as a function of Gd-content.

To further understand the source of the structural disorder, the local structure was analyzed by means of PDF.

G(r) of $(Nd_{1-x}Gd_x)_2Zr_2O_7$ compositions in the low-r region are plotted in Figure 4.11. Values of peak position and FWHM for the first M-M correlation as obtained from single peak fitting are reported in Figure 4.12.

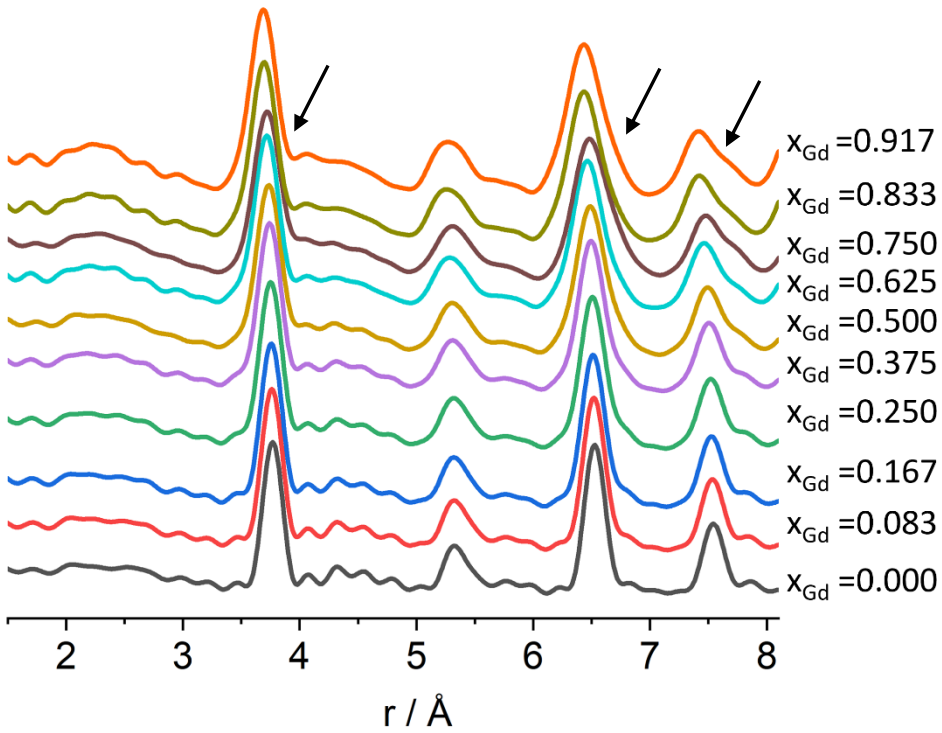

Figure 4.11 G(r) of $(Nd_{1-x}Gd_x)_2Zr_2O_7$ compounds between 1.8 and 8.0 Å. PDFs were normalized and offset on the Y axis for a better comparison. Black arrows indicate the new M-M correlations arising with Gd-doping.

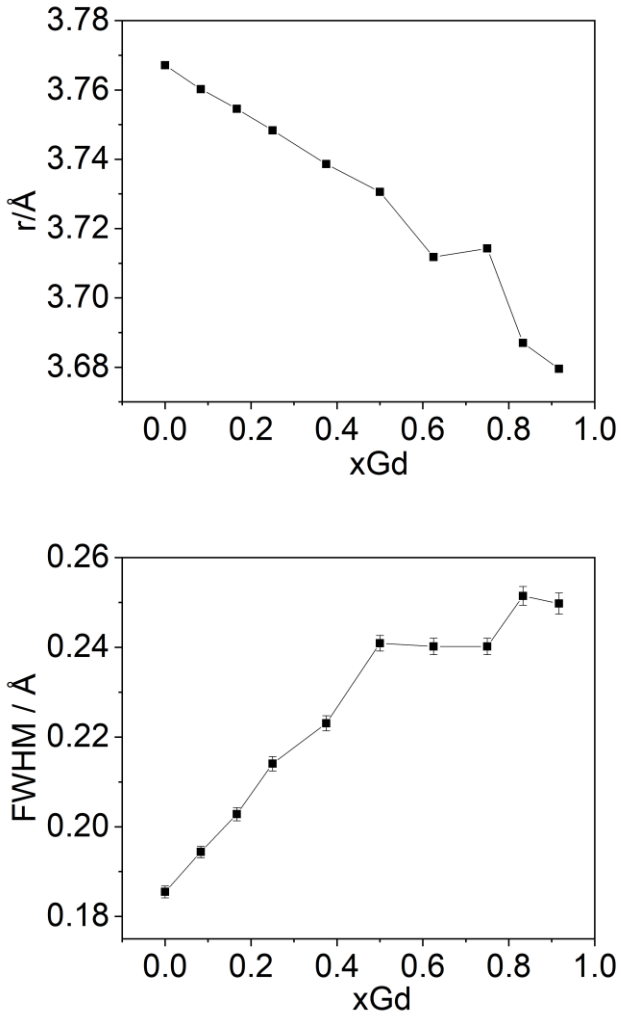

Figure 4.12 Peak r value (top) and FWHM (bottom) for the first M-M correlation in the PDFs of $(Nd_{1-x}Gd_x)_2Zr_2O_7$compounds

The gradual addition of Gd^{3+} in place of Nd^{3+} in the system causes a shift of the peaks towards lower r-values (see for example Figure 4.12, top) in accordance with the decrease of cell dimension already observed at the average scale. As in the case of $Gd_2(Ti_{1-x}Zr_x)_2O_7$ samples, a progressive broadening of the peaks occurs (Fig. 4.12, bottom) together with the appearance of new M-M correlations around 4.0, 6.7 and 7.5 Å (black arrows in Fig. 4.11). Again, these observations suggest an increase in structural disorder in compositions close to the $Gd_2Zr_2O_7$ endmember.

The pyrochlore model was employed to fit all the PDFs between 1.8 and 8.0 Å. Selected fits are shown in Figure 4.13.

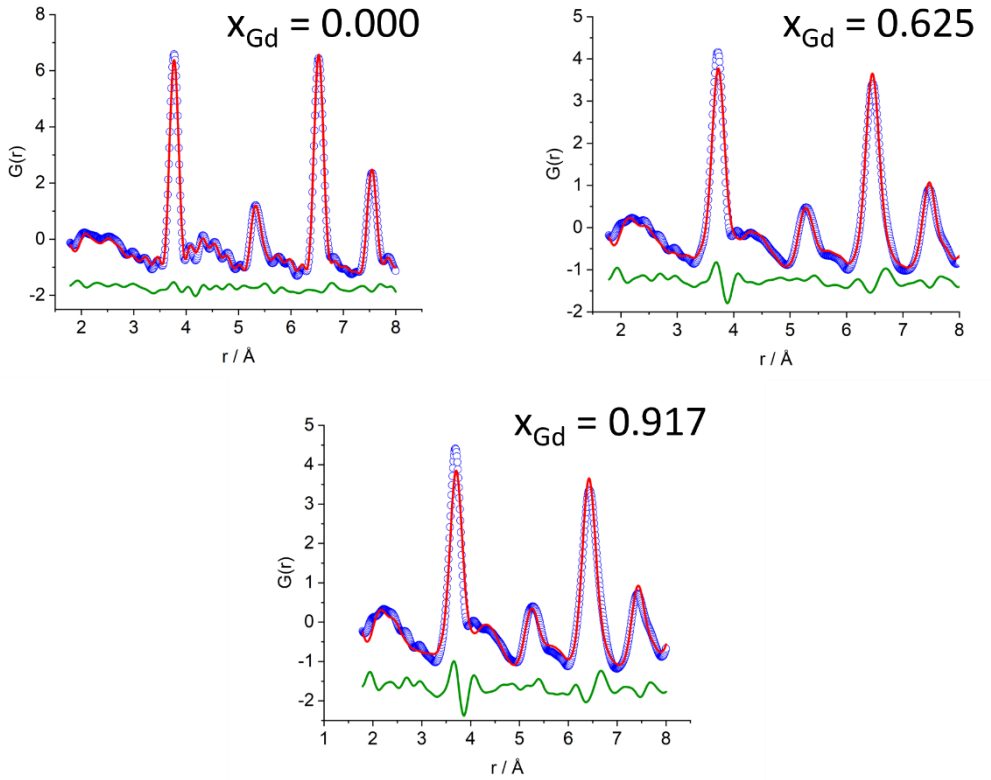

Figure 4.13 Selected G(r) of $(Nd_{1-x}Gd_x)_2Zr_2O_7$ solid solutions fitted between 1.8 and 8.0 Å. Experimental G(r) are depicted by blue circles, calculated G(r) by red lines and difference curves are in green.

Another parallelism can be pointed out with the $Gd_2(Ti_{1-x}Zr_x)_2O_7$ solid solution. As the chemical substitution (x_{Gd}) increases, the pyrochlore model fails in capturing the local scale correlations in $(Nd_{1-x}Gd_x)_2Zr_2O_7$ compositions. The misfits highlighted by the difference curves in Figure 4.13 cannot be resolved by simply introducing anion Anti-Frenkel and cation antisite defects, as was done in the case of the analysis

of the average structure, where a disordered pyrochlore model was employed. The origin of the misfits is in the modulation of metal-metal distances, which is not allowed by neither the ideal nor the defective pyrochlore structure. Consistent with the findings in $Gd_2(Ti_{1-x}Zr_x)_2O_7$ samples, these modulations are restricted to the very local scale. Indeed, good fits were obtained when the pyrochlore model was used to fit the experimental PDFs in a higher r-range (9-22 Å). In Figure 4.14 the resulting

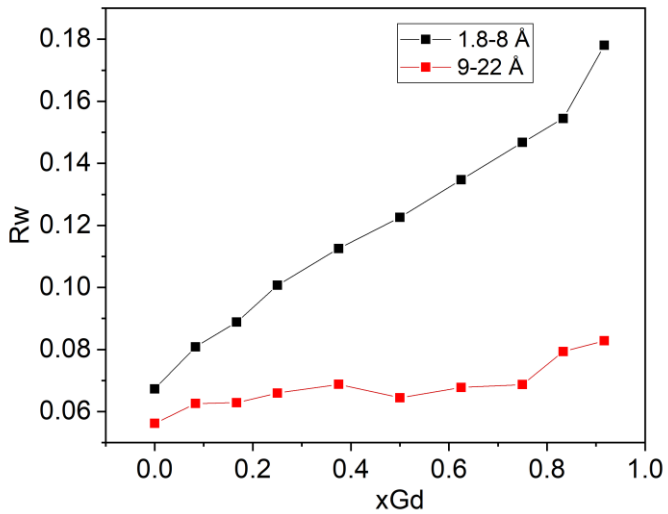

Figure 4.14 Rw values of PDF fits in the 1.8-8.0 (black) and 9-22 (red) Å windows with the pyrochlore model in $(Nd_{1-x}Gd_x)_2Zr_2O_7$ series as a function of Gd-content.

Rw for the fits in the two probed r-windows are plotted as a function of Gd-content.

The similarities between $(Nd_{1-x}Gd_x)_2Zr_2O_7$ and $Gd_2(Ti_{1-x}Zr_x)_2O_7$ compositions in the PDFs suggest that the short-range structure might be described by a similar model.

Part 5

$Gd_2(Zr_{1-x}Ce_x)_2O_7$ solid solution

The following samples were synthesized by solid-state reaction starting from Gd_2O_3, CeO_2 and ZrO_2 as precursors.

Compound	Annealing cycles (#)
$Gd_2(Zr_{0.917}Ce_{0.083})_2O_7$	7
$Gd_2(Zr_{0.833}Ce_{0.167})_2O_7$	7
$Gd_2(Zr_{0.750}Ce_{0.250})_2O_7$	7
$Gd_2(Zr_{0.625}Ce_{0.375})_2O_7$	7
$Gd_2(Zr_{0.500}Ce_{0.500})_2O_7$	7
$Gd_2(Zr_{0.375}Ce_{0.625})_2O_7$	7
$Gd_2(Zr_{0.250}Ce_{0.750})_2O_7$	7
$Gd_2(Zr_{0.167}Ce_{0.833})_2O_7$	7
$Gd_2(Zr_{0.083}Ce_{0.917})_2O_7$	7
$Gd_2Ce_2O_7$	6

HR-XRD patterns of $Gd_2(Zr_{1-x}Ce_x)_2O_7$ series in the Q-range between 0.5 and 3.5 $Å^{-1}$ are displayed in Figure 5.1. Reflections are indexed according to a fluorite cell. The solid solution experiences two phase transitions at the average scale. Following the compositional coordinate 'x_{Ce}', the Zr-rich samples in the phase diagram, specifically those with x_{Ce} = 0.083 and 0.167, adopt the pyrochlore structure. The samples in the central part of the phase diagram with $0.250 \leq x_{Ce} \leq 0.833$, form a defect fluorite structure, while those with x_{Ce} = 0.917 and 1.00 exhibit a C-type structure.

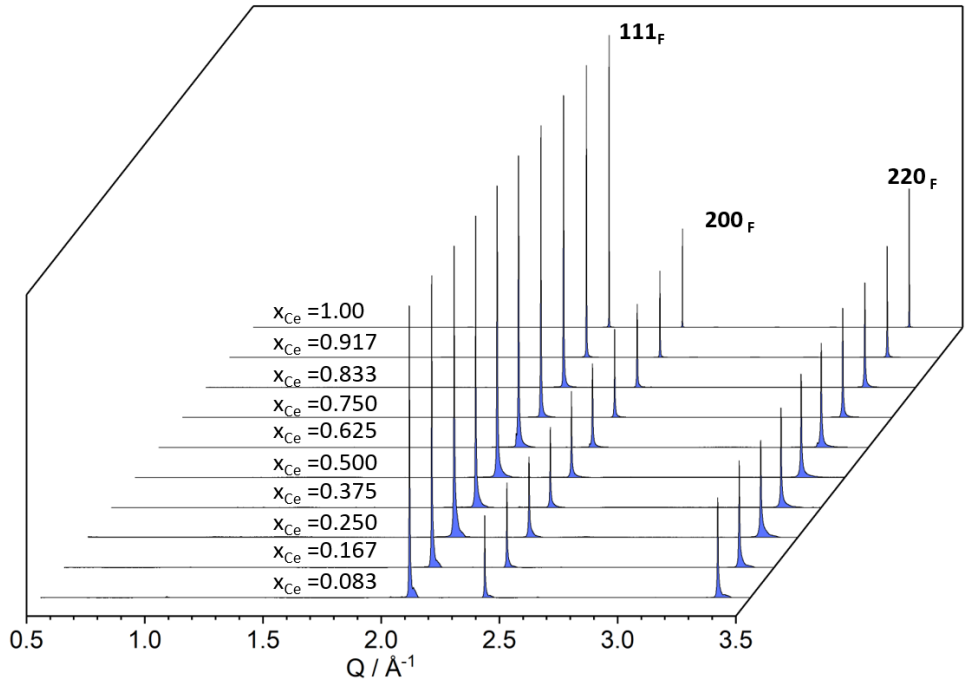

Figure 5.1 Evolution of HR-XRD patterns of $Gd_2(Zr_{1-x}Ce_x)_2O_7$ series with xCe in the Q-range 0.5 – 3.5 $Å^{-1}$. Patterns were normalized and offset in a 3D graph for a better comparison. Reflections are indexed according to a fluorite cell.

Although present, superstructure peaks are not visible in Figure 5.1. For this reason, a close-up view of the low-Q region for selected compositions is provided in Figure 5.2. 111_P pyrochlore peak for compositions with $x_{Ce} = 0.083, 0.167$ is weak yet sharp, with discernible diffuse scattering underneath. For $x_{Ce} = 0.250$, the pyrochlore peak 111_P is hardly visible and its intensity is comparable to that of other weak peaks

belonging to spurious phases. Similarly, 211_C superstructure peak indicating C-type ordering in samples with x_{Ce} = 0.917, 1.00 is also relatively weak, but noticeably broader compared to the pyrochlore reflection. At the same time, the corresponding fluorite (structure) peaks are quite sharp in all the compositions (Figure 5.1). This behavior has been already observed in Ln-doped CeO_2 and it was attributed to the emergence of antiphase boundaries between C-type nanodomains growing in the

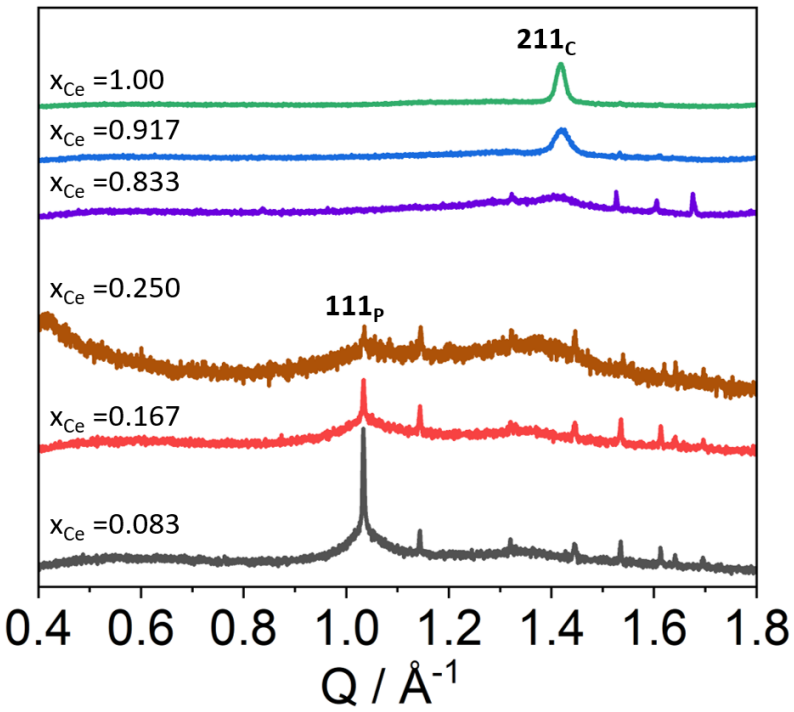

Figure 5.2 Detail of selected HR-XRD patterns in the low-Q region. Unindexed reflections suggest the presence of spurious phases produced in the solid state synthesis.

sample matrix[20,128].

Rietveld refinements were performed to analyze HR-XRD patterns and extract structural parameters. For x_{Ce} = 0.083, 0.167, a disordered pyrochlore model was adopted, as in the case of $Gd_2(Ti_{1-x}Zr_x)_2O_7$ and $(Nd_{1-x}Gd_x)_2Zr_2O_7$ solid solutions already discussed. In particular, the cell constant was refined for the structural model along with *x*O1 and isotropic displacement parameters (U_{iso}) of A, B and O sites. The occupation factor of O3 (o.f.(O3)) and that of Zr at the A site (o.f. (Zr_A)) were also allowed to vary with opportune constraints to avoid stoichiometry changes (see Part 3). The patterns of the defect fluorite compositions in the range $0.250 \leq x_{Ce} \leq 0.833$ were analysed with a defect fluorite model (general formula $(A,B)_4O_7$). In this case, all three cations were placed at the *4a* site of the structure. Half of it was occupied by Gd^{3+}, while the other half was portioned between Zr^{4+} and Ce^{4+} according to the nominal stoichiometry of the sample. The occupation of the oxygen site *8c* was set to 0.875. The cell constant and two U_{iso} parameters were refined (one for cations and one for the oxygen atom). Lastly, the patterns of compositions showing C-type ordering (x_{Ce} = 0.917, 1.00) were treated with a C-type structural model, in which cations were distributed over *8b* and *24d* sites and anions over *48e* and *16c* sites. Again, half of the cationic sites was reserved for Gd^{3+} and the other half was partitioned between Zr^{4+} and Ce^{4+}. The occupation of the oxygen site *16c* was set to 0.5. Beside the lattice constant, the coordinates of oxygen sites *48e* and *16c*, the *x*

coordinate of cationic site *24d*, and an isotropic displacement parameter for cations and one for oxygen atoms were allowed to vary.

In line with the findings already presented in the previous solid solutions, it was observed that the samples were not completely homogeneous, as a result of the solid-state process employed for the synthesis of the materials. Additional intensity at higher Q values, detected at the tails of the main phase peaks (Figure 5.1 and Figure 5.3), indicated the presence of secondary phases. To account for this residual intensity, a supplementary phase with the same structure and composition as the main phase but with a different lattice constant was included in the refinement. Specifically, for compositions with x_{Ce}= 0.083, 0.167, a second pyrochlore phase was added to the refinement, along with a third phase with a defect fluorite structure (Figure 5.3a) in analogy with compositions in solid solution $(Nd_{1-x}Gd_x)_2Zr_2O_7$ with x_{Gd} = 0.625, 0.750, 0.833, 0.917 (see Part 4). It appeared that in the present case, the homogeneity of the samples increased with increasing Ce-content.

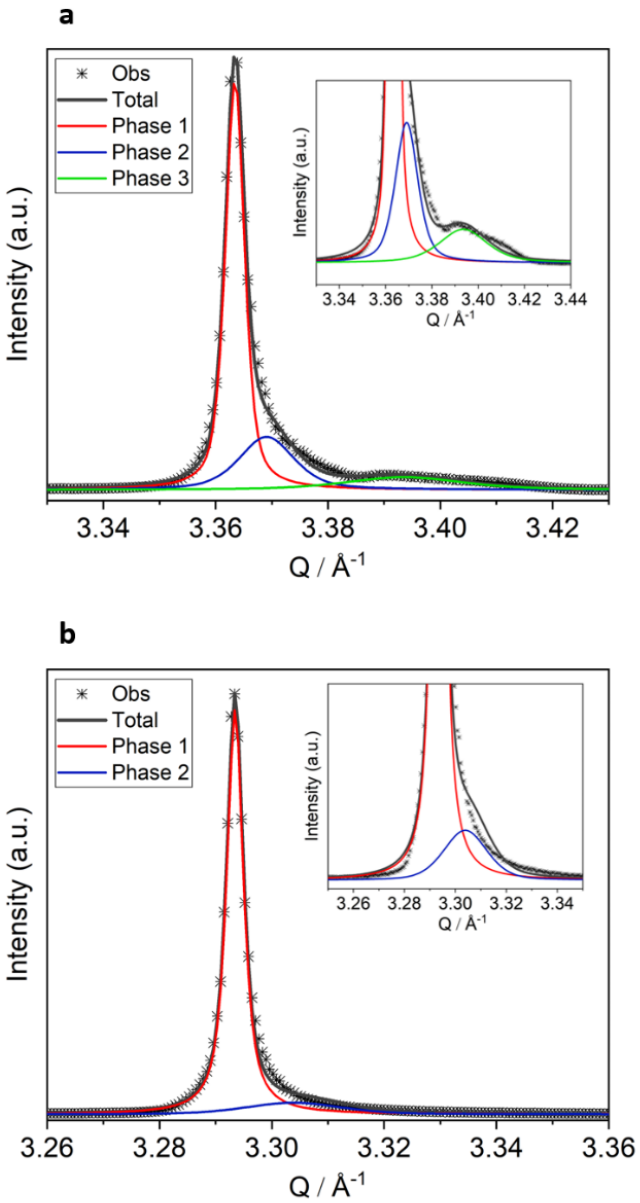

Figure 5.3 Detail of 220_F reflection (indexed according to a fluorite cell) in HR-XRD patterns of compositions with xCe = (**a**) 0.083 and (**b**) 0.750. Symbols represent the observed pattern, while solid lines are the calculated profile by Rietveld refinement.

Considering only the fluorite sub-structure in the $Gd_2(Zr_{1-x}Ce_x)_2O_7$ series, the substitution of Zr^{4+} with Ce^{4+} leads to an expansion of the unit cell commensurate with the different ionic sizes of the cations. This is evidenced by the shift of fluorite peaks towards lower Q-values in HR-XRD patterns (see for example Figure 5.3). The variation of the pseudofluorite cell parameter in $Gd_2(Zr_{1-x}Ce_x)_2O_7$ solid solution is shown in Figure 5.4. Half of the refined unit cell parameter was considered for those compositions adopting pyrochlore or C-type superstructures.

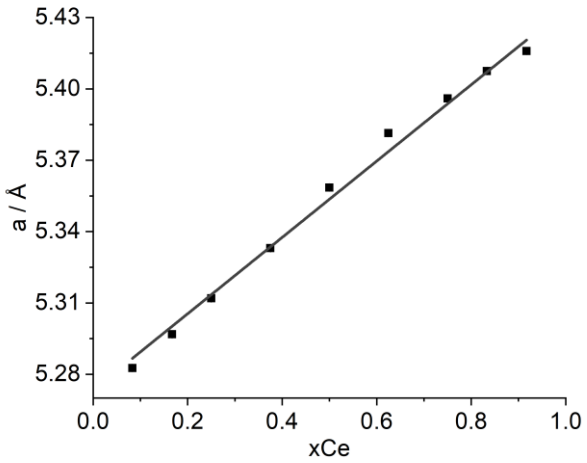

Figure 5.4 Pseudofluorite unit cell parameter in $Gd_2(Zr_{1-x}Ce_x)_2O_7$ solid solution as a function of Ce-content. Solid line is a linear fit to the data.

The plot in Figure 5.4 shows how the pseudofluorite unit cell parameter changes in an almost linear fashion with x_{Ce}.

Examining the pyrochlore compositions (x_{Ce} = 0.083, 0.167), a mismatch in the position between the calculated and observed profile for the superstructure peaks was found (Figure 5.5).

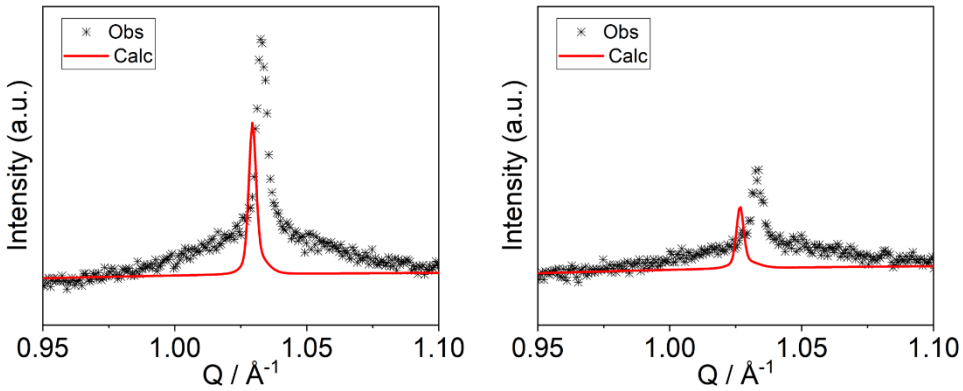

Figure 5.5 Close-up view in the low-Q region of the 111_P pyrochlore reflection for compositions $Gd_2(Zr_{0.917}Ce_{0.083})_2O_7$ (left) and $Gd_2(Zr_{0.833}Ce_{0.167})_2O_7$ (right). Symbols represent the observed pattern, while solid red line is the calculated profile.

The calculated profile for pyrochlore superstructure peaks was invariably shifted to lower Q-values with respect to the experimental patterns. At the moment, it is not clear the origin of such mismatch.

Parameters extracted from Rietveld refinements of HR-XRD patterns of compositions with x_{Ce} = 0.083, 0.167 are summarized in Table 5.1. Data for x_{Ce} = 0.0 ($Gd_2Zr_2O_7$) are also provided for comparison. As can be seen, these compositions attained a highly disordered pyrochlore structure. The value of *x*O1 reveals that the oxygen at the *48f* site is close to the position it would have in a defect fluorite

structure (xO1 = 0.375). At the same time, occupation of the O3 site is near 90 %. Taking into account multiplicities of O1 (48) and O3 (8) sites, this means that almost 15 % of oxygens O1 have formed Anti-Frenkel defects with vacant O3 sites. Fort the $Gd_2Zr_2O_7$ sample, only 6% of oxygens O1 have formed Anti-Frenkel pairs with O3 sites.

Table 5.1 Parameters obtained from Rietveld refinement of HR-XRD patterns of compositions $Gd_2Zr_2O_7$, $Gd_2(Zr_{0.917}Ce_{0.083})_2O_7$ and $Gd_2(Zr_{0.833}Ce_{0.167})_2O_7$.

xCe		**0**	**0.083**	**0.167**
Phase 1 s.g. $Fd\bar{3}m$	Weight Fraction %	89.6	64.9	65.0
	a / Å	10.52304(2)	10.56677(3)	10.59517(3)
Phase 2 s.g. $Fd\bar{3}m$	Weight Fraction %	10.4	23.3	25.1
	a / Å	10.4790(6)	10.5490(2)	10.5697(2)
Phase 3 s.g. $Fm\bar{3}m$	Weight Fraction %	-	11.8	9.9
	a / Å	-	5.2365(2)	5.2494(3)
xO1		0.34698(4)	0.3724(9)	0.372(1)
o.f.(O3)		0.40(1)	0.89(3)	0.95(3)
o.f.(Zr_A)		0.048(2)	0.190(4)	0.375(5)
Uiso / $Å^2$	A	0.01135(8)	0.0172(3)	0.0172(4)
	B	0.0182(2)	0.0164(4)	0.0175(5)
	O	0.0233(9)	0.0495(9)	0.0453(8)
wRp(%)		7.6	10.3	9.7

An increase in antisite cation defects is observed as well. It is reasonable to assume that in this system it is Ce^{4+} that firstly replace the Gd^{3+} at the A-site of the structure rather than Zr^{4+}. However, refining the occupancy of Ce at the A-site lead to negative values for the occupation factor of Ce at the B-site and, consequently, only Zr and

Gd were considered in the formation of cation antisite defects. The o.f.(Zr_A) goes from 0.048 in $Gd_2Zr_2O_7$ to 0.190 in $Gd_2(Zr_{0.917}Ce_{0.083})_2O_7$ and 0.375 in $Gd_2(Zr_{0.833}Ce_{0.167})_2O_7$ samples, indicating an escalation of disorder in the cations array. The radii ratio r_A/r_B calculated with the nominal occupancies at the A- and B-sites is around 1.44 for $x_{Ce} = 0.083$ and 1.41 for $x_{Ce} = 0.167$. The value that defines the boundary for the pyrochlore/defect fluorite stability field is 1.46 ($Gd_2Zr_2O_7$, see Part 1). The fact that a pyrochlore structure is found also for these compositions with low Ce-content is in line with previous investigations, reporting an enlargement of the stability field of the pyrochlore structure well beyond the limiting value due to cation antisite defects[182].

HR-XRD of compositions in the range $0.250 \leq x_{Ce} \leq 0.833$ were analysed by using a defect fluorite model in the Rietveld refinements. Relevant parameters are reported in Table 5.2. The variation of the isotropic displacement parameters (U_{iso}) for metal and oxygen atoms in this series is plotted in Figure 5.6.

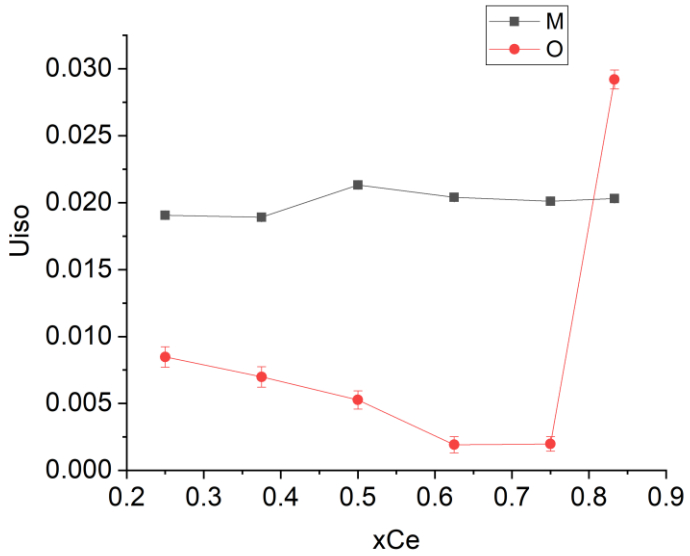

Figure 5.6 U_{iso} of metal (black) and oxygen atoms in compositions $0.250 \leq xCe \leq 0.833$ as a function of Ce-content.

U_{iso} values obtained for the cations are surprisingly higher than those obtained for the anions and do not show any significant trend. On the other hand, those for oxygen anions gradually decrease up to $x_{Ce} = 0.750$. A sudden increase is observed for $x_{Ce} = 0.833$. This trend might suggest that static disorder in the anion array decreases in the defect fluorite part of the phase diagram before being enhanced at the onset of the C-type phase transition.

Table 5.2 Parameters obtained from Rietveld refinement of HR-XRD patterns of compositions $0.250 \leq xCe \leq 0.833$. Estimated standard deviation values are in parentheses. Those of weight fractions are not indicated because underestimated by the software.

xCe		**0.250**	**0.375**	**0.500**	**0.625**	**0.750**	**0.833**
Phase 1 s.g $Fm\bar{3}m.$	Weight Fraction %	68.9	74.7	80.6	84.0	89.3	88.2
	a / Å	5.31192(2)	5.33302(2)	5.35852(2)	5.38141(2)	5.39596(1)	5.40752(1)
Phase 2 s.g $Fm\bar{3}m$	Weight Fraction %	31.1	25.3	19.4	16.0	10.7	11.8
	a / Å	5.2894(2)	5.3042(2)	5.3278(2)	5.3563(3)	5.3715(3)	5.3912(2)
Uiso / $Å^2$	A	0.01906(8)	0.01891(8)	0.02133(8)	0.02039(7)	0.02015(8)	0.02028(8)
	O	0.0085(8)	0.0070(8)	0.0053(7)	0.0020(6)	0.0016(6)	0.0292(7)
wRp(%)		8.7	10.5	9.0	9.6	10.7	11.4

Results of Rietveld refinements for HR-XRD of C-type samples (x_{Ce} = 0.917, 1.00) are provided in Table 5.3.

Table 5.3 Parameters obtained from Rietveld refinement of HR-XRD patterns of compositions xCe = 0.917, 1.00.

xCe		**0.917**	**1.00**
a / Å		10.83165(3)	10.85320(1)
s.g.		$Ia\bar{3}$	$Ia\bar{3}$
*x*M2		-0.00436(8)	-0.00526(7)
*x*O1		0.384(1)	0.3848(9)
*y*O1		0.138(1)	0.1364(9)
*z*O1		0.382(2)	0.382(1)
*x*O2		0.376(4)	0.375(3)
Uiso / Å^2	M	0.0212(1)	0.0210(1)
	O	0.019(1)	0.017(1)
wRp(%)		15.7	19.8

The results are in accordance with those reported by Grover et al.[35] and Scavini et al.[40] on microcrystalline samples in the Gd_2O_3-CeO_2 system with a C-type structure. However, in the present case the wRp values of the refinements are inexplicably high compared to the aforementioned studies and to the other refinements performed on HR-XRD patterns in this thesis. The reason for this behaviour is not clear at the moment. The Rietveld plots for compositions x_{Ce} = 0.917, 1.00 are displayed in Figure 5.7.

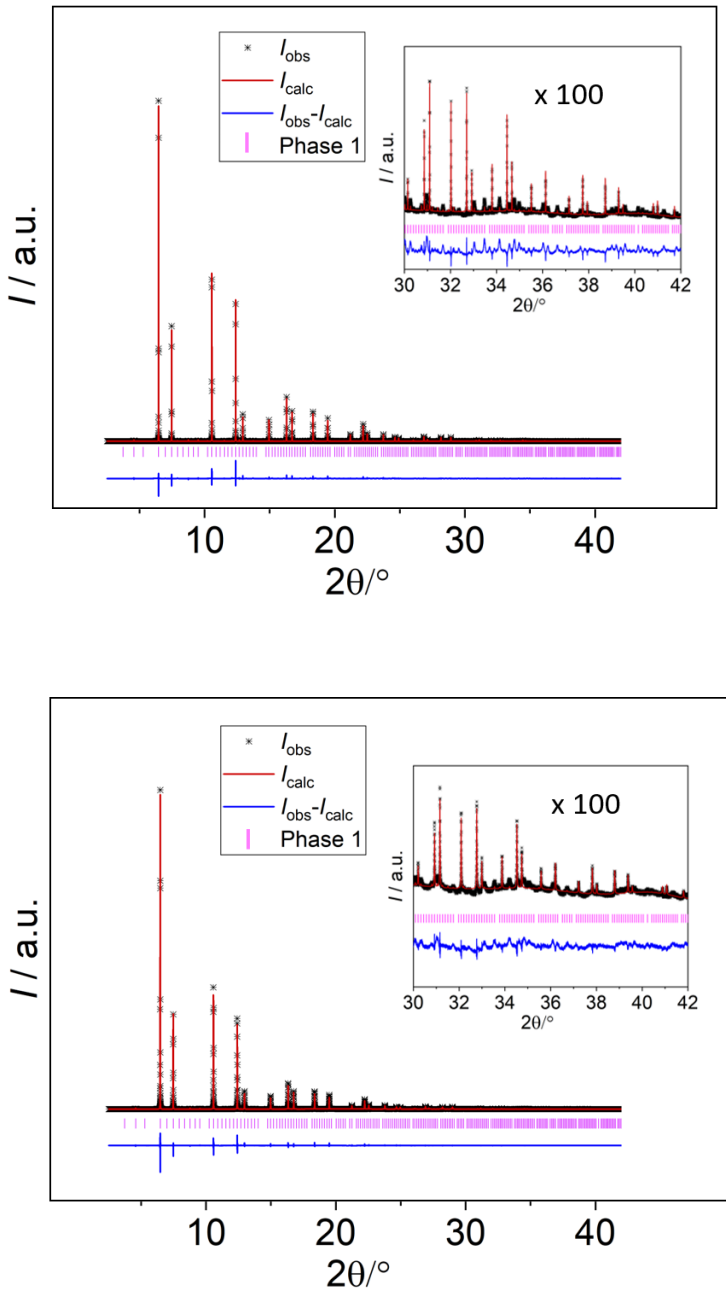

Figure 5.7 Rietveld refinements of synchrotron HR-XRD profiles of (top) $Gd_2Ce_2O_7$ and (bottom) $Gd_2(Zr_{0.083}Ce_{0.917})O_7$ samples

A systematic investigation on $Gd_2(Zr_{1-x}Ce_x)_2O_7$ solid solution has been conducted by Reid and colleagues[39]. XRD analysis indicated that samples with $0 \leq x_{Ce} \leq 0.125$ were pyrochlore-like, those with $0.125 < x_{Ce} < 0.825$ adopted a defect fluorite structure, while those with $0.825 \leq x_{Ce} \leq 1.00$ crystallized in the C-type structure. Considering that limiting compositions at the border of the pyrochlore/defect fluorite and defect fluorite /C-type regions showed weak and diffuse superstructure peaks, the phase diagram established by Reid and coworkers is consistent with that reported in this thesis. What is particularly intriguing is their analysis of superstructure reflections in electron diffraction patterns. Electron diffraction proved to be very sensitive to cations and anions ordering. In particular, defect fluorite compositions were characterized by disordered anions and vacancies, but with some degree of short-range cations correlations. Moreover, an incommensurate C-type structure was identified in the $Gd_2(Zr_{0.5}Ce_{0.5})_2O_7$ composition.

The analysis of HR-XRD patterns has revealed that the samples in this solid solution experience two phase transitions at the average scale. Raman spectroscopy provides further insights into the structural transformations that occur upon Ce-substitution. Raman spectra of $Gd_2(Zr_{1-x}Ce_x)_2O_7$ series are displayed in Figure 5.8. The overall profile of the spectra undergoes a profound change throughout the whole compositional range, much more than the spectra discussed for the solid solutions of the previous chapters.

In this case, the relevant vibrational bands that change and/or appear in the spectra upon Ce-substitution were labelled from P1 to P6. The frequency shifts obtained after background subtraction and fitting of the peaks with Gaussian functions are plotted in Figure 5.9, while selected fits are shown in Figure 5.10.

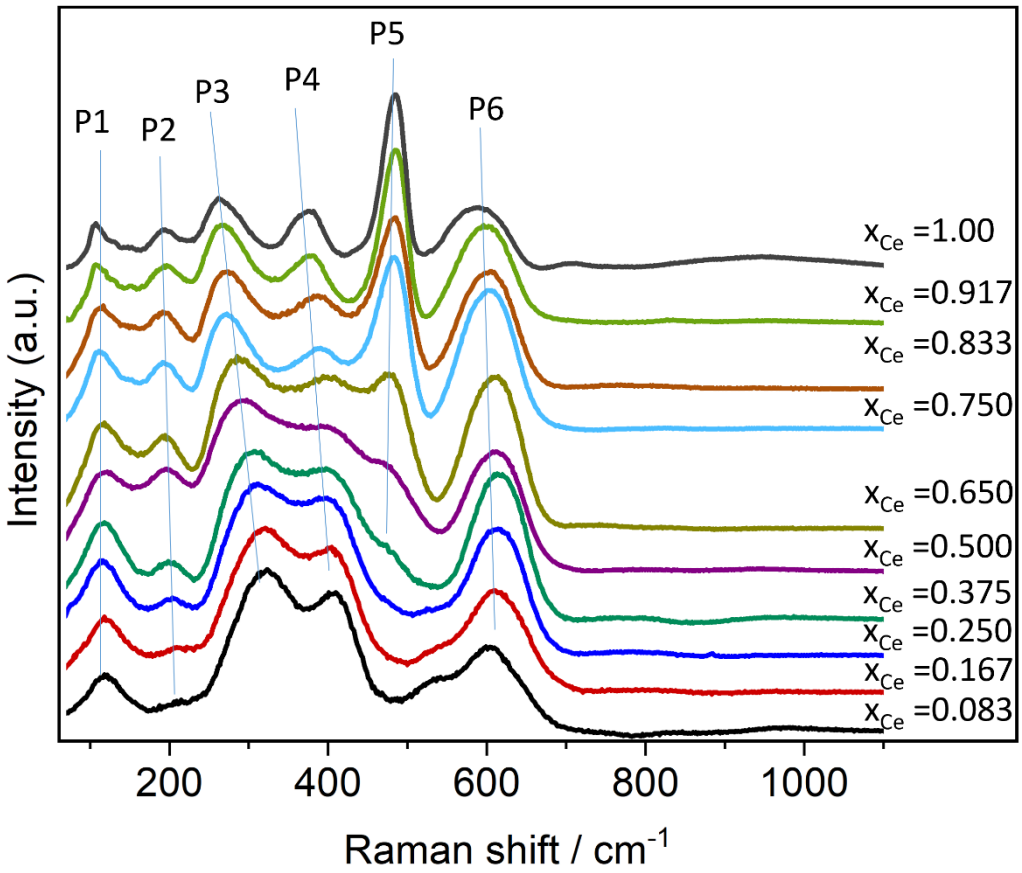

Figure 5.8 Raman spectra of $Gd_2(Zr_{1-x}Ce_x)_2O_7$ solid solution between 100 and 1100 cm^{-1} offset on the Y axis. After background subtraction, each spectrum was normalized between 0 and 100. The observed vibrational bands are labelled from P1 to P6

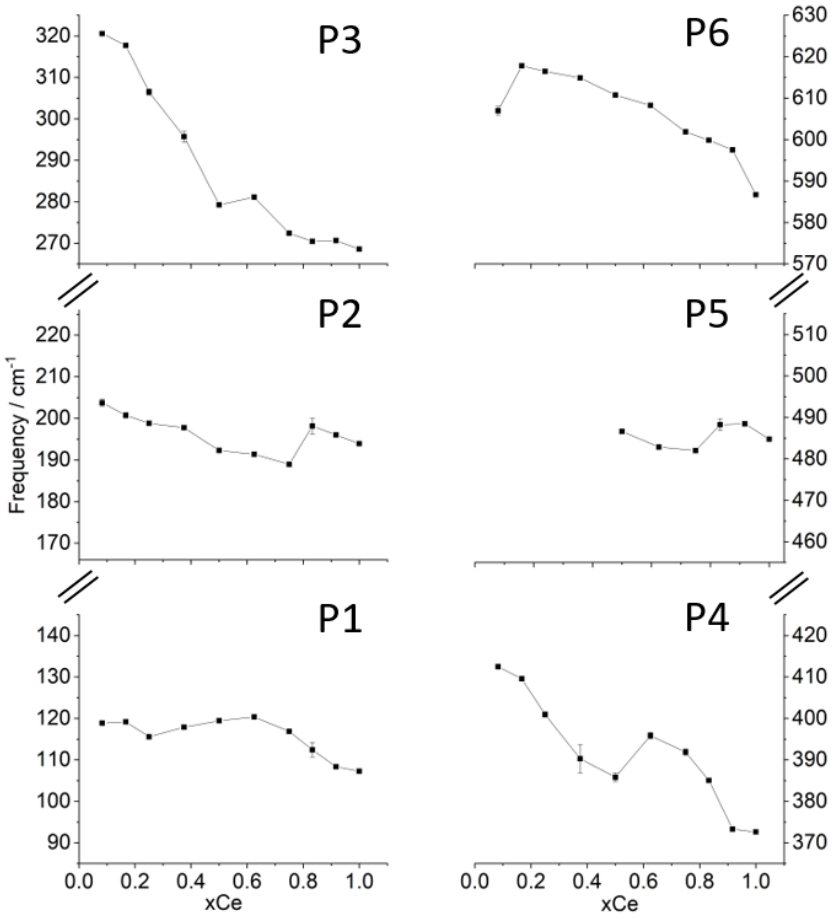

Figure 5.9 Frequency of vibrational bands in the Raman spectra of $Gd_2(Zr_{1-x}Ce_x)_2O_7$ solid solution as a function of Ce-content.

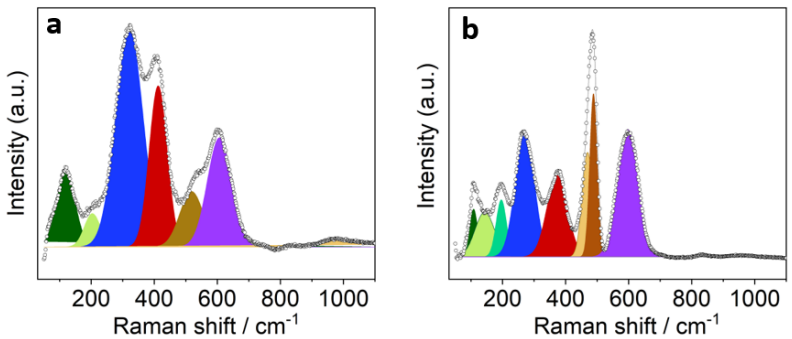

Figure 5.10 Selected fits with Gaussian functions of Raman bands in the spectra of compositions with xCe = (**a**) 0.083 and (**b**) 1.00.

The band P1 in the low-wavenumber region of the spectrum of composition $Gd_2(Zr_{0.917}Ce_{0.083})_2O_7$ around 120 cm^{-1} appears to sharpen on Ce-substitution, while being slightly red-shifted. A weak band around 205 cm^{-1} grows in intensity as the Ce-content rises, becoming clearly visible in the spectrum of $Gd_2Ce_2O_7$ endmember denoted as P2. The main spectral feature in the spectrum of $Gd_2(Zr_{0.917}Ce_{0.083})_2O_7$ sample at ≈ 320 cm^{-1} appears to broaden when Zr is substituted with Ce and, eventually, it evolves in the band P3 from composition with $x_{Ce} = 0.625$ onwards. A similar trend is observed for the other prominent band in the spectrum of $Gd_2(Zr_{0.917}Ce_{0.083})_2O_7$ sample at ≈ 412 cm^{-1}, as it broadens and shifts towards lower wavenumbers. Starting from $x_{Ce} = 0.625$, this band is identified as the peak marked P4, and is placed around 370 cm^{-1} in the spectrum of $x_{Ce} = 1.00$. A new spectral feature labelled P5 emerges at ≈ 486 cm^{-1} in the spectrum of composition with $x_{Ce} = 0.500$. P5 progressively sharpens and grows in intensity on Ce-substitution, ultimately becoming the most intense vibrational band in the spectrum of. $Gd_2Ce_2O_7$. The band indicated as P6 in Figure 5.8 around 600 cm^{-1} seems to grow and move towards lower wavenumbers as Zr is being substituted by Ce. A similar spectral evolution has been recently reported by Nandi and co-workers for the Raman spectra measured on the $Nd_2(Zr_{1-x}Ce_x)_2O_7$ series[178].

Only the spectra of samples with low Ce-content ($0.083 \leq x_{Ce} \leq 0.250$) resemble that of $Gd_2Zr_2O_7$, which, as discussed in Part 3, despite having a pyrochlore ordering at the long-range scale, was disordered at the local scale. As indicated by Rietveld

refinements, pyrochlore compositions with x_{Ce} = 0.083, 0.167 have a higher concentration of anion Anti-Frenkel and cation antisite defects than $Gd_2Zr_2O_7$. Notably, the Raman spectra also suggest an increase in structural disorder at the local scale. A band at ≈ 514 cm^{-1}, which is related to the A_{1g} mode of the pyrochlore structure and associated to the vibration of O1 in the [100] direction towards the vacant site O3[70,121,140], has almost disappeared in the spectra of $Gd_2(Zr_{0.917}Ce_{0.083})_2O_7$ and $Gd_2(Zr_{0.833}Ce_{0.167})_2O_7$ samples. In fact, the formation of Anti-Frenkel pairs through the occupation of vacant O3 site by O1 oxygen ions results in a decrease in intensity of the A_{1g} mode[105,144]. At the same time, a new mode is activated, which corresponds to the band P6[143] (see also Part 3). A general broadening induced by static disorder within the structure[100] affects the remaining pyrochlore bands at ≈ 320 cm^{-1} and 412 cm^{-1} and formally forbidden lines, such as P1 and P2, appear in the low wavenumbers region. These bands might be related to IR modes activated when displacive disorder of Gd and O2 ions lowers the local symmetry[104,134]. Samples in the compositional range $0.250 \leq x_{Ce} \leq 0.833$ adopt an average defect fluorite structure, though the limiting compositions of this series show evidence of weak and/or broad superstructure peaks related to pyrochlore (x_{Ce} = 0.250) or C-type (x_{Ce} = 0.833) ordering. It is worth remembering that compounds with an ideal fluorite structure exhibit only one spectral line related to a T_{2g} mode in the Raman spectrum[111], whereas defect fluorite compounds show a complete broadening of this band[49,100] (see also Part 2). In the present case, the Raman spectra of defect fluorite samples are characterized by different distinct bands. Clearly, those modes that

derived from the pyrochlore spectrum are quite broad, but they seem to sharpen in Ce-rich compounds and form new vibrational bands in the spectrum of $Gd_2Ce_2O_7$ (see for example P3 and P4). Other lines such as P1, P2 and P6 are also present and confirm that a certain degree of ordering is preserved at the local scale despite the long-range defect fluorite structure. Furthermore, the new band P5 gradually appears and intensifies in the spectra of these defect fluorite compositions. Samples with x_{Ce} = 0.917 and 1.00 exhibit a long-range C-type structure. Although 22 Raman active modes ($4A_g$+$4E_g$+$14T_g$) are derived by factor group analysis of a C-type structure, less than half of the predicted modes are observed experimentally[114]. In the series under analysis, the signature of C-type ordering is the band P4 at ≈ 370 cm^{-1}[138,183–185]. Banerji and coworkers observed a Raman band located around 370 cm^{-1} in the spectra of $Ce_{1-x}Gd_xO_{(2-x)/2}$ compounds[183]. This band originated from x_{Gd} = 0.2 and ultimately evolved in the line at ≈ 354 cm^{-1} in the Gd_2O_3 endmember, corresponding to the vibration of oxygens around Gd in six-fold coordination. A similar band has also been reported for Nd-[38], Sm-[184], Er-[186] and Yb-[187] doped CeO_2. However, the dominant peak in the spectra of C-type compounds (x_{Ce} = 0.917, 1.00) is P5 at ≈ 486 cm^{-1}. Previous studies have shown that a band near 480 cm^{-1} appears in the spectrum of doped ceria on increasing cationic substitution as a high-frequency shoulder of the T_{2g} mode of CeO_2 located at ≈ 465 cm^{-1} [183,185]. Banerji and colleagues interpreted this high-frequency component on the basis of different Ce-O and Gd-O interatomic distances as derived from EXAFS analysis. The Gd-O distances are always larger than the Ce-O distances in the Gd_2O_3-CeO_2 system[188]. Therefore, Gd-O distances

would experience a compressive stress in a CeO_2 matrix with a fluorite-like environment and, as a result, the Gd-O vibration would have a higher frequency with respect to the nominal value of 465 cm^{-1} reported for CeO_2[183]. Additional lines P3 and P6 at ≈ 268 and 586 cm^{-1} respectively in the spectrum of $Gd_2Ce_2O_7$ are commonly assigned in the literature to defects-induced bands[38,183,184,189]. In particular, the introduction of aliovalent cations like Gd^{3+} in the structure of CeO_2 causes the formation of anion vacancies for charge compensation. Different metal-oxygen-vacancy complexes can then give rise to different vibrations and new modes can be activated in the spectra[190]. Interestingly, looking at the phonon dispersion of CeO_2, there are two modes with frequency around 290 and 590 cm^{-1} at the centre of Brillouin zone, beside the T_{2g} mode with frequency 465 cm^{-1}. These modes have symmetry T_{1u} and are not Raman active. However, the presence of defects within the structure can relax the selection rules and allow for new modes to be activated and observed experimentally[185].

A closer inspection of the local structure was performed by PDF analysis. G(r) functions of $Gd_2(Zr_{1-x}Ce_x)_2O_7$ compositions in the low-r region are displayed in Figure 5.11. The peak position and FWHM for the first M-M correlation as obtained by single peak fitting are reported in Figure 5.12.

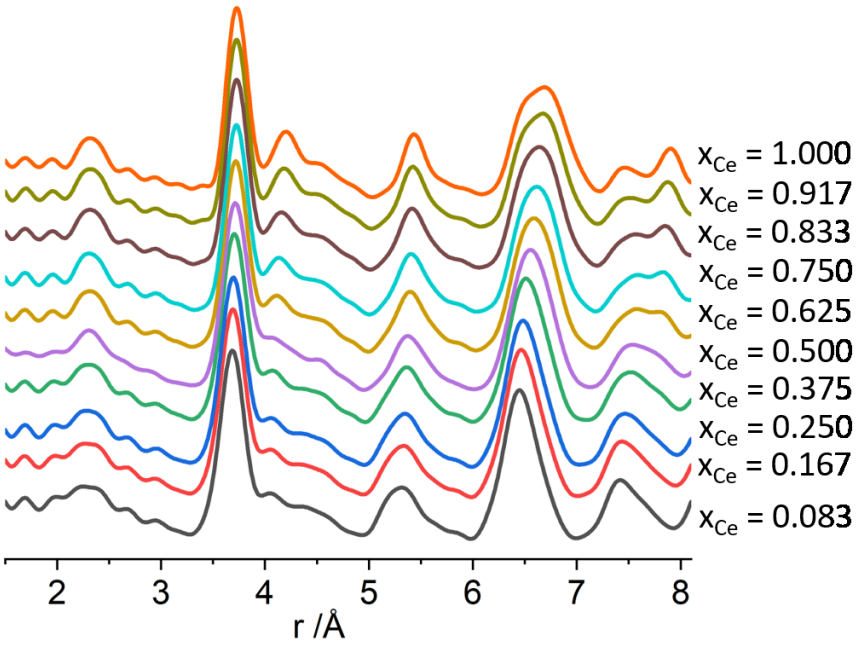

Figure 5.11 G(r) of $Gd_2(Zr_{1-x}Ce_x)_2O_7$ compounds between 1.8 and 8.0 Å. PDFs were normalized and offset on the Y axis for a better comparison.

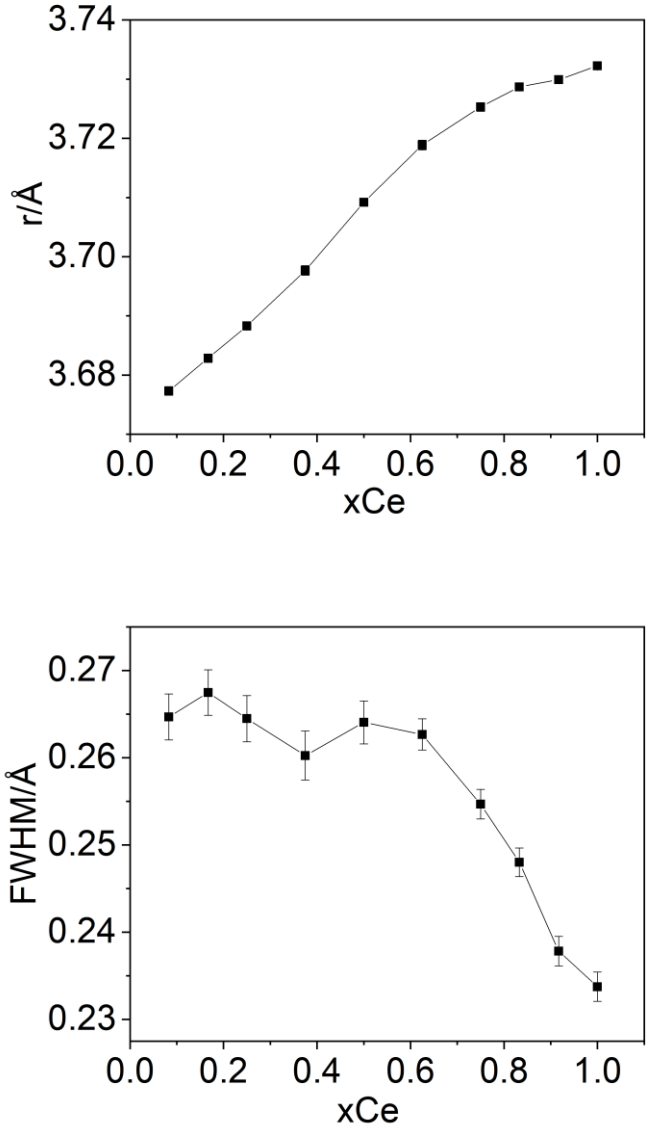

Figure 5.12 Peak position (top) and FWHM (bottom) for the first M-M correlation in the G(r) of $Gd_2(Zr_{1-x}Ce_x)_2O_7$ compounds as afunction of Ce-content.

As in the case of Raman spectra, a marked change of the G(r) is observed as a result of two phase transitions at the average scale. All the peaks move towards higher r-values on Ce-substitution in response to the expansion of the sub-cell detected at the average scale by HR-XRD (see for example Fig. 5.12, top). The first broad peak at ≈ 2.3 Å corresponding to M-O distances appears to sharpen on Ce-substitution. Similarly, a sharpening effect is also experienced by the peak around 3.7 Å, which is related to the first M-M distances in fluorite-oxides (see Fig. 5.12, bottom). A new M-M correlation emerges in Ce-rich samples at ≈4.1 Å. The peak around 5.3-5.4 Å also derives from M-M interatomic distances and is quite broad in the G(r) of sample with $x_{Ce} = 0.083$. Upon Ce-substitution, the peak sharpens and shift towards higher r-values. Another intense, although broad, peak is located near 6.4 Å. With increasing Ce-content, this feature appears to split into two components that are still very close to each other in the PDF of $Gd_2Ce_2O_7$ end member. The progressive Ce-doping in $Gd_2(Zr_{1-x}Ce_x)_2O_7$ samples leads also to the separation of two M-M correlations that can be found around 7.6-7.9 Å.

The short-range ordering of $Gd_2(Zr_{1-x}Ce_x)_2O_7$ compounds appear to be quite different from that already discussed in the previous chapters. In contrast to $Gd_2(Ti_{1-x}Zr_x)_2O_7$ and $(Nd_{1-x}Gd_x)_2Zr_2O_7$ solid solutions, the reduction of r_A/r_B with the compositional coordinate (x_{Ce}) is accompanied by a progressive sharpening of the main peaks associated with M-M correlations. This means that the corresponding interatomic distances become more uniform, with their values closely spaced around a certain r.

As can be evidenced from Figure 5.12 (bottom), the FWHM of the first M-M peak slightly diminishes up to $x_{Ce} = 0.625$, then rapidly decreases with the introduction of more Ce in the system.

The modelling of the PDFs of $Gd_2(Zr_{1-x}Ce_x)_2O_7$ solid solution in the low r-region through small box refinements is still at its first stages. However, preliminary tests using the structural models of the average structures have revealed that high residuals are obtained for all PDFs in the r-range 1.8-8.0 Å. Furthermore, Rw values steadily increase with increasing Ce-content (Figure 5.13). This finding suggests that, at the local scale, the deviation from the average structure becomes more pronounced as more Ce is introduced in the system. Interestingly, going beyond the very short-range scale and fitting the PDFs in the 9-22 Å interval with the average structural models, results in satisfactory fits for all the samples, although Rw values tend to increase in the Ce-rich part of the phase diagram. Distortions and deviations from the long-range structure might extend further in the mesoscopic scale for these compositions.

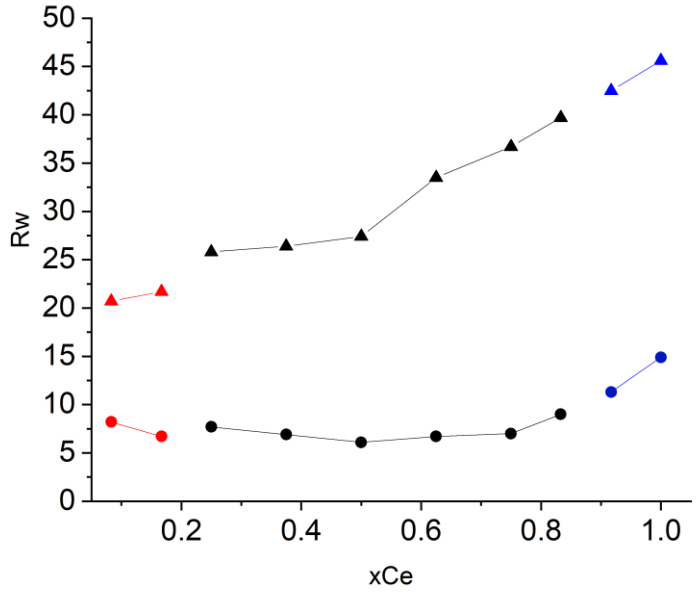

Figure 5.13 Rw values of PDF fits of $Gd_2(Zr_{1-x}Ce_x)_2O_7$ series in the 1.8-8.0 Å (triangles) and 9-22 Å (circles) window. A pyrochlore model has been adopted for xCe≤0.167 (red), a defect fluorite model for 0.250≤xCe≤0.833 (black) and a C-type model for xCe≥.0.917 (blue).

Conclusions and future prospects

A study on structural disorder in $A_2B_2O_7$ pyrochlore oxides has been performed within this PhD project. The focus of the work was the composition $Gd_2Zr_2O_7$, which exhibited high radiation resistance, making it a potential matrix for radionuclides disposal. The structural disorder was controlled through chemical substitution with isovalent cations at the A- and B sites. Solid solutions in the form of $Gd_2(Ti_{1-x}Zr_x)_2O_7$, $(Nd_{1-x}Gd_x)_2Zr_2O_7$ and $Gd_2(Zr_{1-x}Ce_x)_2O_7$ were produced and characterized at the average scale using High-resolution X-ray diffraction (HR-XRD) and at the short-range scale using Raman spectroscopy and the analysis of the Pair Distribution Function (PDF).

The solid-state synthesis was employed to prepare all the samples. Although the method is simple, long annealing steps with intermediate grounding of the reaction mixture are necessary to produce a homogeneous sample.

As confirmed by Rietveld refinements of HR-XRD patterns and PDF analysis, the gadolinium titanate $Gd_2Ti_2O_7$ is the more ordered sample of all the investigated compositions. In fact, it retains an almost ideal pyrochlore structure at both the long-range and short-range scale. However, small structural distortions have been detected even in $Gd_2Ti_2O_7$ by the appearance of additional weak vibrational bands in the Raman spectrum[108]. In the $Gd_2(Ti_{1-x}Zr_x)_2O_7$ and $(Nd_{1-x}Gd_x)_2Zr_2O_7$ solid-solutions a pyrochlore structure is retained throughout the whole series. Nevertheless, the

structural disorder increases as the radii ratio r_A/r_B decreases and the boundary between the stability fields of pyrochlore and defect fluorite structures is approached. A hierarchy of disorder between cations and anions is observed within the average structure. Initially, the anions form Anti-Frenkel pairs between the occupied O1 site and the vacant O3 site. As compositions converge to the $Gd_2Zr_2O_7$ endmember, cations begin to switch sites forming antisite defects. Regardless, an increase in isotropic displacement parameters directly indicates a rise in static disorder as r_A/r_B diminishes. The accumulation of disorder at the long-range scale leads to a progressive broadening of the pyrochlore vibrational bands in the Raman spectra. Notably, a new spectral feature at ≈ 600 cm^{-1} grows as the O3 site is being occupied and other forbidden bands appear, suggesting the presence of cations displacive disorder and a lowering of the local symmetry. Indeed, the analysis of the PDFs in the low-r region reveals that new metal-to-metal correlations arise in those samples with a low r_A/r_B value. These deviations from the average structure are limited to a sub nanometer scale (≈ r < 8 Å). The weberite-type was used as a model for the short-range structure of Zr-rich compositions in $Gd_2(Ti_{1-x}Zr_x)_2O_7$. The weberite-type supplies the positional degrees of freedom of cations needed to capture the additional correlations observed in the PDFs and also provides a model for reconciling the disorder observed at the long-range and short-range scale. The anion Anti-Frenkel defects detected in the average structure lead to the formation of a characteristic local coordination environment. Specifically, layers of AO_8 and BO_6 polyhedra alternate with AO_7 and BO_7 polyehdra, creating a configuration typical of the weberite-type

structure. The weberite-type model will be also tested in the fitting of PDFs of $(Nd_{1-x}Gd_x)_2Zr_2O_7$ compositions in the low-r range. However, the disorder affecting these pyrochlore system when r_A/r_B decreases and approaches the limiting value for the pyrochlore/defect fluorite stability field appears to be more complex than a single phase can describe. Alternatives to this approach might be the big-box modelling of PDF data or models derived from atomistic calculations, as those mentioned in Part 3 and developed by Dr. Davide Ceresoli parallel to the present work.

A separate mention deserves the $Gd_2(Zr_{1-x}Ce_x)_2O_7$ solid solution. Although the Zr^{4+} is substituted with the isovalent Ce^{4+}, the size difference of the two cations results in profound structural changes between the $Gd_2Zr_2O_7$ and $Gd_2Ce_2O_7$ endmembers. At the long-range scale, Zr-rich compositions adopt a pyrochlore structure with a significant concentration of anion Anti-Frenkel and cation antisite defects. In contrast, the majority of samples in the central part of the phase diagram crystallize in a defect fluorite structure, whereas Ce-rich compositions exhibit a C-type ordering. These phase transitions at the average structure are coupled with complex reconstructions at the short-range scale. In this regard, Raman spectra provide clear evidence of the deviation from the average structure, as different vibrational bands attributed to defects appear. Additionally, PDF analysis demonstrates that new metal-metal interatomic distances are generated.

In conclusion, the work conducted in this PhD thesis have confirmed that the structural disorder increases in the $Gd_2(Ti_{1-x}Zr_x)_2O_7$ system with increasing Zr-

content. Despite remaining pyrochlore-like when prepared at 1500 °C, the $Gd_2Zr_2O_7$ composition displays significant deviation from the average structure at the local scale. Its intrinsic capability to reorganize the local coordination environment of cations in response to defects formation allows $Gd_2Zr_2O_7$ to accommodate additional disorder (e.g. when subjected to high radiation doses). Moreover, the introduction of surrogates of radioactive elements (Nd^{3+} and Ce^{4+}) into the structure of $Gd_2Zr_2O_7$ induces other structural changes commensurate with the radii ratio r_A/r_B. Further studies are needed to analyze the behavior of gadolinium zirconate in double doped compositions $(Nd_{1-y}Gd_y)_2(Zr_{1-z}Ce_z)_2O_7$. A major challenge will be that of reconciling the weberite-type, which is the current accepted model for the local structure in disordered fluorite oxides, with the experimental results obtained from these systems. The use of a chemical sensitive probe such as EXAFS will serve as complement to analyze the first atom-atom correlations in more detail. Of particular concern will remain the study of the structural disorder in pyrochlore and defect fluorite oxides as a function not only of composition but also of external conditions (ion irradiation, pressure etc.) and preparation methods (solid-state *vs* sol-gel etc.).

Appendix A

Disposal of radioactive waste

Several human activities produce radioactive wastes, including research, industry, mining operations, medical procedures, nuclear power plants and reprocessing of nuclear weapons[198,199]. The final destiny of radioactive wastes is their disposal, which must be accomplished with utmost consideration according to the fundamental safety objective of protecting people and the environment from the threat posed by ionizing radiation[200,201]. This step is particularly critical, especially for waste that is classified as High-Level Waste (HLW) due to its significant concentration in long-lived radionuclides[202,203]. According to the *Nuclear Safety and Security Glossary* of the International Atomic Energy Agency (IAEA), disposal is defined as the 'emplacement of waste in an appropriate facility without the intention of retrieval'[204]. The accepted method of disposal, which complies with the safety standards, involves burying HLW in geological formations located hundreds of meters below the surface[203]. A multi-barrier approach is employed to prevent the contamination of the biosphere by radionuclides. In this approach, the geological formation serves as the outermost barrier, while the waste form, in which the radionuclides are embedded, acts as the primary barrier[205–207]. The present thesis will focus on the structural study of crystalline phases belonging to the pyrochlore family, which have the potential to serve as waste forms for radionuclides.

Among the aforementioned activities that produce radioactive wastes, the use of nuclear energy to generate electricity and the reprocessing of nuclear weapons stand out as the primary sources of HLW. In terms of nuclear weapons, the production of plutonium for military purposes is currently limited. However, it has been estimated that approximately 300 metric tons of plutonium have been produced globally for the development of warheads, primarily by Russia and the United States[199]. By the present time, thousands of those weapons have been dismantled, resulting in the production of HLW containing tens of metric tonnes of weapons-grade plutonium and hundreds of tons of enriched uranium that require reprocessing[5,208]. On the other hand, nuclear power, along with renewable energy sources, represents a valuable resource for transitioning away from fossil fuels and mitigating the climate crisis. While it does not produce CO_2 as waste, the use of nuclear power for electricity generation results in a kind of high-level waste known as spent nuclear fuel (SNF)[209,210]. Considering a modern light-water reactor with a capacity of 1GW(e), approximately 25 metric tonnes of SNF are generated annually[116,211]. In contrast, generating the same capacity by burning coal produces approximately 6.5 million metric tonnes of CO_2 along with 300,000 tonnes of harmful ashes and thousand tonnes of other gases[212]. According to projections by IAEA, in the best-case scenario, the nuclear generating capacity is expected to double to 792 GW(e) in 2050 from 393 GW(e) in 2021[213]. Even if we consider the present situation, 437 nuclear power reactors are in operation or suspension worldwide, with a total capacity of approximately 390 GW(e). Additionally, there are 57 reactors under construction,

with a combined capacity of approximately 59 GW(e)[214]. This means that approximately 12,000 metric tonnes of SNF are produced every year, which, as HLW, requires proper disposal[116].

At the industrial scale, the method of choice for producing waste forms for HLW is the vitrification process[215–218]. HLW is combined with glass frit and melted at a temperature between 1100-1200 °C. The resulting molten glass is then cast into a metallic canister, which is stored temporarily while awaiting disposal[198,205,219]. Several glass formulations have been developed during the years, comprising borosilicate, aluminosilicate and phosphate glasses[198,205,220]. The radionuclides and other elements present in high-level waste are effectively immobilized by being incorporated into the three-dimensional framework of the glassy matrix. Vitrification of HLW is a consolidated technology, as the glass can be easily prepared. In addition, the amorphous nature of the glass enables the incorporation of a wide range of elements, and its proven radiation resistance and chemical durability make it an ideal waste form[198,205]. However, an alternative option for radionuclides waste forms was envisaged in ceramic materials[221]. Being crystalline phases, they are thermodynamically stable when compared to glasses and can in principle provide superior performances in the immobilization and retention of HLW in geological repositories[205]. In the framework of ceramic materials, Ringwood proposed the SYNROC (SYNthetic ROCk) waste form[222]. This system was based on the combination of titanate minerals such as hollandite ($BaAl_2Ti_5O_{14}$), perovskite

($CaTiO_3$) and zirconolite ($CaZrTi_2O_7$), which can act as host matrices for radionuclides, and rutile (TiO_2) to provide chemical buffering[223]. The idea was to mimic natural mineral phases by utilizing synthetic analogues to encapsulate radioactive elements. Naturally occurring minerals are known to effectively host radionuclides in their crystal structure, remaining stable for millions of years even under harsh conditions[224]. A recent overview of the Synroc technology has been provided by Gregg and colleagues[225].

Different generations of SYNROCs were developed for different waste streams. The one that was tailored for the disposition of SNF and in particular for actinide immobilization, was SYNROC-F, which contained pyrochlore ($CaUTi_2O_7$) as the predominant crystalline phase[226,227]. It should be emphasized at this point that a wide range of chemical elements are produced during nuclear reactions resulting in an extremely complex composition of the waste stream that is the spent nuclear fuel. Several parameters influence the composition of SNF, including the initial composition of the fuel, the extent of fission (referred to as burn-up) and the energy spectrum of neutrons used in the fission process[205,228,229]. Nevertheless, the primary elements contributing to the total radiotoxicity in the time scale of a geological repository are all long-lived actinides such as the isotopes of U (^{235}U with half-life of 0.70 billion years, ^{238}U with half-life of 4.5 billion years) and transuranic elements formed by neutron capture and β-decay, like ^{237}Np (2.1 million years) and ^{239}Pu (24,100 years)[205,209,230]. The solubility of these actinides in the common borosilicate

glasses employed for HLW disposal is generally low[198] and it is highly dependent on the oxidation state[219]. Therefore, there has been growing interest in studying alternative waste forms that can accommodate higher loading of actinides isotopes[231]. It is important to highlight that, currently, no operational facility for Synroc production exists in the world. However, the first treatment facility is under construction at the Australian Nuclear Science Technology Organisation (ANSTO). Although the facility will be focused on ^{99}Mo from nuclear medicine, it will provide the first industrial demonstration of Synroc technology[225]. Additionally, it is noteworthy that glass-ceramic composite materials have been proposed as a means to enhance the properties of nuclear glasses while addressing the challenges posed by complex waste streams[198,205,232].

Pyrochlores for actinides immobilization

Significant effort has been dedicated to exploring pyrochlore compositions that can act as waste forms for actinides. A comprehensive review of this research field can be found in the work of Ewing and colleagues[5], while more recent publications are those of McMaster[210], and Wang[116]. With the general formula $A_2B_2X_6Y$, four crystallographic sites are available to accommodate a vast array of chemical elements in the pyrochlore structure[11,12].

Among the various compositions, titanate pyrochlores attracted much interest for their chemical durability[5]. The first studies were focused on $CaUTi_2O_7$, $CaPuTi_2O_7$

and $Gd_2Ti_2O_7$ compositions[233]. In the host matrix, the presence of Gd, which is a high neutron absorber, is of particular interest, especially for the immobilization of fissile ^{239}Pu and ^{235}U in HLW[230]. However, as already mentioned for glassy matrices, one of the fundamental properties of a potential waste form that needs to be evaluated is radiation resistance[198]. Radioactive elements emit various kinds of radiation, which can result in structural damage to the waste form[216]. The main source of damage in the long term in pyrochlore matrices is the α-decay of actinides and their daughter products[231]. The emission of alpha particles, along with the recoil of the emitting nuclei induces self-heating of the material, ionization, electronic excitations and atomic displacements[5]. The radiation damage has been investigated by studying natural pyrochlores containing U and Th[216,234], or by doping synthetic phases with short-lived isotopes, such as ^{244}Cm (half-life 18 years) or ^{238}Pu (half-life 87 years)[233,235,236]. Another approach consists in simulating the radiation damage induced by α-decay through ion-beam irradiation[5,216,237]. In a systematic study conducted by Lian and coworkres, titanate pyrochlores of the series $A_2Ti_2O_7$ (with A = Sm to Lu, and Y) were irradiated with 1 MeV Kr^+ at different temperatures and characterized by transmission electron microscopy (TEM) and selected-area electron diffraction (SAED)[238]. All the samples were readily amorphized and the ion fluence at which the disordering process occurred (critical amorphization fluence) was determined for each sample and temperature (Figure A1). The ion fluence is often converted into displacement per atom (dpa) units. This conversion enables a straightforward comparison of radiation effects on materials exposed to various types

of radiation[230,239]. It was observed that a significant increase in the critical amorphization fluence occurred at a specific temperature. This temperature value varied depending on the sample and was referred to as the critical amorphization temperature (*Tc*). It represents the temperature at which the rate of amorphization equals the rate of recrystallization, resulting in damage recovery[5]. A high critical *Tc* means that certain materials will be more susceptible to amorphization at low ion fluences. $Gd_2Ti_2O_7$ exhibits the highest of all rare-earth titanate pyrochlores and this is an undesirable outcome since the gadolinium titanate was envisaged for Pu disposition[230].

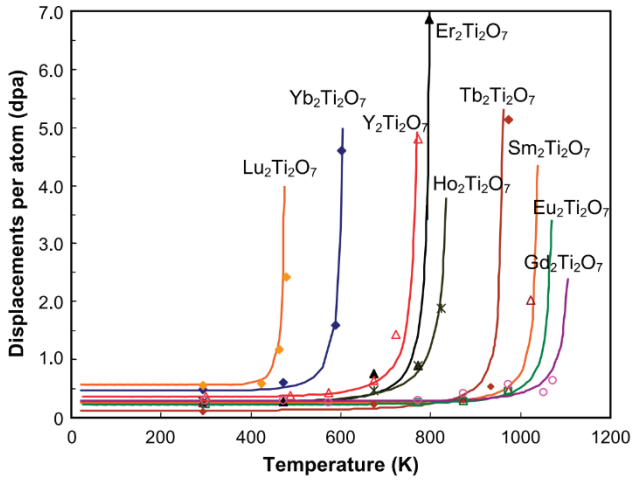

Figure A1 Critical amorphization fluence expressed as displacements per atom (dpa) as a function of temperature [from Ref. 238, 239]

Other compositions were explored. Starting from the $Gd_2Ti_2O_7$ end member, a solid solution with Zr was produced in the form of $Gd_2(Ti_{1-x}Zr_x)_2O_7$ and irradiation with 1

MeV Kr^{+} was employed to investigate the change in radiation resistance with composition[53]. It was found that the critical amorphization temperature dramatically decreased with Zr-substitution. The authors observed that no amorphization occurred for x_{Zr} >0.5 above 380 K and only 30 % of the sample with x_{Zr} = 0.75 was converted to amorphous at cryogenic temperatures. Remarkably, no amorphization occurred for the $Gd_2Zr_2O_7$ end member, even at extremely high ion fluences, corresponding to a radiation dose accumulating over 30 million years in a waste form hosting 10 % wt of ^{239}Pu[53]. The structural transition upon irradiation in $Gd_2(T_{1-x}Zr_x)_2O_7$ samples was followed by Transmission Electron Microscopy (TEM) images and Selected Area Electron Diffraction (SAED) patterns. As shown in Figure A2, the $Gd_2Ti_2O_7$ composition transformed from an ordered pyrochlore structure to a disordered amorphous state. In the case of $Gd_2Zr_2O_7$ the material retained its crystalline nature and converted from the pyrochlore to an anion deficient fluorite (or defect fluorite) structure with general formula $(Gd,Zr)_4O_7$. This phase transition occurs by a complete randomization of cations and anions over their crystallographic sites and can be evidenced from the loss of a specific set of reflections in the diffraction patterns (see Figure A2 lower-right panel).

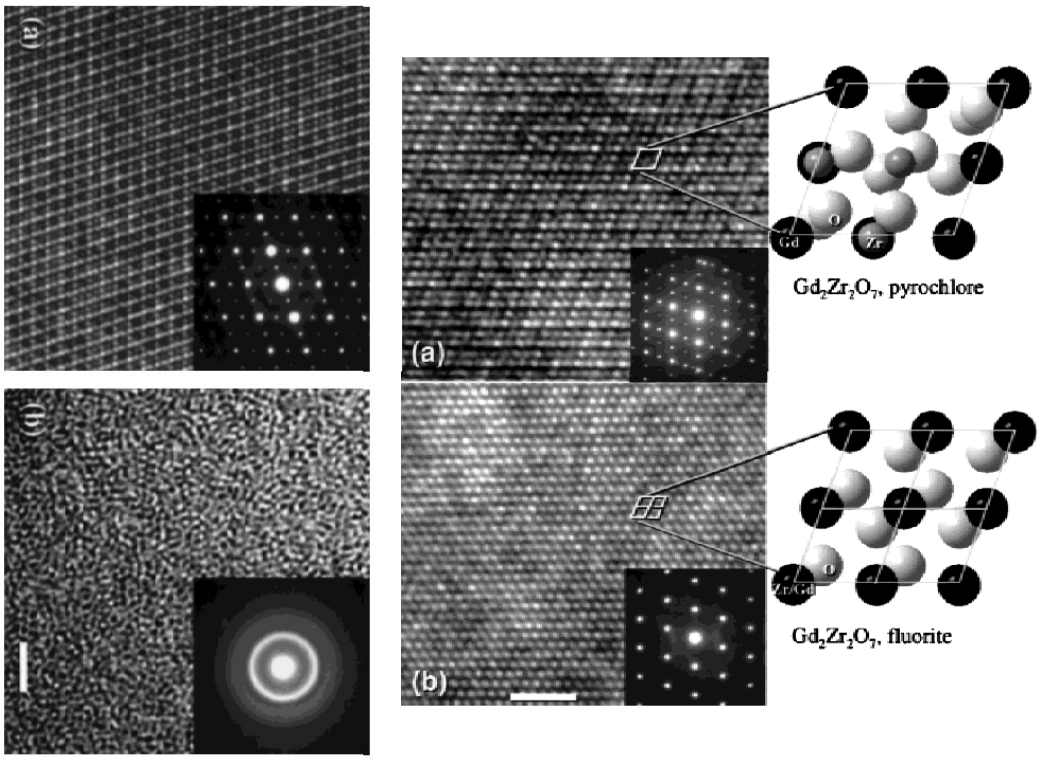

Figure A2 High resolution TEM images and SAED patterns of $Gd_2Ti_2O_7$ (left panels) and $Gd_2Zr_2O_7$ (right panels) compositions before (upper panels) and after (lower panels) irradiation 1 MeV Kr^+ [from Ref. 53].

Since the discovery of radiation resistance in gadolinium zirconate, the response of the $Gd_2(Ti_{1-x}Zr_x)_2O_7$ series towards irradiation has been thoroughly investigated[69–71,82,132,240,241]. Typically, before and after being irradiated, the samples are characterized by means of X-Ray Diffraction (XRD), High Resolution Transmission Electron Microscopy (HRTEM) and Raman spectroscopy to obtain structural information about changes at both the average and the local scale. It is widely recognized that irradiation with heavy ions induces structural disorder in these oxides. In compositions with high Ti-content, the disordering process drives the

structure towards amorphization, whereas in Zr-rich samples the disordering results in a phase transition from the pyrochlore to the defect fluorite structure. These observations clearly indicate that radiation resistance increases with Zr-content in the $Gd_2(Ti_{1-x}Zr_x)_2O_7$ system.

Appendix B

Stability field of the pyrochlore structure

The stability field of pyrochlore oxides was also analyzed with the classical concept of the tolerance factor *t*. Goldschmidt was the first to introduce this concept in 1926 to define the stability of perovskite-like materials[242]. Assuming a hard sphere model packing, the tolerance factor *t* was defined as follows:

$$t = \frac{1}{\sqrt{2}} \frac{r_A + r_O}{r_B + r_O}$$

where r_A, r_B and r_O are the ionic radii of species A, B and O in a perovskite with general formula ABO_3 and $\frac{1}{\sqrt{2}}$ is a geometrical factor derived by the ratio between the B-O bond length (half of the lattice constant) and A-O bond length (half of the face diagonal). As *t* tends to unity, the perovskite structure generated by a specific combination of A and B-cations becomes stable. In 1958, Isupov[243] proposed a similar tolerance factor also for pyrochlore oxides in the assumption of a regular BO_6 octahedral network. The tolerance factor has the form of

$$t = 0.866 \frac{r_A + r_O}{r_B + r_O}$$

where 0.866 is the ratio between A-O1 and A-O2 bond lengths. However, as it was stated above in the definition of *x*O1, the coordination environment of B-cations is usually a trigonal antiprism rather than a perfect octahedron. Cai and coworkers

revisited the tolerance factor for pyrochlore oxides in 2011[244]. Starting from the coordination geometry of O1 and O2 ions in A_2B_2 and A_4 tetrahedra, they derived two tolerance factors, t_1 and t_2, integrating the *x*O1 parameter and cell constant in their formulation. t_1 and t_2 are defined as follows:

$$t_1 = \frac{\sqrt{\left(X - \frac{1}{4}\right)^2 + \frac{1}{32}}}{\sqrt{\left(X - \frac{1}{2}\right)^2 + \frac{1}{32}}} \frac{r_A + r_O}{r_B + r_O}$$

$$t_2 = a \frac{3\sqrt{3}}{8(r_A + r_O)}$$

where X is *x*O1 and a is the cell constant. When investigating 315 pyrochlore compositions, Cai and colleagues found that t_1 values lie between 0.83 and 1.07, with the majority being between 0.90 and 0.99. For t_2, the values are in the range 0.89-0.93. These tolerance factors rely on the determination or calculation of either the *x*O1 parameter or the cell constant. To overcome this limitation, Mouta et al. proposed a new tolerance factor based solely on the ionic radii of A, B and O ions[245]. They started from the definition of t_2 by Cai and colleagues and substituted in its expression an empirical formula for predicting the cell constant of the pyrochlore structure from r_A, r_B and r_O. In this way they obtained the following new tolerance factor:

$$t_{new} = 1.43373 - 0.42931 \frac{r_A + r_O}{r_B + r_O}$$

The distribution of pyrochlore compositions according to the analysis of Mouta and coworkers is centered at t_{new} = 0.913. More recently, an additional tolerance factor τ has been formulated by Song and colleagues[246].

$$\tau = \frac{3(r_A + r_O)}{\sqrt{17}(r_B + r_O)}$$

Similar to Isupov, the derivation of τ was based on a description of the pyrochlore structure with regular BO_6 octahedra. The investigated pyrochlore compositions fell into a range of τ-values of 0.826-0.943.

In their review of tolerance factors for the definition of a pyrochlore stability field, Fuentes and co-workers stressed the necessity to use the actual metal distribution of cations at the A- and B-site of the pyrochlore structure when calculating the ratio r_A/r_B or other tolerance factors[182]. In fact, as cations become similar in size, $A_2B_2O_7$ pyrochlores are affected by cation antisite defects, which results in a certain degree of inversion of the occupancies of A- and B-sites and a change in the corresponding radii. Fuentes and colleagues studied the $Gd_{2-x}Ln_xZr_2O_7$ series, in which a pyrochlore to defect fluorite phase transition occurs when introducing lanthanides smaller than Gd^{3+}. Plotting the variation of the tolerance factors presented above in the $Gd_{2-x}Ln_xZr_2O_7$ series, Fuentes and colleagues obtained a straight line when using the nominal occupancies of cation sites. If the actual occupancies derived by Rietveld refinements of diffraction patterns are used instead, a clear transition in tolerance factors is observed at the pyrochlore/defect fluorite border. Moreover, Fuentes and

co-workers clearly stated that none of the existing criteria provide a simple and efficient method for predicting whether a hypothetical $A_2B_2O_7$ compound would crystallize in the pyrochlore or defect fluorite structure. In this regard, the radii ratio r_A/r_B remains the most simple and useful criterion, because it implicitly contains the information about the tendency of possible A- and B-cations to order. Fuentes concluded by saying that since pyrochlore oxides are prone to disorder, it is not possible to formulate a tolerance factor as meaningful as that introduced by Goldschmidt for perovskites[182].

It is worth mentioning that in 2021 O'Quinn and co-workers defined the stability field of fluorite and defect fluorite structures by introducing the parameters ρ_c and ρ_a[9]. These parameters measure the relative size of a given cation to all other cations (ρ_c) and the relative size of the cations to the anions (ρ_a) in the structure. A phase space for fluorite-type structures is delimited by ρ_c and ρ_a, with $\rho_c > 0.931$ and ρ_a in the range 0.657-0.756. The rules introduced by O'Quinn and co-workers are regarded as the application of Pauling's rules on coordination polyhedra[247,248] and Goldschmidt's rules on cation mixing[242] in ionic solids.

References

(1) Yakubovich, O.; Urusov, V.; Massa, W.; Frenzen, G.; Babel, D. Structure of Na2Fe2F7 and Structural Relations in the Family of Weberites Na2MIIMIIIF7. *Zeitschrift fur Anorg. und Allg. Chemie* **1993**, *619* (11), 1909–1919. https://doi.org/10.1002/zaac.19936191115.

(2) Sickafus, K. E.; Grimes, R. W.; Valdez, J. A.; Cleave, A.; Tang, M.; Ishimaru, M.; Corish, S. M.; Stanek, C. R.; Uberuaga, B. P. Radiation-Induced Amorphization Resistance and Radiation Tolerance in Structurally Related Oxides. *Nat. Mater.* **2007**, *6* (3), 217–223. https://doi.org/10.1038/nmat1842.

(3) Stanek, C. R.; Jiang, C.; Uberuaga, B. P.; Sickafus, K. E.; Cleave, A. R.; Grimes, R. W. Predicted Structure and Stability of A4B3O12 δ-Phase Compositions. *Phys. Rev. B* **2009**, *80* (17), 174101. https://doi.org/10.1103/PhysRevB.80.174101.

(4) Karimova, O. V.; Organova, N. I.; Balakirev, V. G. Modulation in the Murataite Structure. *Crystallogr. Reports* **2002**, *47* (6), 957–960. https://doi.org/10.1134/1.1523540.

(5) Ewing, R. C.; Weber, W. J.; Lian, J. Nuclear Waste Disposal—Pyrochlore (A2B2O7): Nuclear Waste Form for the Immobilization of Plutonium and "Minor" Actinides. *J. Appl. Phys.* **2004**, *95* (11), 5949–5971. https://doi.org/10.1063/1.1707213.

(6) Toon, R. The Discovery of Fluorine. *Education in Chemistry*. September 1, **2011**.

(7) Willoughby, E. Making Light of Fluorite. *Nat. Geosci.* **2022**, *15* (10), 760–760. https://doi.org/10.1038/s41561-022-01040-y.

(8) Barker, W. W. Stoichiometry, Cation Coordination Number and a Method of Representation of Oxide Compounds and Phases Related to the Fluorite Structure. *Zeitschrift für Krist.* **1969**, *128* (1–2), 55–65. https://doi.org/10.1524/zkri.1969.128.1-2.55.

(9) O'Quinn, E. C.; Drey, D. L.; Lang, M. K. Defining the Structural Stability Field of Disordered Fluorite Oxides. *Front. Chem.* **2021**, *9* (August), 1–9. https://doi.org/10.3389/fchem.2021.733718.

(10) Wöhler, F. Ueber Den Pyrochlor, Eine Neue Mineralspecies. *Ann. Phys.* **1826**, *83* (8), 417–428. https://doi.org/10.1002/andp.18260830803.

(11) Subramanian, M. A.; Aravamudan, G.; Subba Rao, G. V. Oxide Pyrochlores — A Review. *Prog. Solid State Chem.* **1983**, *15* (2), 55–143. https://doi.org/10.1016/0079-6786(83)90001-8.

(12) Atencio, D.; Andrade, M. B.; Christy, A. G.; Giere, R.; Kartashov, P. M. THE PYROCHLORE SUPERGROUP OF MINERALS: NOMENCLATURE. *Can. Mineral.* **2010**, *48* (3), 673–698. https://doi.org/10.3749/canmin.48.3.673.

(13) Chakoumakos, B. C.; Ewing, R. C. Crystal Chemical Constraints on the Formation of Actinide Pyrochlores. *MRS Proc.* **1984**, *44*, 641. https://doi.org/10.1557/PROC-44-641.

(14) Weller, M. T.; Hughes, R. W.; Rooke, J.; Knee, C. S.; Reading, J. The Pyrochlore Family - A Potential Panacea for the Frustrated Perovskite Chemist. *Dalt. Trans.* **2004**, No. 19, 3032–3041. https://doi.org/10.1039/b401787k.

(15) Harvey, E. J.; Ashbrook, S. E.; Lumpkin, G. R.; Redfern, S. A. T. Characterisation of the (Y 1−x La x) 2 Ti 2 O 7 System by Powder Diffraction and Nuclear Magnetic Resonance Methods. *J. Mater. Chem.* **2006**, *16* (48), 4665–4674. https://doi.org/10.1039/B608053G.

(16) Herrera, G.; Jiménez-Mier, J.; Chavira, E. Layered-Structural Monoclinic–Orthorhombic Perovskite La2Ti2O7 to Orthorhombic LaTiO3 Phase Transition and Their Microstructure Characterization. *Mater. Charact.* **2014**, *89*, 13–22. https://doi.org/10.1016/j.matchar.2013.12.013.

(17) Chakraborty, K. R.; Krishna, P. S. R.; Chavan, S. V; Tyagi, A. K. A Neutron Diffraction Study on Ceria-Neodia Solid Solutions. *Powder Diffr.* **2006**, *21* (1), 36–39. https://doi.org/10.1154/1.2104547.

(18) Chavan, S. V.; Tyagi, A. K. Phase Relations and Lattice Thermal Expansion Studies in the Ce0.50RE0.50O1.75 (RE=rare-Earths). *Mater. Sci. Eng. A* **2005**, *404* (1–2), 57–63. https://doi.org/10.1016/j.msea.2005.05.036.

(19) Coduri, M.; Scavini, M.; Allieta, M.; Brunelli, M.; Ferrero, C. Defect Structure of Y-Doped Ceria on Different Length Scales. *Chem. Mater.* **2013**, *25* (21), 4278–4289. https://doi.org/10.1021/cm402359d.

(20) Coduri, M.; Bozzetti, D.; Checchia, S.; Brunelli, M.; Scavini, M. Local and Average Structure of Yb-Doped Ceria through Synchrotron and Neutron Pair Distribution Function. *Inorganics* **2019**, *7* (8), 102. https://doi.org/10.3390/inorganics7080102.

(21) Chakoumakos, B. C. Systematics of the Pyrochlore Structure Type, Ideal A2B2X6Y. *J. Solid State Chem.* **1984**, *53* (1), 120–129. https://doi.org/10.1016/0022-4596(84)90234-2.

(22) Glerup, M.; Nielsen, O. F.; Poulsen, F. W. The Structural Transformation from the Pyrochlore Structure, A2B2O7, to the Fluorite Structure, AO2, Studied by Raman Spectroscopy and Defect Chemistry Modeling. *J. Solid State Chem.* **2001**, *160* (1), 25–32. https://doi.org/10.1006/jssc.2000.9142.

(23) Cai, L.; Nino, J. C. Complex Ceramic Structures. I. Weberites. *Acta Crystallogr. Sect. B Struct. Sci.* **2009**, *65* (3), 269–290. https://doi.org/10.1107/S0108768109011355.

(24) O'Quinn, E. C.; Sickafus, K. E.; Ewing, R. C.; Baldinozzi, G.; Neuefeind, J. C.; Tucker, M. G.; Fuentes, A. F.; Drey, D.; Lang, M. K. Predicting Short-Range Order and Correlated Phenomena in Disordered Crystalline Materials. *Sci. Adv.* **2020**, *6*

(35), eabc2758. https://doi.org/10.1126/sciadv.abc2758.

(25) Wuensch, B. J.; Eberman, K. W.; Heremans, C.; Ku, E. M.; Onnerud, P.; Yeo, E. M. E.; Haile, S. M.; Stalick, J. K.; Jorgensen, J. D. Connection between Oxygen-Ion Conductivity of Pyrochlore Fuel-Cell Materials and Structural Change with Composition and Temperature. *Solid State Ionics* **2000**, *129* (1), 111–133. https://doi.org/10.1016/S0167-2738(99)00320-3.

(26) Bøgvad, R. Weberite, a New Mineral from Ivigtut. *Meddelelser om Grønl.* **1938**, *119*, 3–11.

(27) Rooksby, H. P.; White, E. A. D. Rare-Earth Niobates and TantaIates of Defect Fluorite- and Weberite-Type Structures. *J. Am. Ceram. Soc.* **1964**, *47* (2), 94–96. https://doi.org/10.1111/j.1151-2916.1964.tb15663.x.

(28) Allpress, J. G.; Rossell, H. J. Fluorite-Related Phases Ln3MO7, Ln = Rare Earth, Y, or Sc, M = Nb, Sb, or Ta. I. Crystal Chemistry. *J. Solid State Chem.* **1979**, *27* (1), 105–114. https://doi.org/10.1016/0022-4596(79)90149-X.

(29) Kahn-Harari, A.; Mazerolles, L.; Michel, D.; Robert, F. Structural Description of La3NbO7. *J. Solid State Chem.* **1995**, *116* (1), 103–106. https://doi.org/10.1006/jssc.1995.1189.

(30) Shamblin, J.; Feygenson, M.; Neuefeind, J.; Tracy, C. L.; Zhang, F.; Finkeldei, S.; Bosbach, D.; Zhou, H.; Ewing, R. C.; Lang, M. Probing Disorder in Isometric Pyrochlore and Related Complex Oxides. *Nat. Mater.* **2016**, *15* (5), 507–511. https://doi.org/10.1038/nmat4581.

(31) Drey, D. L.; O'Quinn, E. C.; Subramani, T.; Lilova, K.; Baldinozzi, G.; Gussev, I. M.; Fuentes, A. F.; Neuefeind, J. C.; Everett, M.; Sprouster, D.; et al. Disorder in Ho 2 Ti 2−x Zr x O 7 : Pyrochlore to Defect Fluorite Solid Solution Series. *RSC Adv.* **2020**, *10* (57), 34632–34650. https://doi.org/10.1039/D0RA07118H.

(32) King, G.; Thompson, C. M.; Greedan, J. E.; Llobet, A. Local Structure of the Vacancy Disordered Fluorite Yb3TaO 7 from Neutron Total Scattering. *J. Mater. Chem. A* **2013**, *1* (35), 10487–10494. https://doi.org/10.1039/c3ta12100c.

(33) Penfield, S. L.; Foote, H. W. On Bixbyite, a New Mineral, and Notes on the Associated Topaz. *Am. J. Sci.* **1897**, *4*, 105–108.

(34) Adachi, G.; Imanaka, N. The Binary Rare Earth Oxides. *Chem. Rev.* **1998**, *98* (4), 1479–1514. https://doi.org/10.1021/cr940055h.

(35) Grover, V.; Achary, S. N.; Tyagi, A. K. Structural Analysis of Excess-Anion C-Type Rare Earth Oxide: A Case Study with Gd 1− x Ce x O 1.5+ x /2 (x = 0.20 and 0.40). *J. Appl. Crystallogr.* **2003**, *36* (4), 1082–1084. https://doi.org/10.1107/S0021889803010288.

(36) Grover, V.; Tyagi, A. K. Phase Relation Studies in the CeO 2-Gd 2O 3-ZrO 2 System. *J. Solid State Chem.* **2004**, *177* (11), 4197–4204. https://doi.org/10.1016/j.jssc.2004.07.052.

(37) Scavini, M.; Coduri, M.; Allieta, M.; Masala, P.; Cappelli, S.; Oliva, C.; Brunelli, M.; Orsini, F.; Ferrero, C. Percolating Hierarchical Defect Structures Drive Phase Transformation in Ce 1− x Gd x O 2− x /2 : A Total Scattering Study. *IUCrJ* **2015**, *2* (5), 511–522. https://doi.org/10.1107/S2052252515011641.

(38) Horlait, D.; Claparède, L.; Clavier, N.; Szenknect, S.; Dacheux, N.; Ravaux, J.; Podor, R. Stability and Structural Evolution of Ce IV 1– x Ln III x O 2– x /2 Solid Solutions: A Coupled μ-Raman/XRD Approach. *Inorg. Chem.* **2011**, *50* (15), 7150–7161. https://doi.org/10.1021/ic200751m.

(39) Reid, D. P.; Stennett, M. C.; Hyatt, N. C. The Fluorite Related Modulated Structures of the Gd2(Zr2−xCex)O7 Solid Solution: An Analogue for Pu Disposition. *J. Solid State Chem.* **2012**, *191*, 2–9. https://doi.org/10.1016/j.jssc.2011.12.039.

(40) Scavini, M.; Coduri, M.; Allieta, M.; Brunelli, M.; Ferrero, C. Probing Complex Disorder in Ce 1- x Gd x O 2- x /2 Using the Pair Distribution Function Analysis. *Chem. Mater.* **2012**, *24* (7), 1338–1345. https://doi.org/10.1021/cm203819u.

(41) Henderson, S. J.; Shebanova, O.; Hector, A. L.; McMillan, P. F.; Weller, M. T. Structural Variations in Pyrochlore-Structured Bi 2 Hf 2 O 7 , Bi 2 Ti 2 O 7 and Bi 2 Hf 2 - x Ti x O 7 Solid Solutions as a Function of Composition and Temperature by Neutron and X-Ray Diffraction and Raman Spectroscopy. *Chem. Mater.* **2007**, *19* (7), 1712–1722. https://doi.org/10.1021/cm062864a.

(42) Minervini, L.; Grimes, R. W.; Sickafus, K. E. Disorder in Pyrochlore Oxides. *J. Am. Ceram. Soc.* **2000**, *83* (8), 1873–1878. https://doi.org/10.1111/j.1151-2916.2000.tb01484.x.

(43) van Dijk, M. P.; Burggraaf, A. J.; Cormack, A. N.; Catlow, C. R. A. Defect Structures and Migration Mechanisms in Oxide Pyrochlores. *Solid State Ionics* **1985**, *17* (2), 159–167. https://doi.org/10.1016/0167-2738(85)90067-0.

(44) Pirzada, M.; Grimes, R. W.; Minervini, L.; Maguire, J. F.; Sickafus, K. E. Oxygen Migration in A2B2O7 Pyrochlores. *Solid State Ionics* **2001**, *140* (3–4), 201–208. https://doi.org/10.1016/S0167-2738(00)00836-5.

(45) Sun, M.; Huang, B. “Energy Selection Channels” for High-Performance Electrolyte: Anion-Frenkel Defect Pair as Dominant Source for O Ion Conductions in Pyrochlore-Type Lanthanide Hafnium Oxides SOFC. *Inorg. Chem.* **2017**, *56* (14), 7975–7984. https://doi.org/10.1021/acs.inorgchem.7b00683.

(46) Minervini, L.; Grimes, R. W.; Tabira, Y.; Withers, R. L.; Sickafus, K. E. The Oxygen Positional Parameter in Pyrochlores and Its Dependence on Disorder. *Philos. Mag. A* **2002**, *82* (1), 123–135. https://doi.org/10.1080/01418610208240001.

(47) Heremans, C.; Wuensch, B. J.; Stalick, J. K.; Prince, E. Fast-Ion Conducting Y2(Zr Ti1-)2O7 Pyrochlores: Neutron Rietveld Analysis of Disorder Induced by Zr Substitution. *J. Solid State Chem.* **1995**, *117* (1), 108–121.

https://doi.org/10.1006/jssc.1995.1253.

(48) Mandal, B. P.; Banerji, A.; Sathe, V.; Deb, S. K.; Tyagi, A. K. Order–Disorder Transition in Nd2−yGdyZr2O7 Pyrochlore Solid Solution: An X-Ray Diffraction and Raman Spectroscopic Study. *J. Solid State Chem.* **2007**, *180* (10), 2643–2648. https://doi.org/10.1016/j.jssc.2007.07.007.

(49) Sayed, F. N.; Jain, D.; Mandal, B. P.; Pillai, C. G. S.; Tyagi, A. K. Tunability of Structure from Ordered to Disordered and Its Impact on Ionic Conductivity Behavior in the Nd2−yHoyZr2O7 ($0.0 \leq y \leq 2.0$) System. *RSC Adv.* **2012**, *2* (22), 8341. https://doi.org/10.1039/c2ra20458d.

(50) Lian, J.; Wang, L.; Chen, J.; Sun, K.; Ewing, R. C.; Farmer, J. M.; Boatner, L. A. The Order-Disorder Transition in Ion-Irradiated Pyrochlore. *Acta Mater.* **2003**, *51* (5), 1493–1502. https://doi.org/10.1016/S1359-6454(02)00544-X.

(51) Sickafus, K. E.; Minervini, L.; Grimes, R. W.; Valdez, J. A.; Ishimaru, M.; Li, F.; McClellan, K. J.; Hartmann, T. Radiation Tolerance of Complex Oxides. *Science (80-.).* **2000**, *289* (5480), 748–751. https://doi.org/10.1126/science.289.5480.748.

(52) Knop, O.; Brisse, F.; Castelliz, L. Pyrochlores. V. Thermoanalytic, X-Ray, Neutron, Infrared, and Dielectric Studies of A 2 Ti 2 O 7 Titanates. *Can. J. Chem.* **1969**, *47* (6), 971–990. https://doi.org/10.1139/v69-155.

(53) Wang, S. X.; Begg, B. D.; Wang, L. M.; Ewing, R. C.; Weber, W. J.; Kutty, K. V. G. Radiation Stability of Gadolinium Zirconate: A Waste Form for Plutonium Disposition. *J. Mater. Res.* **1999**, *14* (12), 4470–4473. https://doi.org/10.1557/JMR.1999.0606.

(54) Shannon, R. D. Revised Effective Ionic Radii and Systematic Studies of Interatomic Distances in Halides and Chalcogenides. *Acta Crystallogr. Sect. A* **1976**, *32* (5), 751–767. https://doi.org/10.1107/S0567739476001551.

(55) Moon, P. K.; Tuller, H. L. Intrinsic Fast Oxygen Ionic Conductivity in the Gd2(ZrxTi1−x)2O7, and Y2(ZrxTi1-x)2O7 Pyrochlore Systems. *MRS Proc.* **1988**, *135* (1), 149. https://doi.org/10.1557/PROC-135-149.

(56) Moon, P. K.; Tuller, H. L. Ionic Conduction in the Gd2Ti2O7−Gd2Zr2O7 System. *Solid State Ionics* **1988**, *28–30*, 470–474. https://doi.org/10.1016/S0167-2738(88)80085-7.

(57) Moon, P. K.; Tuller, H. L. Fast Ion Conduction in the Gd2(ZrxTi1−x)2O7 Pyrochlore System; Tuller, H. L., Balkanski, M., Eds.; Springer US: Boston, MA, 1989; pp 307–312. https://doi.org/10.1007/978-1-4613-0509-5_14.

(58) Tuller, H. L. Mixed Ionic-Electronic Conduction in a Number of Fluorite and Pyrochlore Compounds. *Solid State Ionics* **1992**, *52* (1–3), 135–146. https://doi.org/10.1016/0167-2738(92)90099-B.

(59) Tuller, H. L. Oxygen Ion Conduction and Structural Disorder in Conductive Oxides. *J. Phys. Chem. Solids* **1994**, *55* (12), 1393–1404.

https://doi.org/10.1016/0022-3697(94)90566-5.

(60) Williford, R. E.; Weber, W. J.; Devanathan, R.; Gale, J. D. Effects of Cation Disorder on Oxygen Vacancy Migration in Gd2Ti2O7. *J. Electroceramics* **1999**, *3* (4), 409–424. https://doi.org/10.1023/A:1009978200528.

(61) van Dijk, M. .; de Vries, K. .; Burggraaf, A. . Oxygen Ion and Mixed Conductivity in Compounds with the Fluorite and Pyrochlore Structure. *Solid State Ionics* **1983**, *9–10*, 913–919. https://doi.org/10.1016/0167-2738(83)90110-8.

(62) Díaz-Guillén, J. A.; Díaz-Guillén, M. R.; Almanza, J. M.; Fuentes, A. F.; Santamaría, J.; León, C. Effect of La Substitution for Gd in the Ionic Conductivity and Oxygen Dynamics of Fluorite-Type Gd2Zr2 O7. *J. Phys. Condens. Matter* **2007**, *19* (35), 356212. https://doi.org/10.1088/0953-8984/19/35/356212.

(63) Li, F.; Zhou, L.; Liu, J.-X.; Liang, Y.; Zhang, G.-J. High-Entropy Pyrochlores with Low Thermal Conductivity for Thermal Barrier Coating Materials. *J. Adv. Ceram.* **2019**, *8* (4), 576–582. https://doi.org/10.1007/s40145-019-0342-4.

(64) Wright, A. J.; Wang, Q.; Ko, S.-T.; Chung, K. M.; Chen, R.; Luo, J. Size Disorder as a Descriptor for Predicting Reduced Thermal Conductivity in Medium- and High-Entropy Pyrochlore Oxides. *Scr. Mater.* **2020**, *181*, 76–81. https://doi.org/10.1016/j.scriptamat.2020.02.011.

(65) Wu, J.; Wei, X.; Padture, N. P.; Klemens, P. G.; Gell, M.; García, E.; Miranzo, P.; Osendi, M. I. Low-Thermal-Conductivity Rare-Earth Zirconates for Potential Thermal-Barrier-Coating Applications. *J. Am. Ceram. Soc.* **2002**, *85* (12), 3031–3035. https://doi.org/https://doi.org/10.1111/j.1151-2916.2002.tb00574.x.

(66) Díaz-Guillén, J. A.; Durá, O. J.; Díaz-Guillén, M. R.; Bauer, E.; López de la Torre, M. A.; Fuentes, A. F. Thermophysical Properties of Gd2Zr2O7 Powders Prepared by Mechanical Milling: Effect of Homovalent Gd3+ Substitution. *J. Alloys Compd.* **2015**, *649*, 1145–1150. https://doi.org/10.1016/j.jallcom.2015.07.146.

(67) Nicholls, J. R.; Lawson, K. J.; Johnstone, A.; Rickerby, D. S. Methods to Reduce the Thermal Conductivity of EB-PVD TBCs. *Surf. Coatings Technol.* **2002**, *151–152*, 383–391. https://doi.org/10.1016/S0257-8972(01)01651-6.

(68) Zhao, M.; Pan, W.; Wan, C.; Qu, Z.; Li, Z.; Yang, J. Defect Engineering in Development of Low Thermal Conductivity Materials: A Review. *J. Eur. Ceram. Soc.* **2017**, *37* (1), 1–13. https://doi.org/10.1016/j.jeurceramsoc.2016.07.036.

(69) Begg, B. D.; Hess, N. J.; McCready, D. E.; Thevuthasan, S.; Weber, W. J. Heavy-Ion Irradiation Effects in Gd2(Ti2-XZrx)O7 Pyrochlores. *J. Nucl. Mater.* **2001**, *289* (1–2), 188–193. https://doi.org/10.1016/S0022-3115(00)00696-6.

(70) Hess, N. J.; Begg, B. D.; Conradson, S. D.; McCready, D. E.; Gassman, P. L.; Weber, W. J. Spectroscopic Investigations of the Structural Phase Transition in Gd2(Ti1-YZry)2O7 Pyrochlores. *J. Phys. Chem. B* **2002**, *106* (18), 4663–4677. https://doi.org/10.1021/jp014285t.

(71) Lang, M.; Zhang, F. X.; Ewing, R. C.; Lian, J.; Trautmann, C.; Wang, Z. Structural Modifications of Gd 2Zr 2-XTi XO 7 Pyrochlore Induced by Swift Heavy Ions: Disordering and Amorphization. *J. Mater. Res.* **2009**, *24* (4), 1322–1334. https://doi.org/10.1557/jmr.2009.0151.

(72) Blanchard, P. E. R.; Clements, R.; Kennedy, B. J.; Ling, C. D.; Reynolds, E.; Avdeev, M.; Stampfl, A. P. J.; Zhang, Z.; Jang, L.-Y. Does Local Disorder Occur in the Pyrochlore Zirconates? *Inorg. Chem.* **2012**, *51* (24), 13237–13244. https://doi.org/10.1021/ic301677b.

(73) Norberg, S. T.; Hull, S.; Eriksson, S. G.; Ahmed, I.; Kinyanjui, F.; Biendicho, J. J. Pyrochlore to Fluorite Transition: The Y 2 (Ti 1– x Zr x) 2 O 7 ($0.0 \leq x \leq 1.0$) System. *Chem. Mater.* **2012**, *24* (22), 4294–4300. https://doi.org/10.1021/cm301649d.

(74) Zhang, Z.; Middleburgh, S. C.; de los Reyes, M.; Lumpkin, G. R.; Kennedy, B. J.; Blanchard, P. E. R.; Reynolds, E.; Jang, L.-Y. Gradual Structural Evolution from Pyrochlore to Defect-Fluorite in Y 2 Sn 2– x Zr x O 7 : Average vs Local Structure. *J. Phys. Chem. C* **2013**, *117* (50), 26740–26749. https://doi.org/10.1021/jp408682r.

(75) de los Reyes, M.; Whittle, K. R.; Zhang, Z.; Ashbrook, S. E.; Mitchell, M. R.; Jang, L.-Y.; Lumpkin, G. R. The Pyrochlore to Defect Fluorite Phase Transition in Y2Sn2−xZrxO7. *RSC Adv.* **2013**, *3* (15), 5090. https://doi.org/10.1039/c3ra22704a.

(76) Zhang, Z.; Avdeev, M.; de los Reyes, M.; Lumpkin, G. R.; Kennedy, B. J.; Blanchard, P. E. R.; Liu, S.; Tadich, A.; Cowie, B. C. C. Probing Long- and Short-Range Disorder in Y 2 Ti 2– x Hf x O 7 by Diffraction and Spectroscopy Techniques. *J. Phys. Chem. C* **2016**, *120* (46), 26465–26479. https://doi.org/10.1021/acs.jpcc.6b07076.

(77) Reynolds, E.; Blanchard, P. E. R.; Kennedy, B. J.; Ling, C. D.; Liu, S.; Avdeev, M.; Zhang, Z.; Cuello, G. J.; Tadich, A.; Jang, L.-Y. Anion Disorder in Lanthanoid Zirconates Gd 2– x Tb x Zr 2 O 7. *Inorg. Chem.* **2013**, *52* (15), 8409–8415. https://doi.org/10.1021/ic4009703.

(78) Su, S.; Ding, Y.; Shu, X.; Dan, H.; Tu, H.; Dong, F.; Lu, X. Nd and Ce Simultaneous Substitution Driven Structure Modifications in Gd2−xNdxZr2−yCeyO7. *J. Eur. Ceram. Soc.* **2015**, *35* (6), 1847–1853. https://doi.org/10.1016/j.jeurceramsoc.2014.12.017.

(79) Shu, X.; Fan, L.; Lu, X.; Xie, Y.; Ding, Y. Structure and Performance Evolution of the System (Gd1−Nd)2(Zr1−Ce)2O7 ($0 \leq x$, $Y \leq 1.0$). *J. Eur. Ceram. Soc.* **2015**, *35* (11), 3095–3102. https://doi.org/10.1016/j.jeurceramsoc.2015.04.037.

(80) Feighery, A. J.; Irvine, J. T. S.; Zheng, C. Phase Relations at 1500°C in the Ternary System ZrO2–Gd2O3–TiO2. *J. Solid State Chem.* **2001**, *160* (2), 302–306. https://doi.org/10.1006/jssc.2001.9201.

(81) Wang, C.; Zinkevich, M.; Aldinger, F. Phase Diagrams and Thermodynamics of Rare-Earth-Doped Zirconia Ceramics. *Pure Appl. Chem.* **2007**, *79* (10), 1731–1753.

https://doi.org/10.1351/pac200779101731.

(82) Sattonnay, G.; Moll, S.; Thomé, L.; Decorse, C.; Legros, C.; Simon, P.; Jagielski, J.; Jozwik, I.; Monnet, I. Phase Transformations Induced by High Electronic Excitation in Ion-Irradiated Gd2(ZrxTi1−x)2O7 Pyrochlores. *J. Appl. Phys.* **2010**, *108* (10), 103512. https://doi.org/10.1063/1.3503452.

(83) Michel, D.; Perez y Jorba, M.; Collongues, R. Etude de La Transformation Ordre-Desordre de La Structure Fluorite a La Structure Pyrochlore Pour Des Phases (1−x) ZrO2 □ x Ln2O3. *Mater. Res. Bull.* **1974**, *9* (11), 1457–1468. https://doi.org/10.1016/0025-5408(74)90092-0.

(84) Shi, J. L.; Qu, Z. X.; Wang, Q. Influence of Temperature on the Order-Disorder Transition in $Gd_2Zr_2O_7$. *Key Eng. Mater.* **2016**, *697*, 386–389. https://doi.org/10.4028/www.scientific.net/KEM.697.386.

(85) Fitch, A.; Dejoie, C.; Covacci, E.; Confalonieri, G.; Grendal, O.; Claustre, L.; Guillou, P.; Kieffer, J.; de Nolf, W.; Petitdemange, S.; et al. ID22 – the High-Resolution Powder-Diffraction Beamline at ESRF. *J. Synchrotron Radiat.* **2023**, *30* (5), 1–10. https://doi.org/10.1107/S1600577523004915.

(86) Dejoie, C.; Coduri, M.; Petitdemange, S.; Giacobbe, C.; Covacci, E.; Grimaldi, O.; Autran, P.-O.; Mogodi, M. W.; Šišak Jung, D.; Fitch, A. N. Combining a Nine-Crystal Multi-Analyser Stage with a Two-Dimensional Detector for High-Resolution Powder X-Ray Diffraction. *J. Appl. Crystallogr.* **2018**, *51* (6), 1721–1733. https://doi.org/10.1107/S1600576718014589.

(87) di Biase, A.; Castellano, C.; Scavini, M.; Confalonieri, G. Experiment Ch-5900 at ID22 Beamline, ESRF, Grenoble (FR). 2021. https://doi.org/doi.org/10.15151/ESRF-ES-404435446.

(88) di Biase, A.; Fortis, A.; Ceresoli, D.; Scavini, M.; Confalonieri, G. Experiment Ch-6218 at ID22 Beamline, ESRF, Grenoble (FR). 2022. https://doi.org/doi.org/10.15151/ESRF-ES-804827098.

(89) Rietveld, H. M. A Profile Refinement Method for Nuclear and Magnetic Structures. *J. Appl. Crystallogr.* **1969**, *2* (2), 65–71. https://doi.org/10.1107/S0021889869006558.

(90) Larson, A. C.; Von Dreele, R. B. GSAS: General Structure Analysis System LANSCE, MS-H805. *Los Alamos, NM* **1994**, *87545*, 178.

(91) Toby, B. H. EXPGUI, a Graphical User Interface for GSAS. *J. Appl. Crystallogr.* **2001**, *34* (2), 210–213. https://doi.org/10.1107/S0021889801002242.

(92) Hammersley, A. P. FIT2D: A Multi-Purpose Data Reduction, Analysis and Visualization Program. *J. Appl. Crystallogr.* **2016**, *49*, 646–652. https://doi.org/10.1107/S1600576716000455.

(93) Ashiotis, G.; Deschildre, A.; Nawaz, Z.; Wright, J. P.; Karkoulis, D.; Picca, F. E.; Kieffer, J. The Fast Azimuthal Integration Python Library: PyFAI. *J. Appl.*

Crystallogr. **2015**, *48* (2), 510–519. https://doi.org/10.1107/S1600576715004306.

(94) Egami, T.; Billinge, S. J. L. *Underneath the Bragg Peaks: Structural Analysis of Complex Materials*; Newnes, 2012.

(95) Juhás, P.; Davis, T.; Farrow, C. L.; Billinge, S. J. L. PDFgetX3: A Rapid and Highly Automatable Program for Processing Powder Diffraction Data into Total Scattering Pair Distribution Functions. *J. Appl. Crystallogr.* **2013**, *46* (2), 560–566. https://doi.org/10.1107/S0021889813005190.

(96) Farrow, C. L.; Juhas, P.; Liu, J. W.; Bryndin, D.; Božin, E. S.; Bloch, J.; Proffen, T.; Billinge, S. J. L. PDFfit2 and PDFgui: Computer Programs for Studying Nanostructure in Crystals. *J. Phys. Condens. Matter* **2007**, *19* (33), 335219. https://doi.org/10.1088/0953-8984/19/33/335219.

(97) OriginLab Corporation. OriginPro. Northampton, MA, USA.

(98) *International Tables for Crystallography*; Aroyo, M. I., Ed.; International Union of Crystallography: Chester, England, 2016; Vol. A. https://doi.org/10.1107/97809553602060000114.

(99) McCaffrey, J. F.; McDevitt, N. T.; Phillippi, C. M. Infrared Lattice Spectra of Rare-Earth Stannate and Titanate Pyrochlores. *J. Opt. Soc. Am.* **1971**, *61* (2), 209. https://doi.org/10.1364/JOSA.61.000209.

(100) Scheetz, B. E.; White, W. B. Characterization of Anion Disorder in Zirconate A 2 B 2 O 7 Compounds by Raman Spectroscopy. *J. Am. Ceram. Soc.* **1979**, *62* (9–10), 468–470. https://doi.org/10.1111/j.1151-2916.1979.tb19107.x.

(101) Bhagavantam, S.; Venkatarayudu, T. Raman Effect in Relation to Crystal Structure. *Proc. Indian Acad. Sci. - Sect. A* **1939**, *9* (3), 224–258. https://doi.org/10.1007/BF03046465.

(102) DeAngelis, B. A.; Newham, R. E.; White, W. B. Factor Group Analysis of the Vibrational Spectra of Crystals: A Review and Consolidation. *American Mineral.* **1972**, *57* (1–2), 255–268.

(103) Vandenborre, N. T.; Husson, E.; Brusset, H. Analyse En Coordonnées Normales Des Composés A2IIIB2IVO7 (A = La, Nd; B = Zr, Hf) de Structure Pyrochlore. *Spectrochim. Acta Part A Mol. Spectrosc.* **1981**, *37* (2), 113–118. https://doi.org/10.1016/0584-8539(81)80096-7.

(104) Vandenborre, M. T.; Husson, E.; Chatry, J. P.; Michel, D. Rare-Earth Titanates and Stannates of Pyrochlore Structure; Vibrational Spectra and Force Fields. *J. Raman Spectrosc.* **1983**, *14* (2), 63–71. https://doi.org/10.1002/jrs.1250140202.

(105) Grima, L.; Peña, J. I.; Sanjuán, M. L. Pyrochlore-like ZrO2-PrOx Compounds: The Role of the Processing Atmosphere in the Stoichiometry, Microstructure and Oxidation State. *J. Alloys Compd.* **2022**, *923*, 166449. https://doi.org/10.1016/j.jallcom.2022.166449.

(106) Vandenborre, M. T.; Husson, E. Comparison of the Force Field in Various Pyrochlore Families. I. The A2B2O7 Oxides. *J. Solid State Chem.* **1983**, *50* (3), 362–371. https://doi.org/10.1016/0022-4596(83)90205-0.

(107) Saha, S.; Muthu, D. V. S.; Pascanut, C.; Dragoe, N.; Suryanarayanan, R.; Dhalenne, G.; Revcolevschi, A.; Karmakar, S.; Sharma, S. M.; Sood, A. K. High-Pressure Raman and x-Ray Study of the Spin-Frustrated Pyrochlore Gd2Ti2O7. *Phys. Rev. B* **2006**, *74* (6), 064109. https://doi.org/10.1103/PhysRevB.74.064109.

(108) Lummen, T. T. A.; Handayani, I. P.; Donker, M. C.; Fausti, D.; Dhalenne, G.; Berthet, P.; Revcolevschi, A.; Van Loosdrecht, P. H. M. Phonon and Crystal Field Excitations in Geometrically Frustrated Rare Earth Titanates. *Phys. Rev. B - Condens. Matter Mater. Phys.* **2008**, *77* (21), 1–11. https://doi.org/10.1103/PhysRevB.77.214310.

(109) Mączka, M.; Hanuza, J.; Hermanowicz, K.; Fuentes, A. F.; Matsuhira, K.; Hiroi, Z. Temperature-Dependent Raman Scattering Studies of the Geometrically Frustrated Pyrochlores Dy 2 Ti 2 O 7 , Gd 2 Ti 2 O 7 and Er 2 Ti 2 O 7. *J. Raman Spectrosc.* **2008**, *39* (4), 537–544. https://doi.org/10.1002/jrs.1875.

(110) Mączka, M.; Sanjuán, M. L.; Fuentes, A. F.; Macalik, L.; Hanuza, J.; Matsuhira, K.; Hiroi, Z. Temperature-Dependent Studies of the Geometrically Frustrated Pyrochlores Ho2Ti2O7 and Dy2Ti2O7. *Phys. Rev. B* **2009**, *79* (21), 214437. https://doi.org/10.1103/PhysRevB.79.214437.

(111) Michel, D.; y Jorba, M. P.; Collongues, R. Study by Raman Spectroscopy of Order-Disorder Phenomena Occurring in Some Binary Oxides with Fluorite-Related Structures. *J. Raman Spectrosc.* **1976**, *5* (2), 163–180. https://doi.org/10.1002/jrs.1250050208.

(112) Keramidas, V. G.; White, W. B. Raman Spectra of Oxides with the Fluorite Structure. *J. Chem. Phys.* **1973**, *59* (3), 1561–1562. https://doi.org/10.1063/1.1680227.

(113) Kovyazina, S. A.; Perelyaeva, L. A.; Leonidov, I. A.; Bakhteeva, Y. A. High-Temperature Structural Disorder in R 3 NbO 7. *J. Struct. Chem.* **2003**, *44* (6), 975–979. https://doi.org/10.1023/B:JORY.0000034803.89136.ba.

(114) White, W. B.; Keramidas, V. G. Vibrational Spetra of Oxides with the C-Type Rare Earth Oxide Structure. *Spectrochim. Acta Part A Mol. Spectrosc.* **1972**, *28A*, 501–509.

(115) Preux, N.; Rolle, A.; Merlin, C.; Benamira, M.; Malys, M.; Estournes, C.; Rubbens, A.; Vannier, R.-N. La3TaO7 Derivatives with Weberite Structure Type: Possible Electrolytes for Solid Oxide Fuel Cells and High Temperature Electrolysers. *Comptes Rendus Chim.* **2010**, *13* (11), 1351–1358. https://doi.org/10.1016/j.crci.2010.07.009.

(116) Wang, Y.; Jing, C.; Ding, Z.; Zhang, Y.; Wei, T.; Ouyang, J.; Liu, Z.; Wang, Y.-J.; Wang, Y. The Structure, Property, and Ion Irradiation Effects of Pyrochlores: A

Comprehensive Review. *Crystals* **2023**, *13* (1), 143. https://doi.org/10.3390/cryst13010143.

(117) Tanaka, S. Solid State Reactions and Sintering. In *Materials Chemistry of Ceramics*; Springer Singapore: Singapore, 2019; pp 45–74. https://doi.org/10.1007/978-981-13-9935-0_3.

(118) Laverov, N. P.; Yudintsev, S. V.; Livshits, T. S.; Stefanovsky, S. V.; Lukinykh, A. N.; Ewing, R. C. Synthetic Minerals with the Pyrochlore and Garnet Structures for Immobilization of Actinide-Containing Wastes. *Geochemistry Int.* **2010**, *48* (1), 1–14. https://doi.org/10.1134/S0016702910010015.

(119) Matsumoto, U.; Ogawa, T.; Kitaoka, S.; Moriwake, H.; Tanaka, I.; Matsumoto, U. First-Principles Study on the Stability of Weberite-Type, Pyrochlore, and Defect-Fluorite Structures of A 23+B 24+O7(A = Lu3+-La3+, B = Zr4+, Hf4+, Sn4+, and Ti4+). *J. Phys. Chem. C* **2020**, *124* (37), 20555–20562. https://doi.org/10.1021/acs.jpcc.0c05443.

(120) Subramani, T.; Voskanyan, A.; Jayanthi, K.; Abramchuk, M.; Navrotsky, A. A Comparison of Order-Disorder in Several Families of Cubic Oxides. *Front. Chem.* **2021**, *9* (September), 1–21. https://doi.org/10.3389/fchem.2021.719169.

(121) Sanjuán, M. L.; Guglieri, C.; Díaz-Moreno, S.; Aquilanti, G.; Fuentes, A. F.; Olivi, L.; Chaboy, J. Raman and X-Ray Absorption Spectroscopy Study of the Phase Evolution Induced by Mechanical Milling and Thermal Treatments in R2Ti2O7 Pyrochlores. *Phys. Rev. B* **2011**, *84* (10), 104207. https://doi.org/10.1103/PhysRevB.84.104207.

(122) O'Quinn, E. C.; Bishop, J. L.; Sherrod, R.; Neuefeind, J.; Montemayor, S. M.; Fuentes, A. F.; Lang, M. Advanced Characterization Technique for Mechanochemically Synthesized Materials: Neutron Total Scattering Analysis. *J. Mater. Sci.* **2018**, *53* (19), 13400–13410. https://doi.org/10.1007/s10853-018-2212-9.

(123) Chung, C. K.; Shamblin, J.; O'Quinn, E. C.; Shelyug, A.; Gussev, I.; Lang, M.; Navrotsky, A. Thermodynamic and Structural Evolution of Dy2Ti2O7 Pyrochlore after Swift Heavy Ion Irradiation. *Acta Mater.* **2018**, *145*, 227–234. https://doi.org/10.1016/j.actamat.2017.12.044.

(124) Moriga, T.; Yoshiasa, A.; Kanamaru, F.; Koto, K.; Yoshimura, M.; Sōmiya, S. Crystal Structure Analyses of the Pyrochlore and Fluorite-Type Zr2Gd2O7 and Anti-Phase Domain Structure. *Solid State Ionics* **1989**, *31* (4), 319–328. https://doi.org/10.1016/0167-2738(89)90472-4.

(125) Wilde, P. Defects and Diffusion in Pyrochlore Structured Oxides. *Solid State Ionics* **1998**, *112* (3–4), 173–183. https://doi.org/10.1016/S0167-2738(98)00190-8.

(126) Nachimuthu, P.; Thevuthasan, S.; Adams, E. M.; Weber, W. J.; Begg, B. D.; Mun, B. S.; Shuh, D. K.; Lindle, D. W.; Gullikson, E. M.; Perera, R. C. C. Near-Edge X-Ray Absorption Fine Structure Study of Disordering in Gd 2 (Ti 1 - y Zr y) 2 O 7

Pyrochlores. *J. Phys. Chem. B* **2005**, *109* (4), 1337–1339. https://doi.org/10.1021/jp0447789.

(127) Argyriou, D. N. Measurement of the Static Disorder Contribution to the Temperature Factor in Cubic Stabilized ZrO 2. *J. Appl. Crystallogr.* **1994**, *27* (2), 155–158. https://doi.org/10.1107/S0021889893007964.

(128) Coduri, M.; Masala, P.; Allieta, M.; Peral, I.; Brunelli, M.; Biffi, C. A.; Scavini, M. Phase Transformations in the CeO2-Sm2O3 System: A Multiscale Powder Diffraction Investigation. *Inorg. Chem.* **2018**, *57* (2), 879–891. https://doi.org/10.1021/acs.inorgchem.7b02896.

(129) Oueslati, M.; Balkanski, M.; Moon, P. K.; Tuller, H. L. Raman Spectroscopy and Structural Disorder in Gd 2 (Zr x Ti 1−x) 2 O 7. *MRS Proc.* **1988**, *135*, 199. https://doi.org/10.1557/PROC-135-199.

(130) Wan, C.; Qu, Z.; Du, A.; Pan, W. Influence of B Site Substituent Ti on the Structure and Thermophysical Properties of A2B2O7-Type Pyrochlore Gd2Zr2O7. *Acta Mater.* **2009**, *57* (16), 4782–4789. https://doi.org/10.1016/j.actamat.2009.06.040.

(131) Bhuiyan, A.; Wong, V.; Abraham, J. L.; Aughterson, R. D.; Kong, L.; Farzana, R.; Gregg, D. J.; Sorrell, C. C.; Zhang, Y.; Koshy, P. Phase Assemblage and Microstructures of Gd2Ti2-XZrxO7 (x = 0.1–0.3) Pyrochlore Glass-Ceramics as Potential Waste Forms for Actinide Immobilization. *Mater. Chem. Phys.* **2021**, *273* (July), 125058. https://doi.org/10.1016/j.matchemphys.2021.125058.

(132) Kumar, A.; Sharma, S. K.; Grover, V.; Singh, Y.; Kumar, V.; Shukla, V. K.; Kulriya, P. K. Probing the Short-Range Ordering of Ion Irradiated Gd2Ti2-YZryO7 ($0.0 \leq y \leq 2.0$) Pyrochlore under Electronic Stopping Regime. *J. Nucl. Mater.* **2022**, *564*, 153682. https://doi.org/10.1016/j.jnucmat.2022.153682.

(133) Gupta, H. C.; Brown, S.; Rani, N.; Gohel, V. B. Lattice Dynamic Investigation of the Zone Center Wavenumbers of the Cubic A2Ti2O7 Pyrochlores. *J. Raman Spectrosc.* **2001**, *32* (1), 41–44. https://doi.org/10.1002/1097-4555(200101)32:1<41::AID-JRS664>3.0.CO;2-R.

(134) Kumar, S.; Gupta, H. C. First Principles Study of Zone Centre Phonons in Rare-Earth Pyrochlore Titanates, RE 2Ti 2O 7 (RE = Gd, Dy, Ho, Er, Lu; Y). *Vib. Spectrosc.* **2012**, *62*, 180–187. https://doi.org/10.1016/j.vibspec.2012.06.001.

(135) Chernyshev, V. A.; Petrov, V. P.; Nikiforov, A. E. Lattice Dynamics of Rare-Earth Titanates with the Structure of Pyrochlore R2Ti2O7 (R = Gd, Tb, Dy, Ho, Er, Tm, Yb, and Lu): Ab Initio Calculation. *Phys. Solid State* **2015**, *57* (5), 996–1002. https://doi.org/10.1134/S1063783415050078.

(136) Gupta, H. C.; Brown, S. An Analytical Expression for Eg and Ag Modes of Pyrochlores. *J. Phys. Chem. Solids* **2003**, *64* (11), 2205–2207. https://doi.org/10.1016/S0022-3697(03)00234-8.

(137) Gupta, H. C.; Singh, J.; Kumar, S.; Karandeep; Rani, N. A Lattice Dynamical

Investigation of the Raman and the Infrared Frequencies of the Dy2Ti2O7 Pyrochlore Spin Ice Compound. *J. Mol. Struct.* **2009**, *937* (1–3), 136–138. https://doi.org/10.1016/j.molstruc.2009.08.027.

(138) Yastrebtsev, A. A.; Popov, V. V.; Menushenkov, A. P.; Beskrovnyi, A. I.; Neov, D. S.; Shchetinin, I. V.; Ponkratov, K. V. Comparative Neutron and X-Ray Diffraction Analysis of Anionic and Cationic Ordering in Rare-Earth Zirconates (Ln = La, Nd, Tb, Yb, Y). *J. Alloys Compd.* **2020**, *832*, 154863. https://doi.org/10.1016/j.jallcom.2020.154863.

(139) Kushwaha, A. K.; Mishra, S. P.; Vishwakarma, M. K.; Chauhan, S.; Jappor, H. R.; Khenata, R.; Bin Omran, S. Theoretical Study of Thermal Conductivity, Mechanical, Vibrational and Thermodynamical Properties of Ln2Zr2O7 (Ln = La, Nd, Sm, and Eu) Pyrochlore. *Inorg. Chem. Commun.* **2021**, *127* (February), 108495. https://doi.org/10.1016/j.inoche.2021.108495.

(140) Tracy, C. L.; Shamblin, J.; Park, S.; Zhang, F.; Trautmann, C.; Lang, M.; Ewing, R. C. Role of Composition, Bond Covalency, and Short-Range Order in the Disordering of Stannate Pyrochlores by Swift Heavy Ion Irradiation. *Phys. Rev. B* **2016**, *94* (6), 064102. https://doi.org/10.1103/PhysRevB.94.064102.

(141) Mori, M. Compatibility of GdxTi2O7 Pyrochlores ($1.72 \leq x \leq 2.0$) as Electrolytes in High-Temperature Solid Oxide Fuel Cells. *Solid State Ionics* **2003**, *158* (1–2), 79–90. https://doi.org/10.1016/S0167-2738(02)00761-0.

(142) Zhang, F. X.; Manoun, B.; Saxena, S. K.; Zha, C. S. Structure Change of Pyrochlore Sm2Ti2O7 at High Pressures. *Appl. Phys. Lett.* **2005**, *86* (18), 181906. https://doi.org/10.1063/1.1925307.

(143) Poulsen, F. .; Glerup, M.; Holtappels, P. Structure, Raman Spectra and Defect Chemistry Modelling of Conductive Pyrochlore Oxides. *Solid State Ionics* **2000**, *135* (1–4), 595–602. https://doi.org/10.1016/S0167-2738(00)00417-3.

(144) Oliete, P. B.; Orera, A.; Sanjuán, M. L. Spectroscopic Insight into the Interplay between Structural Disorder and Oxidation Degree in Melt-grown Ce 0.5 Zr 0.5 O 2- y Compounds. *J. Raman Spectrosc.* **2020**, *51* (3), 514–527. https://doi.org/10.1002/jrs.5797.

(145) Suganya, M.; Ganesan, K.; Vijayakumar, P.; Gill, A. S.; Srivastava, S. K.; Singh, C. K.; Sarguna, R. M.; Ajikumar, P. K.; Ganesamoorthy, S. Raman and Photoluminescence Spectroscopic Studies on Structural Disorder in Oxygen Deficient Gd 2 Ti 2 O 7-δ Single Crystals. *Cryst. Res. Technol.* **2022**, *57* (4), 2100287. https://doi.org/10.1002/crat.202100287.

(146) Zhang, F. X.; Manoun, B.; Saxena, S. K. Pressure-Induced Order–Disorder Transitions in Pyrochlore RE2Ti2O7 (RE=Y, Gd). *Mater. Lett.* **2006**, *60* (21–22), 2773–2776. https://doi.org/10.1016/j.matlet.2006.01.095.

(147) Jafar, M.; Achary, S. N.; Salke, N. P.; Sahu, A. K.; Rao, R.; Tyagi, A. K. X-Ray Diffraction and Raman Spectroscopic Investigations on CaZrTi2O7Y2Ti2O7

System: Delineation of Phase Fields Consisting of Potential Ceramic Host Materials. *J. Nucl. Mater.* **2016**, *475*, 192–199. https://doi.org/10.1016/j.jnucmat.2016.04.016.

(148) Brown, S.; Gupta, H. C.; Alonso, J. A.; Martinez-Lope, M. J. Vibrational Spectra and Force Field Calculation of A2Mn2O7 (A = Y, Dy, Er, Yb) Pyrochlores. *J. Raman Spectrosc.* **2003**, *34* (3), 240–243. https://doi.org/10.1002/jrs.982.

(149) Chernyshev, V. A. Phonon Spectrum of La2Zr2O7: Ab Initio Calculation. *Opt. Spectrosc.* **2019**, *127* (5), 825–831. https://doi.org/10.1134/S0030400X19110067.

(150) Zhang, F. X.; Saxena, S. K. Structural Changes and Pressure-Induced Amorphization in Rare Earth Titanates RE2Ti2O7 (RE: Gd, Sm) with Pyrochlore Structure. *Chem. Phys. Lett.* **2005**, *413* (1–3), 248–251. https://doi.org/10.1016/j.cplett.2005.07.094.

(151) Arenas, D. J.; Gasparov, L. V.; Qiu, W.; Nino, J. C.; Patterson, C. H.; Tanner, D. B. Raman Study of Phonon Modes in Bismuth Pyrochlores. *Phys. Rev. B - Condens. Matter Mater. Phys.* **2010**, *82* (21), 1–8. https://doi.org/10.1103/PhysRevB.82.214302.

(152) Salamat, A.; McMillan, P. F.; Firth, S.; Woodhead, K.; Hector, A. L.; Garbarino, G.; Stennett, M. C.; Hyatt, N. C. Structural Transformations and Disordering in Zirconolite (CaZrTi 2 O 7) at High Pressure. *Inorg. Chem.* **2013**, *52* (3), 1550–1558. https://doi.org/10.1021/ic302346g.

(153) Blackburn, L. R.; Sun, S.; Gardner, L. J.; Maddrell, E. R.; Stennett, M. C.; Hyatt, N. C. A Systematic Investigation of the Phase Assemblage and Microstructure of the Zirconolite CaZr1-XCexTi2O7 System. *J. Nucl. Mater.* **2020**, *535*, 1–11. https://doi.org/10.1016/j.jnucmat.2020.152137.

(154) Zhang, Y.; Karatchevtseva, I.; Qin, M.; Middleburgh, S. C.; Lumpkin, G. R. Raman Spectroscopic Study of Natural and Synthetic Brannerite. *J. Nucl. Mater.* **2013**, *437* (1–3), 149–153. https://doi.org/10.1016/j.jnucmat.2013.02.004.

(155) Zhang, Y.; Čejka, J.; Karatchevtseva, I.; Qin, M.; Kong, L.; Short, K.; Middleburgh, S. C.; Lumpkin, G. R. Theoretical and Experimental Raman Spectroscopic Studies of Synthetic Thorutite (ThTi2O6). *J. Nucl. Mater.* **2014**, *446* (1–3), 68–72. https://doi.org/10.1016/j.jnucmat.2013.11.037.

(156) Gumber, N.; Pai, R. V.; Phatak, R.; Adiraju, B.; Sahu, M.; Jagannath, J.; Sudarshan, K. Synthesis, Characterization and Crystal Chemistry of Uranium and Cerium Doped Yttrium Titanate Pyrochlore: A Potential Waste Immobilization Matrix. *J. Nucl. Mater.* **2021**, *556*, 153191. https://doi.org/10.1016/j.jnucmat.2021.153191.

(157) Kulriya, P. K.; Yao, T.; Scott, S. M.; Nanda, S.; Lian, J. Influence of Grain Growth on the Structural Properties of the Nanocrystalline Gd2Ti2O7. *J. Nucl. Mater.* **2017**, *487*, 373–379. https://doi.org/10.1016/j.jnucmat.2017.02.032.

(158) Saha, S.; Singh, S.; Dkhil, B.; Dhar, S.; Suryanarayanan, R.; Dhalenne, G.; Revcolevschi, A.; Sood, A. K. Temperature-Dependent Raman and x-Ray Studies

of the Spin-Ice Pyrochlore Dy2Ti2O7 and Nonmagnetic Pyrochlore Lu2Ti2O7. *Phys. Rev. B* **2008**, *78* (21), 214102. https://doi.org/10.1103/PhysRevB.78.214102.

(159) Jafar, M.; Phapale, S. B.; Nigam, S.; Achary, S. N.; Mishra, R.; Majumder, C.; Tyagi, A. K. Implication of Aliovalent Cation Substitution on Structural and Thermodynamic Stability of Gd2Ti2O7: Experimental and Theoretical Investigations. *J. Alloys Compd.* **2021**, *859*, 157781. https://doi.org/10.1016/j.jallcom.2020.157781.

(160) Mandal, B. P.; Krishna, P. S. R.; Tyagi, A. K. Order–Disorder Transition in the Nd2−yYyZr2O7 System: Probed by X-Ray Diffraction and Raman Spectroscopy. *J. Solid State Chem.* **2010**, *183* (1), 41–45. https://doi.org/10.1016/j.jssc.2009.10.010.

(161) Yang, Z.; Li, Y.; Pan, W.; Wan, C. Abnormal Thermal Expansion Coefficients in (Nd 1− x Dy x) 2 Zr 2 O 7 Pyrochlore: The Effect of Low-Lying Optical Phonons. *J. Adv. Ceram.* **2023**, *12* (5), 1001–1014. https://doi.org/10.26599/JAC.2023.9220734.

(162) Renju, U. A.; Prabhakar Rao, P. Contrasting Anion Disorder Behavior in Sm2Zr2O7 by Simultaneous Aliovalent Cation Substitutions and Its Structural and Electrical Properties. *J. Appl. Phys.* **2019**, *126* (4), 45110. https://doi.org/10.1063/1.5100237.

(163) Yang, X.; Masadeh, A. S.; McBride, J. R.; Božin, E. S.; Rosenthal, S. J.; Billinge, S. J. L. Confirmation of Disordered Structure of Ultrasmall CdSe Nanoparticles from X-Ray Atomic Pair Distribution Function Analysis. *Phys. Chem. Chem. Phys.* **2013**, *15* (22), 8480. https://doi.org/10.1039/c3cp00111c.

(164) Shafique, M.; Kennedy, B. J.; Iqbal, Y.; Ubic, R. The Effect of B-Site Substitution on Structural Transformation and Ionic Conductivity in Ho2(ZryTi1−y)2O7. *J. Alloys Compd.* **2016**, *671*, 226–233. https://doi.org/10.1016/j.jallcom.2016.02.087.

(165) Stokes, H. T.; Hatch, D. M. FINDSYM : Program for Identifying the Space-Group Symmetry of a Crystal. *J. Appl. Crystallogr.* **2005**, *38* (1), 237–238. https://doi.org/10.1107/S0021889804031528.

(166) Farrow, C. L.; Shaw, M.; Kim, H.; Juhás, P.; Billinge, S. J. L. Nyquist-Shannon Sampling Theorem Applied to Refinements of the Atomic Pair Distribution Function. *Phys. Rev. B* **2011**, *84* (13), 134105. https://doi.org/10.1103/PhysRevB.84.134105.

(167) Smith, D. K.; Newkirk, W. The Crystal Structure of Baddeleyite (Monoclinic ZrO 2) and Its Relation to the Polymorphism of ZrO 2. *Acta Crystallogr.* **1965**, *18* (6), 983–991. https://doi.org/10.1107/S0365110X65002402.

(168) Marlton, F. P.; Zhang, Z.; Zhang, Y.; Proffen, T. E.; Ling, C. D.; Kennedy, B. J. Lattice Disorder and Oxygen Migration Pathways in Pyrochlore and Defect-Fluorite Oxides. *Chem. Mater.* **2021**, *33* (4), 1407–1415. https://doi.org/10.1021/acs.chemmater.0c04515.

(169) di Biase, A.; Castellano, C.; Confalonieri, G.; Fumagalli, P.; Tumiati, S.; Ceresoli, D.; Scavini, M. Emerging Disorder in Gd 2 (Ti 1− x Zr x) 2 O 7 Pyrochlores Matrices for Radioactive Waste Disposal: Symmetry Lowering versus Defect Clustering. *J. Mater. Chem. A* **2023**. https://doi.org/10.1039/D3TA04847K.

(170) Zoghlin, E.; Schmehr, J.; Holgate, C.; Dally, R.; Liu, Y.; Laurita, G.; Wilson, S. D. Evaluating the Effects of Structural Disorder on the Magnetic Properties of Nd2Zr2O7 Eli. *Phys. Rev. Mater.* **2021**, *5* (8), 084403. https://doi.org/10.1103/PhysRevMaterials.5.084403.

(171) Ubic, R.; Abrahams, I.; Hu, Y. Oxide Ion Disorder in Nd2Hf2O7. *J. Am. Ceram. Soc.* **2007**, *91* (1), 235–239. https://doi.org/10.1111/j.1551-2916.2007.02025.x.

(172) Clements, R.; Hester, J. R.; Kennedy, B. J.; Ling, C. D.; Stampfl, A. P. J. The Fluorite–Pyrochlore Transformation of Ho2−yNdyZr2O7. *J. Solid State Chem.* **2011**, *184* (8), 2108–2113. https://doi.org/10.1016/j.jssc.2011.05.054.

(173) Mandal, B. P.; Tyagi, A. K. Preparation and High Temperature-XRD Studies on a Pyrochlore Series with the General Composition Gd2−xNdxZr2O7. *J. Alloys Compd.* **2007**, *437* (1–2), 260–263. https://doi.org/10.1016/j.jallcom.2006.07.093.

(174) Harvey, E. J.; Whittle, K. R.; Lumpkin, G. R.; Smith, R. I.; Redfern, S. A. T. Solid Solubilities of (La Nd,)2(Zr,Ti)2O7 Phases Deduced by Neutron Diffraction. *J. Solid State Chem.* **2005**, *178* (3), 800–810. https://doi.org/10.1016/j.jssc.2004.12.030.

(175) Whittle, K. R.; Cranswick, L. M. D.; Redfern, S. A. T.; Swainson, I. P.; Lumpkin, G. R. Lanthanum Pyrochlores and the Effect of Yttrium Addition in the Systems La2−xYxZr2O7 and La2−xYxHf2O7. *J. Solid State Chem.* **2009**, *182* (3), 442–450. https://doi.org/10.1016/j.jssc.2008.11.008.

(176) Nandi, S.; Jana, Y. M.; Gupta, H. C. Lattice Dynamical Investigation of the Raman and Infrared Wave Numbers and Heat Capacity Properties of the Pyrochlores R2Zr2O7 (R = La, Nd, Sm, Eu). *J. Phys. Chem. Solids* **2018**, *115* (December 2017), 347–354. https://doi.org/10.1016/j.jpcs.2018.01.001.

(177) Kong, L.; Karatchevtseva, I.; Gregg, D. J.; Blackford, M. G.; Holmes, R.; Triani, G. Gd2Zr2O7 and Nd2Zr2O7 Pyrochlore Prepared by Aqueous Chemical Synthesis. *J. Eur. Ceram. Soc.* **2013**, *33* (15–16), 3273–3285. https://doi.org/10.1016/j.jeurceramsoc.2013.05.011.

(178) Nandi, C.; Poswal, A. K.; Jafar, M.; Kesari, S.; Grover, V.; Rao, R.; Prakash, A.; Behere, P. G. Effect of Ce4+-Substitution at A and B Sites of Nd2Zr2O7: A Study for Plutonium Incorporation in Pyrochlores. *J. Nucl. Mater.* **2020**, *539*, 152342. https://doi.org/10.1016/j.jnucmat.2020.152342.

(179) Sharma, S. K.; Grover, V.; Shukla, R.; Hussain, A.; Mishra, A.; Meena, R. C.; Kulriya, P. K. Evidence of Improved Tolerance to Electronic Excitation in Nanostructured Nd2Zr2O7. *J. Appl. Phys.* **2021**, *129* (11), 115902. https://doi.org/10.1063/5.0039390.

(180) Nandi, C.; Phatak, R.; Kesari, S.; Shafeeq, M.; Patkare, G.; Jha, S. N.; Rao, R.; Mishra, S.; Prakash, A.; Behere, P. G. Influence of Synthesis Atmosphere on the Solid Solubility of Uranium at B-Site of Nd2Zr2O7 Pyrochlore. *J. Nucl. Mater.* **2023**, *574*, 154175. https://doi.org/10.1016/j.jnucmat.2022.154175.

(181) Tang, Z.; Huang, Z.; Han, W.; Qi, J.; Shi, Y.; Ma, N.; Zhang, Y.; Guo, X.; Lu, T. Uranium-Incorporated Pyrochlore La 2 (U x Mg x Zr 1–2 x) 2 O 7 Nuclear Waste Form: Structure and Phase Stability. *Inorg. Chem.* **2020**, *59* (14), 9919–9926. https://doi.org/10.1021/acs.inorgchem.0c01089.

(182) Fuentes, A. F.; Montemayor, S. M.; Maczka, M.; Lang, M.; Ewing, R. C.; Amador, U. A Critical Review of Existing Criteria for the Prediction of Pyrochlore Formation and Stability. *Inorg. Chem.* **2018**, *57* (19), 12093–12105. https://doi.org/10.1021/acs.inorgchem.8b01665.

(183) Banerji, A.; Grover, V.; Sathe, V.; Deb, S. K.; Tyagi, A. K. CeO2–Gd2O3 System: Unraveling of Microscopic Features by Raman Spectroscopy. *Solid State Commun.* **2009**, *149* (39–40), 1689–1692. https://doi.org/10.1016/j.ssc.2009.06.045.

(184) Artini, C.; Pani, M.; Carnasciali, M. M.; Buscaglia, M. T.; Plaisier, J. R.; Costa, G. A. Structural Features of Sm- and Gd-Doped Ceria Studied by Synchrotron X-Ray Diffraction and μ-Raman Spectroscopy. *Inorg. Chem.* **2015**, *54* (8), 4126–4137. https://doi.org/10.1021/acs.inorgchem.5b00395.

(185) Schmitt, R.; Nenning, A.; Kraynis, O.; Korobko, R.; Frenkel, A. I.; Lubomirsky, I.; Haile, S. M.; Rupp, J. L. M. A Review of Defect Structure and Chemistry in Ceria and Its Solid Solutions. *Chem. Soc. Rev.* **2020**, *49* (2), 554–592. https://doi.org/10.1039/C9CS00588A.

(186) Mandal, B. P.; Roy, M.; Grover, V.; Tyagi, A. K. X-Ray Diffraction, μ-Raman Spectroscopic Studies on CeO2−RE2O3 (RE=Ho, Er) Systems: Observation of Parasitic Phases. *J. Appl. Phys.* **2008**, *103* (3). https://doi.org/10.1063/1.2837042.

(187) Mandal, B. P.; Grover, V.; Roy, M.; Tyagi, A. K. X-Ray Diffraction and Raman Spectroscopic Investigation on the Phase Relations in Yb 2 O 3 - and Tm 2 O 3 - Substituted CeO 2. *J. Am. Ceram. Soc.* **2007**, *90* (9), 2961–2965. https://doi.org/10.1111/j.1551-2916.2007.01826.x.

(188) Nakagawa, T.; Osuki, T.; Yamamoto, T. A.; Kitauji, Y.; Kano, M.; Katsura, M.; Emura, S. Study on Local Structure around Ce and Gd Atoms in CeO 2 –Gd 2 O 3 Binary System. *J. Synchrotron Radiat.* **2001**, *8* (2), 740–742. https://doi.org/10.1107/S0909049500018148.

(189) McBride, J. R.; Hass, K. C.; Poindexter, B. D.; Weber, W. H. Raman and X-Ray Studies of Ce1− x RE x O2− y , Where RE=La, Pr, Nd, Eu, Gd, and Tb. *J. Appl. Phys.* **1994**, *76* (4), 2435–2441. https://doi.org/10.1063/1.357593.

(190) Nakajima, A.; Yoshihara, A.; Ishigame, M. Defect-Induced Raman Spectra in Doped CeO2. *Phys. Rev. B* **1994**, *50* (18), 13297–13307. https://doi.org/10.1103/PhysRevB.50.13297.

(191) Chung, C. K.; O'Quinn, E. C.; Neuefeind, J. C.; Fuentes, A. F.; Xu, H.; Lang, M.; Navrotsky, A. Thermodynamic and Structural Evolution of Mechanically Milled and Swift Heavy Ion Irradiated Er2Ti2O7 Pyrochlore. *Acta Mater.* **2019**, *181*, 309–317. https://doi.org/10.1016/j.actamat.2019.09.022.

(192) Shamblin, J.; Tracy, C. L.; Palomares, R. I.; O'Quinn, E. C.; Ewing, R. C.; Neuefeind, J.; Feygenson, M.; Behrens, J.; Trautmann, C.; Lang, M. Similar Local Order in Disordered Fluorite and Aperiodic Pyrochlore Structures. *Acta Mater.* **2018**, *144*, 60–67. https://doi.org/10.1016/j.actamat.2017.10.044.

(193) Sherrod, R.; O'Quinn, E. C.; Gussev, I. M.; Overstreet, C.; Neuefeind, J.; Lang, M. K. Comparison of Short-Range Order in Irradiated Dysprosium Titanates. *npj Mater. Degrad.* **2021**, *5* (1), 19. https://doi.org/10.1038/s41529-021-00165-6.

(194) O'Quinn, E. C.; Tracy, C. L.; Cureton, W. F.; Sachan, R.; Neuefeind, J. C.; Trautmann, C.; Lang, M. K. Multi-Scale Investigation of Heterogeneous Swift Heavy Ion Tracks in Stannate Pyrochlore. *J. Mater. Chem. A* **2021**, *9* (31), 16982–16997. https://doi.org/10.1039/d1ta04924k.

(195) Drey, D.; O'Quinn, E.; Finkeldei, S.; Neuefeind, J.; Lang, M. Local Ordering in Disordered Nd Zr1-O2-0.5 Pyrochlore as Observed Using Neutron Total Scattering. *Acta Mater.* **2022**, *225*, 117590. https://doi.org/10.1016/j.actamat.2021.117590.

(196) Jothi, P. R.; Liyanage, W.; Jiang, B.; Paladugu, S.; Olds, D.; Gilbert, D. A.; Page, K. Persistent Structure and Frustrated Magnetism in High Entropy Rare-Earth Zirconates. *Small* **2022**, *18* (5), 2101323. https://doi.org/10.1002/smll.202101323.

(197) Zhang, D.; Chen, Y.; Vega, H.; Feng, T.; Yu, D.; Everett, M.; Neuefeind, J.; An, K.; Chen, R.; Luo, J. Long- and Short-Range Orders in 10-Component Compositionally Complex Ceramics. *Adv. Powder Mater.* **2023**, *2* (2), 100098. https://doi.org/10.1016/j.apmate.2022.100098.

(198) Donald, I. W.; Metcalfe, B. L.; Taylor, R. N. J. The Immobilization of High Level Radioactive Wastes Using Ceramics and Glasses. *J. Mater. Sci.* **1997**, *32* (22), 5851–5887. https://doi.org/10.1023/A:1018646507438.

(199) *Estimation of Global Inventories of Radioactive Waste and Other Radioactive Materials*; TECDOC Series; INTERNATIONAL ATOMIC ENERGY AGENCY: Vienna, 2008.

(200) *Fundamental Safety Principles*; Safety Fundamentals; INTERNATIONAL ATOMIC ENERGY AGENCY: Vienna, 2006.

(201) *Disposal of Radioactive Waste*; Specific Safety Requirements; INTERNATIONAL ATOMIC ENERGY AGENCY: Vienna, 2011.

(202) Ojovan, M. I. Nuclear Waste Disposal. *Encyclopedia* **2023**, *3* (2), 419–429. https://doi.org/10.3390/encyclopedia3020028.

(203) *Classification of Radioactive Waste*; General Safety Guides; INTERNATIONAL ATOMIC ENERGY AGENCY: Vienna, 2009.

(204) *IAEA Safeguards Glossary*; International Nuclear Verification Series; INTERNATIONAL ATOMIC ENERGY AGENCY: Vienna, 2022.

(205) Caurant, D.; Loiseau, P.; Majerus, O.; Aubin-Chevaldonnet, V.; Bardez, I.; Quintas, A. *Glasses, Glass-Ceramics and Ceramics for Immobilization of Highly Radioactive Nuclear Wastes*; 2009.

(206) Ewing, R. C.; Whittleston, R. A.; Yardley, B. W. D. Geological Disposal of Nuclear Waste: A Primer. *Elements* **2016**, *12* (4), 233–237. https://doi.org/10.2113/gselements.12.4.233.

(207) Ojovan, M. I.; Steinmetz, H. J. Approaches to Disposal of Nuclear Waste. *Energies* **2022**, *15* (20). https://doi.org/10.3390/en15207804.

(208) Ewing, R. C. Ceramic Matrices for Plutonium Disposition. *Prog. Nucl. Energy* **2007**, *49* (8), 635–643. https://doi.org/10.1016/j.pnucene.2007.02.003.

(209) Ewing, R. C. Long-Term Storage of Spent Nuclear Fuel. *Nat. Mater.* **2015**. https://doi.org/10.1038/nmat4226.

(210) McMaster, S. A.; Ram, R.; Faris, N.; Pownceby, M. I. Radionuclide Disposal Using the Pyrochlore Supergroup of Minerals as a Host Matrix—A Review. *J. Hazard. Mater.* **2018**, *360*, 257–269. https://doi.org/10.1016/j.jhazmat.2018.08.037.

(211) *Options for Management of Spent Fuel and Radioactive Waste for Countries Developing New Nuclear Power Programmes*; Nuclear Energy Series; INTERNATIONAL ATOMIC ENERGY AGENCY: Vienna, 2018.

(212) Chapman, N.; Hooper, A. The Disposal of Radioactive Wastes Underground. *Proc. Geol. Assoc.* **2012**, *123* (1), 46–63. https://doi.org/10.1016/j.pgeola.2011.10.001.

(213) *Energy, Electricity and Nuclear Power Estimates for the Period up to 2050*; Reference Data Series; INTERNATIONAL ATOMIC ENERGY AGENCY: Vienna, 2022.

(214) Power Reactor Information System (PRIS) by IAEA https://pris.iaea.org/pris/ (accessed Jun 4, 2023).

(215) *Design and Operation of High Level Waste Vitrification and Storage Facilities*; Technical Reports Series; INTERNATIONAL ATOMIC ENERGY AGENCY: Vienna, 1992.

(216) Ewing, R. C.; Weber, W. J.; Clinard, F. W. Radiation Effects in Nuclear Waste Forms for High-Level Radioactive Waste. *Prog. Nucl. Energy* **1995**, *29* (2), 63–127. https://doi.org/10.1016/0149-1970(94)00016-Y.

(217) Vienna, J. D. Nuclear Waste Vitrification in the United States: Recent Developments and Future Options. *Int. J. Appl. Glas. Sci.* **2010**, *1* (3), 309–321. https://doi.org/10.1111/j.2041-1294.2010.00023.x.

(218) Vernaz, É.; Bruezière, J. History of Nuclear Waste Glass in France. *Procedia Mater. Sci.* **2014**, *7*, 3–9. https://doi.org/10.1016/j.mspro.2014.10.002.

(219) Gin, S.; Jollivet, P.; Tribet, M.; Peuget, S.; Schuller, S. Radionuclides Containment in Nuclear Glasses: An Overview. *Radiochim. Acta* **2017**, *105* (11), 927–959. https://doi.org/10.1515/ract-2016-2658.

(220) Ojovan, M. I. *Handbook of Advanced Radioactive Waste Conditioning Technologies*; Woodhead Publishing Limited, 2011. https://doi.org/10.1533/9780857090959.

(221) McCarthy, G. J. High-Level Waste Ceramics: Materials Considerations, Process Simulation, and Product Characterization. *Nucl. Technol.* **1977**, *32* (1), 92–105. https://doi.org/10.13182/NT77-A31741.

(222) Ringwood, A. E.; Kesson, S. E.; Ware, N. G.; Hibberson, W.; Major, A. Immobilisation of High Level Nuclear Reactor Wastes in SYNROC. *Nature* **1979**, *278* (5701), 219–223. https://doi.org/10.1038/278219a0.

(223) Ringwood, A. E.; Kelly, P. M.; Bowie, S. H. U.; Kletz, T. A. Immobilization of High-Level Waste in Ceramic Waste Forms [and Discussion]. *Philos. Trans. R. Soc. London. Ser. A, Math. Phys. Sci.* **1986**, *319* (1545), 63–82.

(224) Ringwood, A. E. Safe Disposal of High Level Nuclear Wastes: A New Strategy. *Aust. Natl. Univ. Press* **1978**, 1–63.

(225) Gregg, D. J.; Farzana, R.; Dayal, P.; Holmes, R.; Triani, G. Synroc Technology: Perspectives and Current Status (Review). *J. Am. Ceram. Soc.* **2020**, *103* (10), 5424–5441. https://doi.org/10.1111/jace.17322.

(226) Kesson, S. E.; Ringwood, A. E. Safe Disposal of Spent Nuclear Fuel. *Radioact Waste Manag. Nucl Fuel Cycle* **1983**, *4* (2), 159–174.

(227) Gregg, D. J.; Vance, E. R. Synroc Tailored Waste Forms for Actinide Immobilization. *Radiochim. Acta* **2017**, *105* (11), 907–925. https://doi.org/10.1515/ract-2016-2604.

(228) Zhang, F. X.; Lang, M.; Ewing, R. C. Atomic Disorder in Gd2Zr2O7 Pyrochlore. *Appl. Phys. Lett.* **2015**, *106* (19). https://doi.org/10.1063/1.4921268.

(229) Yudintsev, S. V. Isolation of Separated Waste of Nuclear Industry. *Radiochemistry* **2021**, *63* (5), 527–555. https://doi.org/10.1134/s1066362221050015.

(230) Ewing, R. C. Plutonium and "Minor" Actinides: Safe Sequestration. *Earth Planet. Sci. Lett.* **2005**, *229* (3–4), 165–181. https://doi.org/10.1016/j.epsl.2004.11.017.

(231) Weber, W. J.; Navrotsky, A.; Stefanovsky, S.; Vance, E. R.; Vernaz, E. Materials Science of High-Level Nuclear Waste Immobilization. *MRS Bull.* **2009**, *34* (1), 46–53. https://doi.org/10.1557/mrs2009.12.

(232) Ojovan, M. I.; Petrov, V. A.; Yudintsev, S. V. Glass Crystalline Materials as Advanced Nuclear Wasteforms. *Sustain.* **2021**, *13* (8). https://doi.org/10.3390/su13084117.

(233) Lumpkin, G. R.; Begg, B. D.; Smith, K. L. Radiation Damage Effects in Pyrochlore

and Zirconolite Ceramic Matrices for the Immobilization of Actinide-Rich Wastes. In *Scientific research on the back-end of the fuel cycle for the 21 century*; France, 2000; p 575.

(234) Lumpkin, G.; Ewing, R. Alpha-Decay Damage in Minerals of the Pyrochlore Group. *Phys. Chem. Miner.* **1988**, *16* (1). https://doi.org/10.1007/BF00201325.

(235) Clinard, F. W.; Rohr, D. L.; Roof, R. B. Structural Damage in a Self-Irradiated Zirconolite-Based Ceramic. *Nucl. Instruments Methods Phys. Res. Sect. B Beam Interact. with Mater. Atoms* **1984**, *1* (2–3), 581–586. https://doi.org/10.1016/0168-583X(84)90127-7.

(236) Weber, W. J.; Wald, J. W.; Matzke, H. Self-Radiation Damage in Gd2Ti2O7. *Mater. Lett.* **1985**, *3* (4), 173–180. https://doi.org/10.1016/0167-577X(85)90154-5.

(237) Ewing, R. C.; Wang, L. M. Amorphization of Zirconolite: Alpha-Decay Event Damage versus Krypton Ion Irradiation. *Nucl. Instruments Methods Phys. Res. Sect. B Beam Interact. with Mater. Atoms* **1992**, *65* (1–4), 319–323. https://doi.org/10.1016/0168-583X(92)95059-Z.

(238) Lian, J.; Chen, J.; Wang, M.; Ewing, R. C.; Farmer, J. M.; Boatner, L. A.; Helean, B. Radiation-Induced Amorphization of Rare-Earth Titanate Pyrochlores. *Phys. Rev. B - Condens. Matter Mater. Phys.* **2003**, *68* (13), 1–9. https://doi.org/10.1103/PhysRevB.68.134107.

(239) Ewing, R. C.; Meldrum, A.; Wang, L.; Wang, S. Radiation-Induced Amorphization. *Rev. Mineral. Geochemistry* **2000**, *39* (1), 319–361. https://doi.org/10.2138/rmg.2000.39.12.

(240) Lang, M.; Lian, J.; Zhang, J.; Zhang, F.; Weber, W. J.; Trautmann, C.; Ewing, R. C. Single-Ion Tracks in Gd2Zr2−xTixO7 Pyrochlores Irradiated with Swift Heavy Ions Maik. *Phys. Rev. B* **2009**, *79* (22), 224105. https://doi.org/10.1103/PhysRevB.79.224105.

(241) Kumar, A.; Kulriya, P. K.; Sharma, S. K.; Grover, V.; Tyagi, A. K.; Shukla, V. K. Structural and Compositional Effects on the Electronic Excitation Induced Phase Transformations in Gd2Ti2-YZryO7 Pyrochlore. *J. Nucl. Mater.* **2020**, *539*, 152278. https://doi.org/10.1016/j.jnucmat.2020.152278.

(242) Goldschmidt, V. M. Die Gesetze Der Krystallochemie. *Naturwissenschaften* **1926**, *14* (21), 477–485. https://doi.org/10.1007/BF01507527.

(243) Isupov, V. A. GEOMETRICAL CRITERIA OF THE PYROCHLORE STRUCTURE TYPE. *Sov. Physics, Crystallogr.* **1958**, *3*, 96.

(244) Cai, L.; Arias, A. L.; Nino, J. C. The Tolerance Factors of the Pyrochlore Crystal Structure. *J. Mater. Chem.* **2011**, *21* (11), 3611. https://doi.org/10.1039/c0jm03380d.

(245) Mouta, R.; Silva, R. X.; Paschoal, C. W. A. Tolerance Factor for Pyrochlores and Related Structures. *Acta Crystallogr. Sect. B Struct. Sci. Cryst. Eng. Mater.* **2013**,

69 (5), 439–445. https://doi.org/10.1107/S2052519213020514.

(246) Song, Z.; Liu, Q. Tolerance Factor, Phase Stability and Order–Disorder of the Pyrochlore Structure. *Inorg. Chem. Front.* **2020**, *7* (7), 1583–1590. https://doi.org/10.1039/D0QI00016G.

(247) Pauling, L. THE PRINCIPLES DETERMINING THE STRUCTURE OF COMPLEX IONIC CRYSTALS. *J. Am. Chem. Soc.* **1929**, *51* (4), 1010–1026. https://doi.org/10.1021/ja01379a006.

(248) Pauling, L. *The Nature of the Chemical Bond and the Structure of Molecules and Crystals; an Introduction to Modern Structural Chemistry*; Cornell University Press: Ithaca (NY), 1960.